# Soft X-ray Spectroscopy of Cobalt Materials

---

## Zachte Röntgen Spectroscopie aan Kobalt Materialen

(met een samenvatting in het Nederlands)

Proefschrift

ter verkrijging van de graad van doctor aan de Universiteit Utrecht op gezag van de rector magnificus, prof. dr. G. J. van der Zwaan, ingevolge het besluit van het college voor promoties in het openbaar te verdedigen op maandag 28 augustus 2017 des middags te 2.30 uur

door

Boyang Liu

geboren op 22 november 1985 te Ya-an, China

Promotor: Prof.dr. F.M.F. de Groot

The research was funded by China Scholarship Council (CSC).

ISBN: 978-94-6182-810-1

Cover image: Chinese traditional blue and white porcelain disc, shined by the light. The blue part of the porcelain disc contains cobalt element. The light -in and -out indicates the X-ray probe.

Printed by: Offpage.nl

# Contents

**Chapter 1:** **1**

Introduction

**Chapter 2:** **25**

Transition metal sites in $[Co_4(H_2O)_2(\alpha\text{-}PW_9O_{34})_2]^{10-}$ and $[Co_4(H_2O)_2(\alpha\text{-}VW_9O_{34})_2]^{10-}$ polyoxometalate water oxidation catalysts revealed by soft X-ray spectroscopy

**Chapter 3:** **51**

Distorted tetrahedral $Co^{II}$ in $K_5H[CoW_{12}O_{40}]\cdot xH_2O$ probed by 2p3d resonant inelastic X-ray scattering

**Chapter 4:** **80**

In-situ 2p3d resonant inelastic X-ray scattering tracking cobalt nanoparticle reduction

**Chapter 5:** **101**

The difference between electron yield and fluorescence yield X-ray magnetic circular dichroism derived sum rule values

**Summary** 123

**Samenvatting in het Nederlands** 126

**Acknowledgements** 128

**List of publications and presentations** 131

**Curriculum Vitae** 133

Chapter 1.

# Introduction

## 1.1. SPECTROSCOPY

Spectroscopic techniques are used as methods to probe the electronic structures of a matter. Spectroscopic methods, in general, measure the response of a matter as the function of energy. The response reveals interactions between an incident energy carrier (photons, electrons or neutrons) and particles (electrons, nuclei) in matter. The response can be known via detection of in-going energy carriers and out-going particles that contain energies released after the aforementioned interactions. Detecting energies of different out-going particles are used in a number of spectroscopies and, for example, out-going X-ray photon energies are measured in resonant and non-resonant X-ray scattering, while energies of photoelectrons are detected in the X-ray photoelectron spectroscopy (XPS) and Auger electron spectroscopy (AES). In addition to visible light, many spectroscopic techniques utilize electromagnetic radiation, including infrared (IR), ultraviolet (UV), X-rays and Gamma (γ) rays. In Figure 1, the wavelength and corresponding frequency of typical electromagnetic radiation is shown. The information offered by different spectroscopies are related to the kind of transitions or excitations: in the radio wave region, Nuclear Magnetic Resonance (NMR) and Electron Spin Resonance (ESR) offer information of the spin; in the IR and microwave region, information on the change of vibrational configurations and the change of orientation, like rotations, can be detected; from visible to UV regions, the transition information of valence (outer shell) electrons are detected, which offers the valence electron excitations, such as *d-d* excitations; X-rays can yield transition information involving more tightly bounded inner shells, for example the *1s* or *2p* shells of *3d* transition metals; γ-rays can give the information on the changes of nuclear configurations.[1] In the studies of the electronic structure of *3d* transition metal materials, X-rays offer the advantage of element, valence and spin specificities, which also allows the detection of different inner shell information by tuning the X-ray energy. In this PhD thesis, we use X-ray spectroscopies, including *2p* X-ray absorption spectroscopy (XAS), X-ray magnetic circular dichroism (XMCD) and *2p3d* resonant inelastic X-ray scattering (RIXS), also known as resonant X-ray emission spectroscopy (RXES), to study the *3d* transition metal containing materials, with an emphasis on cobalt.

In this introduction first general introductions on different X-ray spectroscopies will be given, and then discussions will focus on XAS, XMCD and RIXS that are main X-ray techniques used in current thesis.

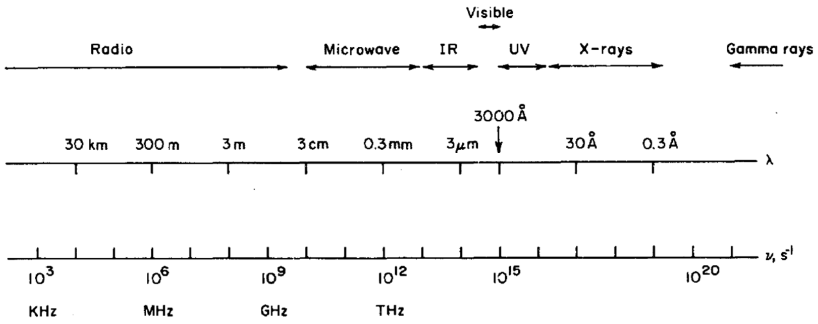


**Figure 1**. The electromagnetic spectrum. Upper panel: the type of radiations. Middle panel: wavelength; Lower panel: frequency. Adapted from Struve.[1]

## 1.2. X-RAY SPECTROSCOPY

The electromagnetic radiation that is known as X-rays was firstly discovered by Wilhelm Röntgen on the evening of 8th, November 1895. Due to this, X-rays are also named after him as Röntgen rays. During the past 120 years, X-rays played pivotal roles in the society, particularly in medicine, pharmacy, physics and chemistry. Although X-rays were originally used by physicists, it gradually became a ubiquitous tool for researches in all branches of scientific endeavor. The reasons that X-rays are so useful for investigating the properties of materials are firstly because X-rays are capable to probe non-destructively different depths in solid materials. The penetration depth of X-rays in a solid materials mainly depends on I) the energy that X-rays bring and II) the electron density of constituent elements in the sample under investigation. Typically, X-rays are with wavelengths between 10 and 0.01 nm corresponding to energies between 100 and 10 keV, and which is often divided into soft and hard X-ray regions. In the soft X-ray region, where energies are normally between 100 and 2000 eV, X-rays can be easily absorbed by air and by solid materials that often leads to the short penetration depth. For example, absorption cross sections of transition metals and rare earths can be high up to a few tenths of Å, which reduces the penetration down to around 100 Å.[2] In contrast, hard X-rays with higher energies can penetrate deeper through the air and solids.

Secondly, X-ray photons can have wavelengths comparable to those of atomic spacings (in the order of Å) in solid materials. This endows the diffraction conditions of X-rays with the crystalline arrays of atoms. Currently, lab-based X-ray diffraction (XRD) is a conventional technique to study the crystalline solids. The diffraction techniques are not discussed in this thesis, instead I focus on

X-ray spectroscopic techniques. The four main X-ray spectroscopic techniques that will be discussed are XAS, XPS, XMCD and RIXS.

It is important to mention that although laboratory X-ray sources could achieve part of spectroscopic techniques discussed here,[3] incident radiations used in this thesis are from synchrotron radiation. We therefore start with a short introduction of synchrotron radiation.

### 1.2.1. Synchrotron radiation

Synchrotrons provide an intense source of tunable X-rays, making them as an ideal place for performing X-ray spectroscopic measurements.[4] In synchrotrons, the high-energy photons are generated when electrons with relativistic speeds are passing through strong magnetic fields. The magnetic fields force electrons to travel along a curved path and during this motion, electrons lose their energies in the form of electromagnetic radiation. The emission of radiation decreases the electron energy and such energy loss needs to be compensated by radiofrequency cavities that apply the accelerating electric field synchronized with the passage of electrons.

The magnetic fields can be applied mainly by using bending magnets or insertion devices including wigglers or undulators. Each of these magnetic components has different characteristics and results in different X-ray properties. Bending magnets generate a broad spectrum from IR to X-rays, making them the general purpose photon sources at accelerators. The X-ray flux of the bending magnet X-ray spectrum depends on the strength of magnetic field as well as the energy in the synchrotron ring. Wigglers and undulators are composed of periodic arrays of permanent magnets. When passing the insertion devices, electrons are forced to follow an oscillatory trajectory due to the alternating magnetic fields, which result in a collimated, spatially intense beam of X-rays. Figure 2 shows a schematic diagram of the insertion devices, and the emitted radiation. In general, undulator beamlines produce the highest brilliance that can yield average photon fluxes exceeding $10^{12}$ photons/second.

The basic components of most beamlines are: (1) a series of valves that separate the beamline from storage rings and the different beamline components from each other; (2) focusing optics to modify the x-ray beam characteristics; (3) monochromators that are used to select the desired wavelengths; (4) detectors, such as photodiodes, charge coupled-devices (CCD) and silicon drift detectors (SDD).[6] In X-ray spectroscopy beamlines, monochromators are important components to monochromatize beams to a small $\Delta E/E$ bandwidth as for better spectral resolution. Soft X-ray monochromators (below 2 KeV) consist of a grating and hard x-ray monochromators use crystal monochromators.[7-10]

In general, synchrotron provides the electromagnetic radiation with desired wavelengths to perform spectroscopic techniques for investigating the aimed electronic structures of materials.

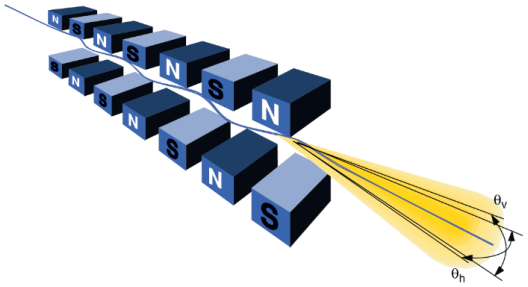


**Figure 2.** A schematic figure of an insertion device. The angular spread in radiation is given in the horizontal and vertical plane by $\theta_h$ and $\theta_v$, respectively. Adapted from Willmott.[5]

### 1.2.2. X-ray absorption spectroscopy

The absorption of electromagnetic rays in the condensed or gaseous matter is a rich phenomenon. In the absorption process, the energy of incident rays transferred that accompanies the physical, chemical or biological modifications of the matter involved. In general, the Beer-Lambert law (equation 1.1) describes an absorption process by monitoring the transmitted intensity ($I_t$) with respect to the incident intensity ($I_0$):

$$I_t = I_0 \times e^{-\mu t} \tag{1.1}$$

where the t is the sample thickness and μ is the absorption coefficient. In the case of homogenous sample, the transmitted intensity decreases exponentially in term of the sample thickness. The absorption coefficient μ describes the probability of X-rays being absorbed. The μ is element specific and a function of X-ray energies. In general, μ is approximately proportional to the $Z^4$ (Z is the atomic number of the element) and it decreases with the increase of photon energy, for which it is approximately the inverse proportion of $E^{-3}$ (shown in Figure 3). This coefficient of a crystalline solid is related to the absorption cross-section $\sigma_i$ of n different chemical elements in the unit of mega barn (1Mbarn = $10^{-18}$ $cm^2$).[11]

$$\mu = \sum_{i=1}^{n} \sigma_i \tag{1.2}$$

Usually, users are more interested in the spectral shape and energy positions of fine structures. Thus, the edge jump of absorption spectra is often normalized to one and the arbitrary unit is given.

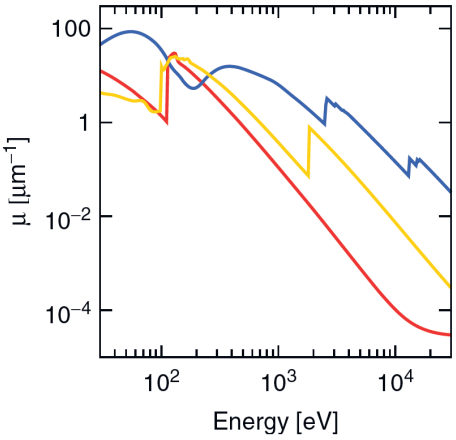


**Figure 3.** The X-ray absorption coefficient μ for beryllium (red), silicon (yellow) and lead (blue) as a function of the photon energy. Adapted from Willmott.[5]

The sharp increases shown in the Figure 3 correspond to the absorption edges, which were also initially named as white lines.[12] These increases are related to the excitations of core electrons to the unoccupied states. Thus, each absorption edge corresponds to a different core level and the corresponding X-ray energy is minimum energy to overcome the binding energy of the specified core level of the materials studied. The edges are named after the core level that is excited. The *K* edge is after the *1s* core level, $L_1$ edge is after the *2s* core level, $L_{2,3}$ edges are after $2p_{1/2}$ and $2p_{3/2}$ core levels, etc. An advantage of XAS for study the fundamental properties of a specific element is that X-ray energies are tunable to fit with the binding energy of the core-level of interest and probe detailed electronic structures with the presence of core hole plus the excited electron.

XAS is a useful tools to study atoms, molecules, adsorbates, etc., and it is widely applied in many fields such as chemistry,[13-15] physics,[16-17] biology,[18-20] and geo-sciences.[21] For example, since XAS is closely related to the unoccupied density of states, the bonding or antibonding information can be effectively known from the shape of XAS spectra. By combining with other techniques, the adsorption of atoms can be well understood, as for the example shown by Nilsson et al.[22]

X-ray absorption spectroscopy is divided into two methods: i). X-ray Absorption Near Edge Spectroscopy (XANES) and ii). Extended X-ray Absorption Fine Structure (EXAFS). The division

of the XAS spectrum into XANES and EXAFS is shown in Figure 4. The pre-edge region as shown in Figure 4 is counted as part of the XANES.

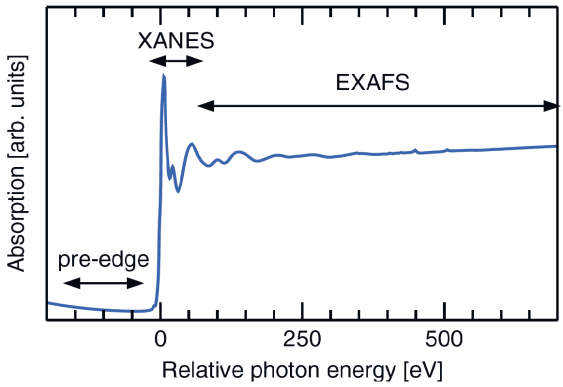


**Figure 4.** An illustration of the XAS spectrum with pre-edge region, XANES region and EXAFS region. Figure adapted from Willmott.[5]

EXAFS is not used in the rest of this thesis. The EXAFS signals contains oscillations in the X-ray absorption coefficient starting at approximately 50 eV above an absorption edge and extending up to several hundred eV. The EXAFS spectra yield information on the short range atomic structure of materials since the energy of the photoelectrons in the EXAFS region have a mean free paths at the order of a few Angstrom, which indicates the range of interactions of photoelectrons with the neighboring atoms of the absorbing atom. EXAFS is a well-established spectroscopy technique for studying the local atomic geometric structure in materials.[23]

XANES is also known as Near Edge X-ray Absorption Fine Structure (NEXAFS). The general method to discriminate XANES and EXAFS are based on the energy range, as shown in Figure 4, XANES are normally within 50 eV close to the absorption edge (white line), while EXAFS are 50 eV above the absorption edge. In this thesis, the XAS spectra we discuss are only the XANES.

Transitions in the XAS process can be effectively described by the Fermi Golden Rule:[24]

$$W_{fi} = \frac{2\pi}{\hbar} \left|\langle \Phi_f | T | \Phi_i \rangle\right|^2 \delta(E_f - E_i - \hbar\Omega) \tag{1.3}$$

The transition probability $W$ between the initial state $\Phi_i$ and final state $\Phi_f$ by absorbing the X-ray photons with energy $\hbar\Omega$ is obtained based on the equation (1.3). The delta function indicates the energy conservation and a transition takes place if the energy of the final state ($E_f$) equals the energy of the initial state ($E_i$) plus the X-ray energy. The squared matrix element gives the transition rate.[25]

For the absorption process, the first order transition operator $T_1$ that describe the one-photon transition process is obtained. The Fermi Golden rule dictate that electric dipole transition of electron states is altered in the absorption process. Electric quadruple transitions or magnetic dipole transitions are also possible, although with much lower probabilities.

### 1.2.2.1. Transition metal *2p* XAS

As stated in the above text, XAS studies on the electronic structure of materials are based on energies carried by photons that induce transitions of different core level electrons to the empty valence states. *2p* XAS that is also known as *L* edge XAS, refers to the resonant excitation of *2p* core electrons to empty *3d* states. For *3d* transition metal containing materials, the use of metal *2p* XAS allows the probe of *3d* empty states of transition metals with the modification, of the *2p* core hole. Energies of excitations used in *K*, *L* and *M* edges of the first 90 elements appearing in the periodic table are given in Figure 5, in which the soft and hard X-ray range are divided by the energy of 1 keV. For cobalt the $L_{2,3}$ edges are between 775-795 eV, which are in the soft X-ray range. For the element vanadium and iron studied in chapter 2 and chapter 5, both *2p* XAS also lie in the soft X-ray range.

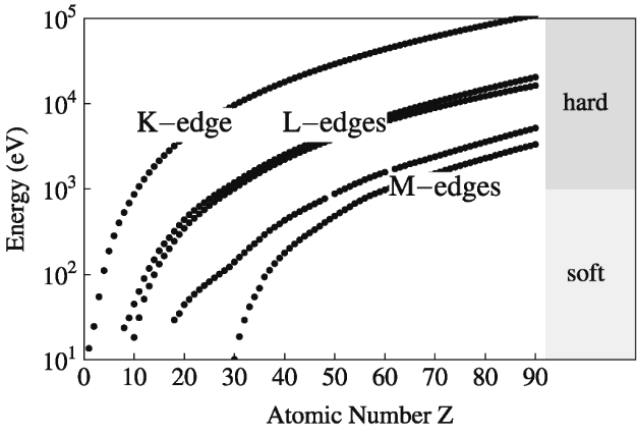


**Figure 5.** Energies of the *K*, *L* and *M* edge XAS for the first 90 elements as a function of atomic number Z. Reproduced from Ament *et al*.[26]

### 1.2.2.2. Multiplet effects in transition metal *2p* XAS

In the transition metal *2p* XAS, multiplet effects[25, 27-30] play important roles. The strong overlap between core wave function and valence wave function implies that the interaction between core

hole and the valence electrons has to be taken into account. Besides, the valence electron interactions in both initial state and final state of *2p* XAS process need to be considered. Both interactions are essentially referred as multiplet effects. Multiplet effects are important for spectroscopies where strong interactions between *3d* electrons and the empty core hole are present, for example, in the *3p* XPS, *2p3s* resonant X-ray emission and *2p3s3s* resonant Auger spectroscopies.[31-34] The transitions in the XAS processes have been successfully described by the ligand field multiplet model, which are used as the theoretical bases of current thesis. From here we discuss several basic aspects of the multiplet theory based on the books of de Groot and Kotani,[25] and the review paper of de Groot.[27] We limit the discussion to atomic multiplets and ligand field multiplets, as we did not apply charge transfer multiplets effects in the current thesis.

In the atomic multiplets, a free atom model is considered without inclusion of influence from the environment. The Hamiltonian of a free atom $H_{atom}$ can be written as:

$$H_{atom} = \sum_N \frac{P_i}{2m} + \sum_N \frac{-Ze^2}{r} + \sum_{i>j} \frac{e^2}{r_{ij}} + \sum_N \zeta(r_i)\, l_i \cdot S_i \qquad (1.4)$$

Equation (1.4) contains, respectively, the kinetic energy of electrons ($p^2/2m$), the electrostatic interaction of electrons with the nucleus ($Ze^2/r$), the electron-electron repulsion ($e^2/r$) and the spin-orbit coupling of each electron ($l \cdot s$). The first two terms in equation (1.4) are the same for all electrons in a given atomic configuration and they define the average energy ($H_{av}$) of the configuration. The last two terms, on the other hand, define the relative energy of different terms within a configuration.

The main problem in solving the Schrödinger equation is that the electron-electron repulsion is large and cannot be treated as a perturbation. But the spherical average can be separated from the non-spherical part, and the spherical average is then added to the $H_{av}$. The modified electron-electron Hamiltonian $H_{ee}^{'}$, which is the non-spherical part, together with the $H_{ls}$ determine the energy of each term within a configuration.

The symmetry labels of a configuration are indicated by the so called term symbol $^{2S+1}L_J$. The *L*, *S* and *J* are respectively the orbit moment, spin moment and total moment of the configuration, with $|L\text{-}S| \leq J \leq |L+S|$. In the absence of spin-orbit coupling, all terms with the same *L* and *S* have the same energy, giving an energy level with the degeneracy of $(2L+1)\cdot(2S+1)$. When spin-orbit coupling is considered, the terms are split in energy according to their *J* value, and each with a degeneracy of $2J+1$. In the 2p XAS process, it is crucial to understand the configuration of the $2p^53d^N$ final state. The term symbols of the $2p^53d^N$ states are found by multiplying the configuration of $3d^N$ with a $^2P$ term symbol. For $Co^{II}$, the ground state $2p^63d^7$ configuration has 120 *d*-states ($10\cdot9\cdot8/3\cdot2$), while the $2p^53d^8$ final state has 270 *pd*-states ($6\cdot10\cdot9/2$).

The term symbol describes the symmetry aspects, but the relative energies of different terms are determined by calculating the matrix elements of these states with the modified electron-electron interaction $H_{ee}^{'}$ and the spin-orbit coupling $H_{ls}$. For the modified/effective electron-electron interaction, the general formulation of the matrix element is:

$$\langle {}^{2S+1}L_J \left|\frac{e^2}{r_{12}}\right| {}^{2S+1}L_J \rangle = \sum_i f_i F^i + \sum_i g_i G^i \quad (1.5)$$

In equation (1.5), $F^i(f_i)$ and $G^i(g_i)$ are the Slater-Condon parameters for the radial (angular) part of the direct Coulomb repulsion and the exchange interaction, respectively. For *3d*-states, it is important to note that a $3d^N$ configuration contains $f_0$, $f_2$ and $f_4$ Slater–Condon parameters. The final state $2p^53d^{N+1}$ configuration contains $f_0$, $f_2$, $f_4$, $g_1$, and $g_3$ Slater–Condon parameters. Atomic multiplet theory is capable to well describe the *3d* and *4d* X-ray spectra of rare earths. For *3d* metal ions, atomic multiplet theory could not simulate the XAS accurately, due to the large effects of neighbors on the *3d* orbitals. It is necessary to induce the ligand field multiplet theory that take care the symmetry effects under the ionic limits. Charge transfer multiplets theory that accounts the delocalization of electrons are necessary for systems with stronger covalency, which are not studied in current thesis.

In ligand field multiplet (LFM) theory, the transition metal is approximated as an isolated atom, and which is surrounded by a distribution of charges. This simplistic model mimics the system, molecule or solid, around the transition metal ion, and which is extremely useful in the explanation of optical spectra. The usefulness of this simple model is that properties related to the symmetries are well considered. Group theory used in this model make the link to the atomic multiplet theory, which branches the results obtained by atomic multiplet calculation to cubic symmetry and further to the lower point groups.[35-36] More details of the LFM theory on the simulation of XAS will not be discussed here. Detailed methods are explained in the recent review papers.[25, 27]

#### 1.2.2.3. Experimental methods of transition metal *2p* XAS

In this section, the experimental methods of transition metal *2p* XAS will be discussed. The methods will be limited to the transmission detection, total electron yield detection (TEY), total fluorescence yield detection (TFY) and inverse partial fluorescence detection (IPFY). Other methods like ion yield, partial fluorescence yield and partial electron yield, etc. are not covered here. Advantages of each detection mode will be discussed and the disadvantage and the potential problems of each detection will be compared.

Transmission detection is the formal method for XAS measurements, the principle of which is based on the Beer-Lambert Law stated as in equation (1.1). In the transmission experiment, the X-ray intensity ($I_0$) is measured in the first ionization chamber or using a metallic (e.g. gold) foil to absorb some of the photons. After the X-ray interacts with the sample of interest, the photon intensity ($I_t$) is measured in the second ionization chamber or by a photodiode. Transmission measurement for XAS are standard for hard X-rays. However, for *3d* transition metals, the L edge lies in the soft X-ray range where the X-ray attenuation length is small.[37] For example, at the *2p* resonance of Fe or Co, the photon attenuation length can be down to ~20 nm that requires thin samples in transmission experiments.[14, 17] Normally, ultra-thin sample with ~100 nm thickness are required which is impractical in many studies. The advantage of transmission method is that I) it is the only detection for obtaining the absolute cross section and, II) it will not suffer effects due to yield variations. The limitation, apart from the sample thickness, is the requirement for the homogeneous sample. The pinhole effects or non-homogeneous sample could lead the distorted spectral shape, in other words a deviated absorption coefficient.

The sample thickness often limits the application of transmission method and one needs to resort to the yield methods, in which one uses the flux of secondary emission produced by the primary absorption process to measure the absorption coefficient. Among the yield methods, TEY and TFY are most generally used. In TEY, all electrons that escape from the sample surface are collected, independent on their energies. The TEY methods shows a good agreement with transmission methods in measuring the absorption coefficient.[38] The normal detection devices used for TEY methods are the pico-ampere meter that measure the drain current of the sample, or the channeltron amplifier to detect the emitted electrons. In a gaseous atmosphere with a pressure of approximately 10 mbar, the TEY measurement can detect the signal from the ionized gas molecules that is, under certain conditions, proportional to the absorption cross section. The limitation of TEY methods mainly includes the short probing depth and magnetic problems (see the discussion in chapter 5). The probing depth of TEY are due to the small electron escaping depth $\lambda_e$ in the range of approximately 2-10 nm, depending on the materials studied. In transition metal L edges, the absorption cross sections can be high which reduces energy-dependent X-ray penetration depth $l(\Omega)$ to low values, at the same range of the electron escape depth. This indicates that both electron escape depth and X-ray penetration depth can affect the measured X-ray absorption cross section, according to:

$$I_{TEY}(\Omega) \propto \frac{\lambda_e}{\lambda_e + l(\Omega) sin\theta} \tag{1.6}$$

where the $\theta$ is the angle of incidence. This implies that when $\lambda_e \ll l(\Omega)\sin\theta$, the TEY is inversely proportional to the $l(\Omega)$ sin $\theta$, which is proportional to the absorption coefficient. The saturation

effects occur when $\lambda_e$ is larger than or comparable to $l(\Omega)$ sin $\theta$.[39-40] At grazing incidence, care should be taken for this limitation. Luckily, in most cases the X-ray penetration depth are significantly larger than the electron escaping depth that suggesting saturation effects rarely occur for TEY *2p* XAS.

In addition to TEY, TFY is also a routine method for transition metal *2p* XAS detection. In TFY, one use the photodiode to measures the total fluorescence decay of the core hole after the core electron is excited by the incident X-ray. The core hole decay occurs via radiation decay of fluorescence and non-radiation decay of Auger electrons. For the core levels below 1 KeV, Auger decay dominates and fluorescence decay is less than 1%.[42] TFY detection is found to be a good measurement of the absorption cross section if the edge absorption is much less than the background absorption.[43-44] Hence, it is suitable for measuring dilute systems or impurities. The fluorescence measurements, on the contrary of TEY, are not affected by the magnetic field. For the less dilute materials, the self-absorption effects or saturation effects can happen and which lead to the distorted spectral shapes including the compressed peaks. The self-absorption is caused by the *2p* re-absorption of the escaping X-ray photons. Self-absorption effects can blur out spectral information, although the original spectrum can be reconstructed from the saturated one.[45-46]

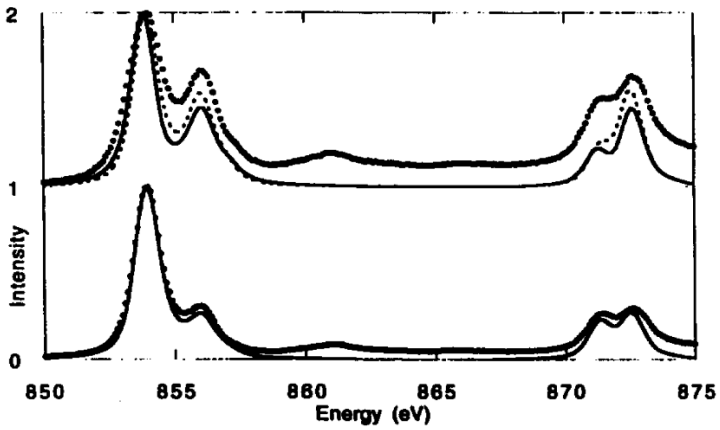


**Figure 6.** Ni *2p* XAS: experimental TEY spectrum (bottom, dots) and the TFY spectrum of $Cs[NiCr(CN)_6]\cdot 2H_2O$. The calculated spectra are presented with solid lines in both top (coherent) and bottom, and dashed line in the top (incoherent). Adapted from de Groot *et al*.[41]

Saturation effects are caused by the energy dependence of the X-ray absorption cross section. Neglecting the angular dependence, the TFY intensity can be approximated as the absorption cross section ($\mu$(E)) divided by $\mu$(E) plus the background absorption. If the energy dependent absorption

is significant, the TFY intensity is not exactly proportional but the signal is saturated at the peaks. In addition to saturation the emitted x-ray could be re-adsorbed in the material, but this self-absorption effect is usually negligible.

Beside the saturation effects, an intrinsic problem also exists in TFY XAS. The assumption for the use of the decay channels is that these channels are linearly proportional to the absorption cross section. In cases where the ratio between radiative and non-radiative decay varies significantly over an energy range, this proportionality breaks down. The reason behind is that fluorescence decay is final state dependent. The fluorescence decay varies drastically over the late transition metal L edges. It is calculated by de Groot that fluorescence decay over the $Ni^{2+}$ $L_{2,3}$ edges varies up to 400%. The Auger decay, on the contrary, only varies around ~20%.[41, 57] Note that this is also the case for the M edge of rare earth.[48] Since Auger decay dominates over the fluorescence decay in the soft X-ray range, the distortion in the spectra is only seen in the TFY XAS. For the electron yield spectra, the distortion is in the region of a few percent. Figure 6 shows the Ni *2p* XAS measured by TEY and TFY modes, and compared with the multiplet calculation results. It can be observed the TFY XAS deviates remarkably from the calculation, while the TEY is much more close to the absolute absorption cross section. This indicate that for transition metal L edge XAS, TEY can be effectively used, while the TFY are, in principle, not equivalent to the true XAS. The general trend of the distortion for transition metal *2p* TFY XAS are shown by Kurian *et al*.[49] The variation of intermediate state fluorescence lifetimes also influence the quantitative analysis results in the X-ray magnetic circular dichroism by using optical sum rules. Details of the deviation will be present in the chapter 5.

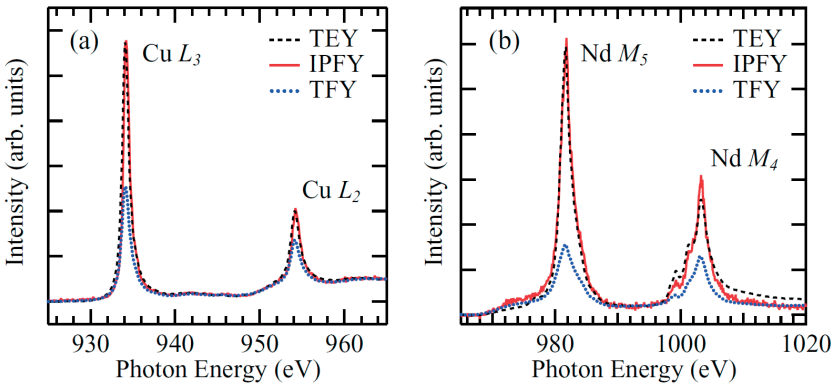


**Figure 7.** The TEY (dashed black), O K edge IPFY (red), and TFY (dotted blue) as a function of photon energy through the (a) Cu L and (b) Nd M edges. Adapted from Achkar *et al*.[50]

Recently, the IPFY[50] measurements of *2p* XAS became popular since it is both bulk sensitive and free of saturation effects. Similar to the normal PFY measurement, in IPFY, one use the energy-sensitive fluorescence detector to collect the fluorescence decay in a particular fluorescence channel. However, in IPFY, one measures the non-resonant X-ray emission spectrum (NXES) from a different element other than the absorption edge of the element that are probed with the incident photons. The principle of IPFY is different than the TEY and TFY. Both TEY and TFY measures the number of core-hole excitations over the absorption edge, while the IPFY effectively measures the X-ray attenuation depth, akin to the transmission measurements. The advantage of IPFY over TEY is the bulk sensitive, which will not be affected by the problem of surface sensitivity. The advantages over the TFY method for L edge of transition metal and M edge of rare earth are I). free of saturation effects and II). free of intrinsic distortions that are caused by the state dependent fluorescence decay as discussed above. More importantly, the source of NXES can be another element in the materials, or other core electrons in the same element in the materials. For example, when measuring V L edge in the $VO_x$, the O K NXES is not proper since the energy of V L edge is close to the energy of O K edge and the V L edge and O K edge may not be well separated unless a high energy resolution detector is used. However, this can be circumvented by choosing other NXES of both elements that have larger energy separation with the V L edge. Therefore, for transition metal *2p* XAS measurements, the IPFY is an optimal choice if the energy sensitive detector is equipped in the beamlines. Figure 7 shows the comparison of IPFY XAS with TEY and TFY results, results presented in the literature by Achkar *et al*.[50]

### 1.2.3. X-ray magnetic circular dichroism

Dichroism refers to a property of certain objects that allows them to show different colors according to their orientation with respect to the light. The mechanism is the dependence of the optical response of objects on the relative orientation between the polarization direction of the light and the symmetry axes of the object. The X-ray Magnetic Circular Dichroism (XMCD) refers to the difference between the absorption of left- and right- circularly polarized light. XMCD, by combining the advantage of spectroscopy and magnetometry, is a useful tool to understand the magnetic properties of materials or the specific element in a system. It has been widely used in the study of (bio)inorganic chemistry and materials science.[51-52] The development of optical sum rules by Thole *et al*.[53] and Carra *et al*.[54] allows the quantitative analysis of magnetic properties by using XMCD spectra. The sum rules show that the integral over XMCD signals of a given edge enables the determination of the ground state expectation values of the orbital moment $L_z$ and the effective spin moment $(S_{eff})_z$. For transition metal, the sum rule apply for a specific transition that is *2p* core state to *3d* valence states. Piamonteze et al. presented a broader theoretical investigation on the

validity of spin sum rules.[55] Experimentally, the application of sum rule for Fe and Co metal L edge XMCD have been successfully proved by Chen *et al*.[17] In that work, the *in-situ* growth of thin films allows the accuracy determination of $L_z$ and $(S_{eff})_z$ values. But for many other L edge XMCD measurement of *3d* transition metals, yield methods are needed for reasons mentioned in the 2.2.1.2 section. In particular, the TFY methods that are also used and which are assumed to be equivalent as the TEY results for XMCD quantitative analysis. The issue of state dependent decay of fluorescence yield methods actually leads to the deviation of the sum-rule-derived ground state expectation values, even the thin film without effective self-absorption effects are used. Details related to this issue is investigated in the chapter 5 in the current thesis. We note that IPFY transition metal L edge XMCD should be an optimal choice for the quantitative analysis, since it offers the advantage of bulk-sensitive and free of saturation/self-absorption effects and free of the intrinsic deviations in the measured spectra.

### 1.2.4. *2p3d* resonant inelastic X-ray scattering (RIXS)

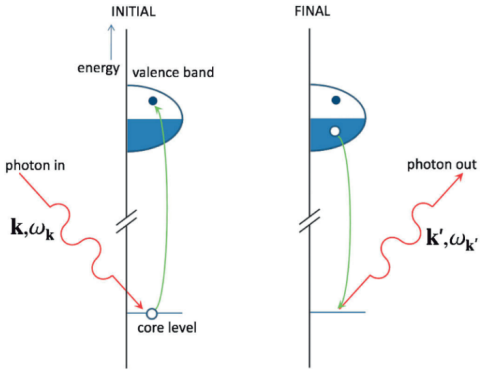


**Figure 8.** Schematics of RIXS process with photon in and photon out process. Adapted from Ament *et al*.[26]

RIXS is also known as resonant X-ray emission spectroscopy (RXES) or resonant Raman X-ray Scattering (RRXS). In RIXS, one scatters X-ray photons inelastically off matter. It is a photon-in and photon-out technique, which in principle, measures the energy, momentum and polarization change of the scattered photon. Changes in the energy, momentum and polarization of photons are transferred to the intrinsic excitations of the materials under study, and hence, the information of these excitations are obtained by RIXS. The *2p3d* RIXS are most widely applied in solid state physics.[26, 56-59] In chemistry, the application of *2p3d* RIXS on the transition metal containing materials is less developed than in physics. With the advent of beamlines with in-situ set-ups and better energy resolutions in recent years, *2p3d* RIXS promises important insights of chemical

mechanisms.[60-64] Figure 8 shows the schematic interpretation of the RIXS transitions. In *2p3d* RIXS, the X-ray photons excite the *2p* core electrons to empty 3d levels and the electrons from filled *3d* levels decay back to the empty *2p* core hole. Effectively, the final state of RIXS process shows the *d-d* excitations, as shown in Figure 9.

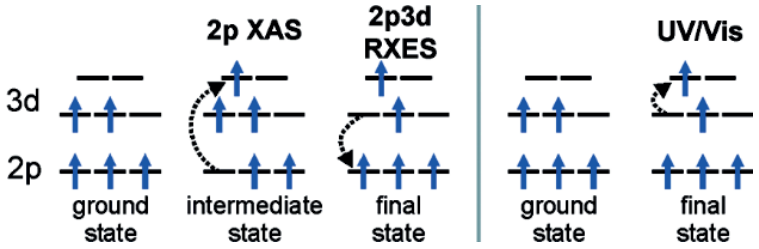


**Figure 9.** Schematic representations of the photon-induced electron transitions in *2p* XAS, *2p3d* RIXS, and UV/Vis spectroscopy. Adapted from van Schooneveld *et al*.[61]

In the decay processes of *2p3d* RIXS, the filling of *2p* core holes may results in the emission of photons (radiative decay, e.g. fluorescence) and electrons (non-radiative decay, e.g. Auger electrons). The probability of each emission are different for the K edge and $L_3$ edge resonances, as shown in the Figure 10. For *2p3d* RIXS of transition metals, excitations performed at the $L_3$ edge resonance, the fluorescent decay paths only consist of ~1% of the total decay path, which are also discussed in the section 1.2.2.3. Measurement of the radiative emissions yields the RIXS spectra. Note that RIXS is a charge neutral process, but the electrons are removed from the probed system due to the simultaneous occurrence of Auger decay process.

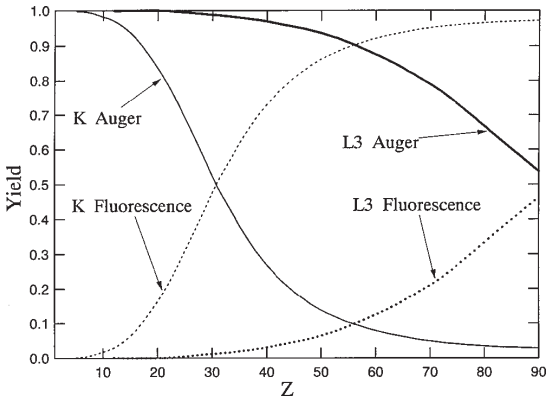


**Figure 10.** Efficiencies of x-ray emission (fluorescence) compared to the Auger yield in a series of ions having S, L, and M angular momenta. Adapted from Kotani *et al*.[56]

The *2p3d* RIXS process can be described by the resonant term of the Kramers-Heisenberg formula[25, 65] that defines the interferences between the X-ray induced *2p* core electron excitations and the subsequent fluorescent decay, given as:

$$F(\Omega,\ \omega) = \sum_f \left| \sum_i \frac{\langle \Phi_f | T_2 | \Phi_i \rangle \langle \Phi_i | T_1 | \Phi_g \rangle}{E_g + \Omega - E_i + \Phi_i \Gamma_i} \right|^2 \times \delta(E_g + \Omega - E_i - \omega) \quad (1.7)$$

where the $E_g$, $E_i$ and $E_f$ are respectively the energies of ground state, intermediate state and final state, while the $\Phi_g$, $\Phi_i$ and $\Phi_g$ are the corresponding wavefunctions. The $\Omega$ and $\omega$ represent the energies of incident and emitted X-ray photons. The $T_1$ and $T_2$ are transition operators describing the radiative transitions of absorption and emission processes, and are both with the electric dipole nature. These two operators are related to the momentum operator $T$ shown in the equation (1.3) through the correlation functions. $\Gamma_i$ describes the spectral Lorentzian broadening due to the finite lifetime of the core-hole intermediate states. The $\delta$ function indicates the energy conservation of the overall RIXS process.

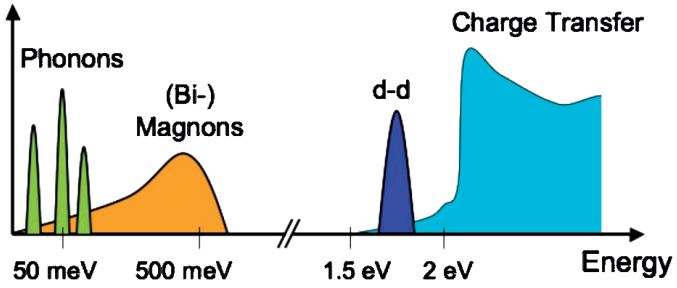


**Figure 11**. Elementary excitations in condensed matter systems and their approximate energy scales in strongly correlated electron materials. Adapted from Ament *et al*.[26]

In the RIXS process, the natural resolution is set by the final state, where in *2p3d* RIXS spectrum, it is the *3d* valance electron hole. Due to this, a significantly smaller natural/lifetime broadening should be shown in the *2p3d* RIXS spectrum than in *2p* XAS spectrum. However, the experimental resolution that often simulated by a Gaussian function also influences the total broadening of spectra. The higher experimental resolution allows the better determination of spectral features or the electronic structures, like the potential distortion of transition metal ion environment discussed in Chapter 3. Spectral features shown in RIXS spectra that correspond to elementary excitations in the probed materials are given in the Figure 11. Through different excitations, like *d-d* or charge transfer excitations, the optical properties of materials can be determined. In current thesis, we focus more on the *d-d* excitations since which are more prominent features for the systems studied.

The multiplet theory used in the interpretation of experimental results are well suited for the *d-d* excitations, also for charge transfer excitations if the charge transfer effects are included in the calculation. The low energy excitation features like phonons or magnons shown in Figure 11 are not well probed and understood due to the limited resolution in the experimental results.

### 1.2.4.1. Experimental instruments of soft X-ray RIXS

The heart of the soft X-ray RIXS beamlines and spectrometers is the diffraction grating. The energy resolution of RIXS spectra is determined by the quality of the lined grating, in which the number of lines per millimeter. RIXS is a photon hungry process, hence the bright X-ray sources are needed. Here, we limit the introduction of the experimental set-ups of soft X-ray RIXS to the beamline 05A[66] in the National Synchrotron Radiation Research Center (NSRRC), Taiwan, where the Co *2p3d* RIXS data present in the Chapter 2 and Chapter 3 were performed. The novel design of this beamline is different than many other soft X-ray beamlines, such as the ADRESS beamline[67] in Swiss light source (SLS) and 07LSU beamline[68] in SPring-8.

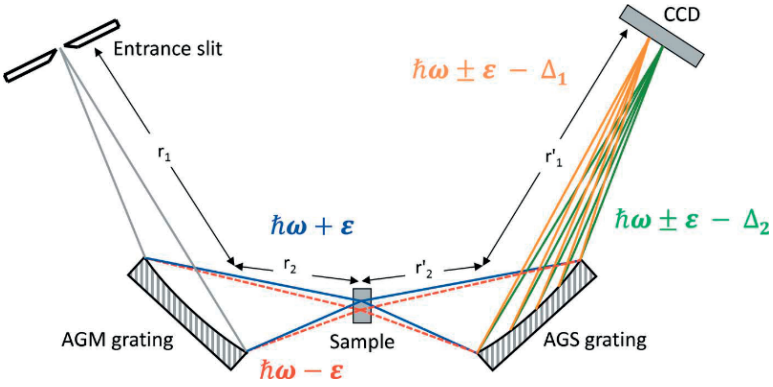


**Figure 12.** Illustration of AGM-AGS arrangement based on the energy-compensation principle of grating dispersion applied in beamline 05A, NSRRC. Adapted from Lai *et al.*[66]

In the beamline 05A, the unique design comprises two bendable gratings, termed an active grating monochromator (AGM) or active-grating spectrometer (AGS), to enhance the efficiency of measurement of inelastic X-rays through an increased bandwidth of incident photons but without smearing the energy resolution.[69] The optical arrangement of a monochromator– spectrometer design in this beamline is based on the energy-compensation principle of grating dispersion for inelastic X-ray scattering. Figure 12 shows the illustration of energy-compensation principle of grating dispersion applied in this RIXS beamline. The main important features of AGM-AGS grating arrangements are (i) the energy-loss spectra are measured through the superposition of the

inelastic X-ray scattering excited with incident X-rays of different energies within the bandwidth of the AGM and (ii) the measurement efficiency is proportional to that energy bandwidth. This design, in principle, greatly enhanced the measurement efficiency of the inelastic X-ray scattering, and which also renders the high energy resolution comparable to the ADRESS beamline in SLS. The high energy resolution allows the better obtainment of ligand field of metal center, and even see the potential distortion of the ligand field as stated in the work in Chapter 3. With the improved energy resolution in the new soft X-ray RIXS beamlines like in Taiwan Photon Source (TPS) or the beamline ID32 in European Synchrotron Radiation Facility (ESRF), the electronic structure with even higher accuracy can be achieved.

## 1.3. OVERVIEW OF THIS THESIS

In Chapter 2, we use the high energy resolution *2p3d* RIXS spectra to study the difference of electronic structures of the $Co^{II}$ sites of the tetra-cobalt core in two Cobalt-containing polyoxometalates (POMs), in which all the four Co centers are supposed to be with the distorted octahedral ($O_h$) symmetry. The ground state information of the Co are obtained by combing the Co *2p* XAS and *2p3d* RIXS spectra. The Vanadium *2p* XAS and *2p3d* RIXS are also measured to observe the postulated interactions with cobalt. The RIXS results offers the direct experimental trace of 3d orbital hybridization between Co and V centers in a cobalt and vanadium containing POM.

In Chapter 3, we report the use of Co *2p3d* RIXS to accurately probe the Co electronic structure. The energy resolution ~90 meV allows the accurate probe of the low energy *d-d* excitations, which are not possible in the optical spectroscopies for the studies of the similar Co containing materials. With the ligand field simulation on both Co *2p* XAS and Co *2p3d* RIXS experimental results, the accurate ligand field parameters are obtained.

In Chapter 4, the reduction process of carbon nanotubes supported Co Fischer-Tropsch catalysts were studied by using in-situ Co *2p* XAS and *2p3d* RIXS. The higher sensitivities of *2p3d* RIXS to the Co monoxide (CoO) than to the Co metal at the Co $L_3$ edge resonance allows the probe of minority CoO in the end of reduction process, and which are not available in the *2p* XAS. The species quantification obtained by spectral fitting procedure further suggest the ratio of CoO to Co metal revealed by *2p3d* RIXS.

In Chapter 5, although the *2p3d* RIXS technique is not directly used, in the simulations of fluorescence yield Co and Fe *2p* XAS spectra, the integrals along the incident energy of *2p3d* RIXS

plane are used. In this chapter, we discuss the difference between TEY and TFY XMCD, in particular the effects on the sum-rule-derived ground state expectation values $L_z$ and $S_z$.

## REFERENCES


(1) Struve, W.S. *Fundamental of Molecular Spectroscopy*; JohnWiley & Sons, Inc., NY, 1989.

(2) Thole, B. T.; van der Laan, G.; Fuggle, J. C.; Sawatzky, G. A.; Karnatak, R. C.; Esteva, J. M. *Phys. Rev. B* **1985**, *32*, 5107-5118.

(3) Zhang, K. L.; Lin, M. F.; Ryland, E. S.; Verkamp, M. A.; Benke, K.; de Groot, F. M. F.; Girolami, G. S.; Vura-Weis, J. *J. Phys. Chem. Lett.* **2016**, *7*, 3383-3387.

(4) Margaritondo, G. A. *J. Synchrot. Radiat.* **1995**, *2*, 148-154.

(5) Willmott, P. *An Introduction to Synchrotron Radiation*; John Wiley & Sons, Inc., Chichester, 2011.

(6) Gatti, E.; Rehak, P. *Nucl. Instrum. Methods Phys. Res. A* **2005**, *541*, 47-60.

(7) Margaritondo, G. *Elements of Synchrotron Light for Biology, Chemistry, and Medical Research*; Oxford University Press, NY, 2002.

(8) Margaritondo, G. *Introduction to Synchrotron Radiation*; Oxford University Press, NY, 1988.

(9) Matsushita, T. *X-ray monochromators, in Handbook on Synchrotron Radiation*, Vol.1, Ed. Koch, E.E.; North-Holland Publ. Co, Amsterdam, 1983.

(10) Mills, D.M. *X-ray optics for third-generation synchrotron radiation sources, in Third-Generation Hard X-ray Sources*, Ed. Mills, D.M.; John Wiley & Sons, Inc., NY, 2002.

(11) Maslen, E.N. *X ray absorption,* in *International Tables for Crystallography*, Ed. International Union of Crystallography; Springer, Heidelberg, 2006.

(12) von Bordwehr, R. S. *Ann. Phys*. (*Paris*, *Fr*.) **1989**, *14*, 377-466.

(13) Bazin, D.; Kovacs, I.; Guczi, L.; Parent, P.; Laffon, C.; De Groot, F.; Ducreux, O.; Lynch, J. *J. Catal*. **2000**, *189*, 456-462.

(14) de Smit, E.; Swart, I.; Creemer, J. F.; Hoveling, G. H.; Gilles, M. K.; Tyliszczak, T.; Kooyman, P. J.; Zandbergen, H. W.; Morin, C.; Weckhuysen, B. M.; de Groot, F. M. F. *Nature* **2008**, *456*, 222-225.

(15) de Smit, E.; Beale, A. M.; Nikitenko, S.; Weckhuysen, B. M. *J. Catal*. **2009**, *262*, 244-256.

(16) Thole, B. T.; van der Laan, G.; Fabrizio, M. *Phys. Rev. B* **1994**, *50*, 11466-11473.

(17) Chen, C. T.; Idzerda, Y. U.; Lin, H. J.; Smith, N. V.; Meigs, G.; Chaban, E.; Ho, G. H.; Pellegrin, E.; Sette, F. *Phys. Rev. Lett*. **1995**, *75*, 152-155.

(18) Wasinger, E. C.; de Groot, F. M. F.; Hedman, B.; Hodgson, K. O.; Solomon, E. I. *J. Am. Chem. Soc*. **2003**, *125*, 12894-12906.

(19) DeBeer George, S.; Metz, M.; Szilagyi, R. K.; Wang, H.; Cramer, S. P.; Lu, Y.; Tolman, W. B.; Hedman, B.; Hodgson, K. O.; Solomon, E. I. *J. Am. Chem. Soc*. **2001**, *123*, 5757-5767.

(20) George, S. J.; Lowery, M. D.; Solomon, E. I.; Cramer, S. P. *J. Am. Chem. Soc*. **1993**, *115*, 2968-2969.

(21) Mountjoy, G.; Cole, J. M.; Brennan, T.; Newport, R. J.; Saunders, G. A.; Wallidge, G. W. *J. Non-Cryst. Solids* **2001**, *279*, 20-27.

(22) Nilsson, A.; Pettersson, L. G. M.; Hammer, B.; Bligaard, T.; Christensen, C. H.; Norskov, J. K. *Catal. Lett*. **2005**, *100*, 111-114.

(23) Koningsberger, D. C.; Prins, R. *In X-ray absorption - Principles, Applications, Techniques of EXAFS, SEXAFS and XANES*; JohnWiley & Sons, Inc., NY, 1988.

(24) Dirac, P. A. M. *Proc. R. Soc. London, Ser. A* **1927**, *114*, 243− 265.

(25) de Groot, F.M.F; Kotani, A. *Core Level Spectroscopy of Solids*; CRC Press: Boca Raton, FL, 2008.

(26) Ament, L. J. P.; van Veenendaal, M.; Devereaux, T. P.; Hill, J. P.; van den Brink, J. *Rev. Mod. Phys*. **2011**, *83*, 705-767.

(27) de Groot, F. M. F. *Coord. Chem. Rev*. **2005**, *249*, 31-63.

(28) de Groot, F. M. F.; Fuggle, J. C.; Thole, B. T.; Sawatzky, G. A. *Phys. Rev. B* **1990**, *41*, 928-937.

(29) de Groot, F. M. F.; Fuggle, J. C.; Thole, B. T.; Sawatzky, G. A. *Phys. Rev. B* **1990**, *42*, 5459-5468.

(30) de Groot, F. M. F. *Chem. Rev.* **2001**, *101*, 1779-1808.

(31) de Groot, F. M. F. *Phys. Rev. B* **1996**, *53*, 7099-7110.

(32) Finazzi, M.; Brookes, N. B.; de Groot, F. M. F. *Phys. Rev. B* **1999**, *59*, 9933-9942.

(33) Taguchi, M.; Braicovich, L.; Borgatti, F.; Ghiringhelli, G.; Tagliaferri, A.; Brookes, N. B.; Uozumi, T.; Kotani, A. *Phys. Rev. B* **2001**, *63*, 245114.

(34) Braicovich, L.; Taguchi, M.; Borgatti, F.; Ghiringhelli, G.; Tagliaferri, A.; Brookes, N. B.; Uozumi, T.; Kotani, A. *Phys. Rev. B* **2001**, *63*, 245115.

(35) Weissbluth, M. *Atoms and Molecules*; Plenum Press, NY, 1978.

(36) Butler. P.H. *Point Group Symmetry Applications: Methods and Tables*; Plenum Press, NY, 1981.

(37) Henke, B. L.; Gullikson, E. M.; Davis, J. C. *At. Data Nucl. Data Tables* **1993**, *54*, 181-342.

(38) Gudat, W.; Kunz, C. *Phys. Rev. Lett*. **1972**, *29*, 169-172.

(39) Nakajima, R.; Stohr, J.; Idzerda, Y. U. *Phys. Rev. B* **1999**, *59*, 6421-6429.

(40) Vogel, J.; Sacchi, M. *J. Electron Spectrosc. Relat. Phenom*. **1994**, *67*, 181-188.

(41) de Groot, F. M. F.; Arrio, M. A.; Sainctavit, P.; Cartier, C.; Chen, C. T. *Solid State Commun*. **1994**, *92*, 991-995.

(42) Fuggle, J. C.; Alvarado, S. F. *Phys. Rev. A* **1980**, *22*, 1615-1624.

(43) Jaklevic, J.; Kirby, J. A.; Klein, M. P.; Robertson, A. S.; Brown, G. S.; Eisenberger, P. *Solid State Commun*. **1977**, *23*, 679-682.

(44) de Groot, F. M. F. *Nat. Chem*. **2012**, *4*, 766-767.

(45) Eisebitt, S.; Boske, T.; Rubensson, J. E.; Eberhardt, W. *Phys. Rev. B* **1993**, *47*, 14103-14109.

(46) Goedkoop, J. B.; Brookes, N. B.; van Veenendaal, M.; Thole, B. T. *J. Electron Spectrosc. Relat. Phenom*. **1997**, *86*, 143-150.

47. de Groot, F. M. F.; Arrio, M. A.; Sainctavit, P.; Cartier, C.; Chen, C. T. *Physica B* **1995**, *208*, 84-86.

(48) Pompa, M.; Flank, A. M.; Lagarde, P.; Rife, J.; Stekhin, I.; Nakazawa, M.; Ogasawara, H.; Kotani, A. *J. Phys. IV (France)* **1997**, *7*, 159-160.

(49) Kurian, R.; Kunnus, K.; Wernet, P.; Butorin, S. M.; Glatzel, P.; de Groot, F. M. F. *J. Phys. Condens. Matter* **2012**, *24*, 452201.

(50) Achkar, A. J.; Regier, T. Z.; Wadati, H.; Kim, Y. J.; Zhang, H.; Hawthorn, D. G. *Phys. Rev. B* **2011**, *83*, 081106.

(51) Funk, T.; Gu, W. W.; Friedrich, S.; Wang, H. X.; Gencic, S.; Grahame, D. A.; Cramer, S. P. *J. Am. Chem. Soc.* **2004**, *126*, 88-95.

(52) Funk, T.; Kennepohl, P.; Di Bilio, A. J.; Wehbi, W. A.; Young, A. T.; Friedrich, S.; Arenholz, E.; Gray, H. B.; Cramer, S. P. *J. Am. Chem. Soc*. **2004**, *126*, 5859-5866.

(53) Thole, B. T.; Carra, P.; Sette, F.; van der Laan, G. *Phys. Rev. Lett*. **1992**, *68*, 1943-1946.

(54) Carra, P.; Thole, B. T.; Altarelli, M.; Wang, X. D. *Phys. Rev. Lett*. **1993**, *70*, 694-697.

(55) Piamonteze, C.; Miedema, P.; de Groot, F. M. F. *Phys. Rev. B* **2009**, *80*, 184410.

(56) Kotani, A.; Shin, S. *Rev. Mod. Phys*. **2001**, *73*, 203-246.

(57) Haverkort, M. W. *Phys. Rev. Lett*. **2010**, *105*, 167404.

(58) Huang, H. Y.; Jia, C. J.; Chen, Z. Y.; Wohlfeld, K.; Moritz, B.; Devereaux, T. P.; Wu, W. B.; Okamoto, J.; Lee, W. S.; Hashimoto, M.; He, Y.; Shen, Z. X.; Yoshida, Y.; Eisaki, H.; Mou, C. Y.; Chen, C. T.; Huang, D. J. *Sci. Rep.* **2016**, *6*, 19657.

(59) Lee, W. S.; Lee, J. J.; Nowadnick, E. A.; Gerber, S.; Tabis, W.; Huang, S. W.; Strocov, V. N.; Motoyama, E. M.; Yu, G.; Moritz, B.; Huang, H. Y.; Wang, R. P.; Huang, Y. B.; Wu, W. B.; Chen, C. T.; Huang, D. J.; Greven, M.; Schmitt, T.; Shen, Z. X.; Devereaux, T. P. *Nat. Phys.* **2014**, *10*, 883-889.

(60) van Schooneveld, M. M.; Suljoti, E.; Campos-Cuerva, C.; Gosselink, R. W.; van der Eerden, A. M. J.; Schlappa, J.; Zhou, K. J. J.; Monney, C.; Schmitt, T.; de Groott, F. M. F. *J. Phys. Chem. Lett.* **2013**, *4*, 1161-1166.

(61) van Schooneveld, M. M.; Gosselink, R. W.; Eggenhuisen, T. M.; Al Samarai, M.; Monney, C.; Zhou, K. J. J.; Schmitt, T.; de Groot, F. M. F. *Angew. Chem., Int. Ed*. **2013**, *52*, 1170-1174.

(62) van Schooneveld, M. M.; Juhin, A.; Campos-Cuerva, C.; Schmitt, T.; de Groot, F. M. F. *J. Phys. Chem. C* **2013**, *117*, 14398-14407.

(63) Harada, Y.; Tokushima, T.; Horikawa, Y.; Takahashi, O.; Niwa, H.; Kobayashi, M.; Oshima, M.; Senba, Y.; Ohashi, H.; Wikfeldt, K. T.; Nilsson, A.; Pettersson, L. G. M.; Shin, S. *Phys. Rev. Lett*. **2013**, *111*, 193001.

(64) Suljoti, E.; Garcia-Diez, R.; Bokarev, S. I.; Lange, K. M.; Schoch, R.; Dierker, B.; Dantz, M.; Yamamoto, K.; Engel, N.; Atak, K.; Kuhn, O.; Bauer, M.; Rubensson, J. E.; Aziz, E. F. *Angew. Chem., Int. Ed*. **2013**, *52*, 9841-9844.

(65) Kramers, H. A.; Heisenberg, W. *Z.Phys.* **1925**, *1*, 681-701.

(66) Lai, C. H.; Fung, H. S.; Wu, W. B.; Huang, H. Y.; Fu, H. W.; Lin, S. W.; Huang, S. W.; Chiu, C. C.; Wang, D. J.; Huang, L. J.; Tseng, T. C.; Chung, S. C.; Chen, C. T.; Huang, D. J. *J. Synchrot. Radiat.* **2014**, *21*, 325-332.

(67) Strocov, V. N.; Schmitt, T.; Flechsig, U.; Schmidt, T.; Imhof, A.; Chen, Q.; Raabe, J.; Betemps, R.; Zimoch, D.; Krempasky, J.; Wang, X.; Grioni, M.; Piazzalunga, A.; Patthey, L. *J. Synchrot. Radiat.* **2010**, *17*, 631-643.

(68) Harada, Y.; Kobayashi, M.; Niwa, H.; Senba, Y.; Ohashi, H.; Tokushima, T.; Horikawa, Y.; Shin, S.; Oshima, M. *Rev. Sci. Instrum.* **2012**, *83*, 013116.

(69) Fung, H. S.; Chen, C. T.; Huang, L. J.; Chang, C. H.; Chung, S. C.; Wang, D. J.; Tseng, T. C.; Tsang, K. L. *AIP Conf. Proc.* **2003**, *705*, 655−658.

Chapter 2.

# Transition metal sites in $[Co_4(H_2O)_2(\alpha\text{-}PW_9O_{34})_2]^{10-}$ and $[Co_4(H_2O)_2(\alpha\text{-}VW_9O_{34})_2]^{10-}$ polyoxometalate water oxidation catalysts revealed by soft X-ray spectroscopy

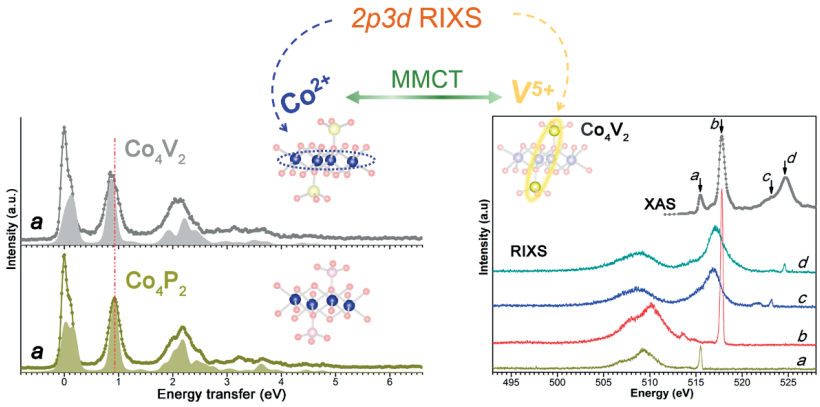


Two iso-structural cobalt containing polyoxometalate water oxidation catalysts $[Co_4(H_2O)_2(\alpha\text{-}PW_9O_{34})_2]^{10-}$ (**$Co_4P_2$**) and $[Co_4(H_2O)_2(\alpha\text{-}VW_9O_{34})_2]^{10-}$ (**$Co_4V_2$**) reveal large deviations in catalytic performances. The substitution of phosphorous centers in **$Co_4P_2$** with vanadium centers in **$Co_4V_2$** leads to electronic structure modifications. The role of vanadium centers for the redox chemistry was theoretically predicted, but without direct experimental evidences. We use soft X-ray absorption and resonant X-ray inelastic scattering spectra to investigate the ground state electronic structures of transition metal (cobalt and vanadium) sites in both **$Co_4P_2$** and **$Co_4V_2$**. High energy resolution spectral results reveal a smaller ligand field of the tetra-cobalt core, and the cobalt to vanadium charge transfer in **$Co_4V_2$**. The direct observation on the hybridization of cobalt and vanadium 3d orbitals, although in the ground state, brings insights for further understanding the potential electron transfer routes in **$Co_4V_2$** under catalytic conditions.

## 2.1. INTRODUCTION

Transition metal containing materials, due to partially filled 3d bands, are extensively used as candidates for new catalytic routes. For example, various supported iron and cobalt materials are used as catalysts for Fischer-Tropsch synthesis.[1-6] Activities of catalysts such as breaking intermolecular bonds and forming new ones can be correlated to electronic structures of the containing transition metals.[7] Hence, it is often relevant to understand a catalyst from its transition metal sites. In catalysis, one consensus goal is to harness solar energy and water oxidation stays as a central thrust in the production of solar fuels via water splitting or carbon dioxide reduction.[8-10] The oxidation of water ($2H_2O \rightarrow O_2 + 4H^+ + 4e^-$) is a highly demanding step and it requires the coupling of four electron and proton transfers together with the formation of the oxygen bond. Recently, a series of viable homogenous water oxidation catalysts (WOCs) with polyoxometalate (POM) ligands that stabilize the nuclear transition metal cores have been developed.[5-6, 11-17] This family of WOCs are carbon-free, hydrolytically and oxidatively stable. Among them, the earth abundant cobalt or nickel containing POM catalysts[5-6, 13, 16-17] how potentials of use on a realistic scale. In particular, the tetra-cobalt POM catalyst $[Co_4(H_2O)_2(\alpha\text{-}PW_9O_{34})_2]^{10-}$ (**$Co_4P_2$**), firstly reported by Yin *et al*.,[5] exhibited high photocatalytic performances such as the ~5 $s^{-1}$ turnover frequency (TOF) and high $O_2$ evolution quantum yields.[13] The later reported[6] $[Co_4(H_2O)_2(\alpha\text{-}VW_9O_{34})_2]^{10-}$ (**$Co_4V_2$**) POM catalyst, an isostructural vanadium-centered analogue of **$Co_4P_2$**, furthermore, showed superior catalytic performances with TOF up to ~$10^3$ $s^{-1}$. Such a large catalytic difference intriguingly calls for examining the 'magic roles' of substituting phosphorous centers in **$Co_4P_2$** with vanadium centers in **$Co_4V_2$**. Importantly, both **$Co_4P_2$** and **$Co_4V_2$** are proved to be the dominant active catalysts, with high hydrolytic and oxidative stabilities in aqueous conditions.[6, 18-19] Therefore, the ground state electronic structures of both catalysts, although vary from electronic structures under catalytic conditions, bring insights to understand their potential electron transfer routes related catalytic properties.

In previous work,[5-6] the electronic structure of **$Co_4P_2$** and **$Co_4V_2$** has been discussed based on experimental results of UV-vis spectra and magnetism studies. In addition, density functional theory (DFT) calculations suggested the role of $VO_4$ orbitals in molecular orbitals of **$Co_4V_2$**. However, questions are raised about: (1) how different electronic structures of the tetra-cobalt core as a whole in these two POMs are? (2) Whether the theoretically predicted hybridization between cobalt and vanadium 3d orbitals can be experimentally observed? The point (1) is interested in based on the original work[5] of **$Co_4P_2$** catalyst, in which other cobalt containing POMs with different cobalt core structures than **$Co_4P_2$** were tested to be catalytically inactive, implying the importance of the whole tetra-cobalt core. In **$Co_4P_2$** and **$Co_4V_2$**, geometrical structures of both tetra-cobalt

cores are quite similar, albeit small deviations in cobalt-oxygen bond lengths and cobalt-oxygen-cobalt angles,[5-6] but connections with heteroatoms (phosphorus or vanadium) may also affect the ligand field related cobalt 3d electronic states of the whole tetra-cobalt core. For the point (2), the charge transfer between partially filled cobalt 3d orbitals and empty vanadium 3d orbitals in **$Co_4V_2$**, if observable, should support the predicted role of vanadium centers for assisting the redox chemistry. To answer these two questions, we propose to investigate transition metal sites in both POMs (cobalt in **$Co_4P_2$** and cobalt, vanadium in **$Co_4V_2$**), by X-ray absorption spectroscopy (XAS) and resonant inelastic X-ray scattering (RIXS). Specifically, the 2p ($L_{2,3}$ edge) XAS and the corresponding 2p3d RIXS with smaller final state lifetime broadenings at this edge and better instrumental resolution are selected.[20-22]

Combined advantages of using transition metal 2p XAS and 2p3d RIXS to address the two concerned issues are: (a) both X-ray spectra are element-specific that enable separate probes on a transition metal element of interest. Hence, a direct comparison on electronic structures of the tetra-cobalt core in **$Co_4P_2$** and **$Co_4V_2$** is achievable. (b) Both techniques are sensitive to the ligand field. Especially, the 2p3d RIXS is capable to demonstrate the ligand field influenced 3d-orbital rich states with a high accuracy.[20, 22-24] (c) 2p3d RIXS allows the clear observation of, in addition to d-d transitions and ligand-metal interactions, metal-metal charge transfer (MMCT).[25-27] We notice that MMCT features assigned in UV-vis spectra[28] are often either not well understood or just the ligand-metal charge transfer or d-d transition features. (d) Transition metal 2p XAS and 2p3d RIXS spectra can be reliably interpreted by multi-electron theories.[29-36] In this work, we measure the cobalt and vanadium 2p XAS and 2p3d RIXS spectra with high experimental energy resolution (*vide infra*). Cobalt experimental spectra are simulated via ligand field multiplet (LFM) methods, by which the detailed cobalt 3d electronic states can be approached. The vanadium data of **$Co_4V_2$** confirms the previous reported[6] valence state (5+, $3d^0$) of the two iso-vanadium centers. The possible beam induced effects on vanadium XAS and RIXS spectra are discussed. From vanadium 2p3d RIXS spectra, the cobalt-vanadium charge transfer in **$Co_4V_2$** is rationalized by combining a model calculation on the $3d^1$ (vanadium 4+) ion. Finally, the cobalt and vanadium spectra indicate the complementary information on the differences of ground state electronic structures in **$Co_4P_2$** and **$Co_4V_2$**.

## 2.2. EXPERIMENTAL

### 2.2.1. Materials.

$Na_{10}[Co_4(H_2O)_2(PW_9O_{34})_2]\cdot 27H_2O$ (**$Co_4P_2$**) and $Na_{10}[Co_4(H_2O)_2\ (VW_9O_{34})_2]\cdot 35H_2O$ (**$Co_4V_2$**) were both synthesized according to the published procedures.[5-6] The obtained **$Co_4P_2$** sample are purple needle-like crystals and the **$Co_4V_2$** sample are greenish-brown needle like crystals. Identities and purities of each POM were confirmed with UV-vis and infrared spectroscopy. Infrared spectra (2% by weight in KBr) were recorded on a Nicolet 6700 FT-IR spectrometer. UV-vis spectra were acquired of ~1 mM aqueous solutions using an Agilent 8453 spectrophotometer equipped with a diode-array detector and Agilent 89090A cell temperature controller unit. Characterizations by UV-vis and FT-IR are provided in Figures S1 and S2 in the Supporting Information (SI).

### 2.2.2. XAS and RIXS Measurements.

Cobalt and vanadium 2p XAS spectra were acquired at the soft X-ray WERA beamline in ANKA synchrotron, Germany. Both crystal POMs were ground to powder and glued on the sample holders. Sample colors were checked to be identical prior and post the glue as well as after XAS measurements. Before the XAS acquisition, the instrumental resolution was calibrated to be ~280 meV full width at half-maximum (fwhm) at 780 eV and ~150 meV fwhm at 510 eV. The cobalt 2p XAS spectra were measured with the total electron yield (TEY) method at room temperature (RT, ~300 K) and the total fluorescence yield (TFY) method at 50 K. The vanadium 2p XAS spectra were obtained with the TEY method at RT. For both TEY and TFY acquisition, the normal incidence was used. All XAS spectra present are averaged from several spectra. Each single spectrum was acquired at a new pristine sample position. For vanadium XAS acquisitions, the defocused mode with a large beam spot size (500×500 $\mu m^2$) was used in order to reduce the possible beam induced damages on the sample.[37-39] No visible beam damage effects were found by comparing spectral shapes of each single spectrum.

Cobalt RIXS spectra were measured at beamline 05A1 in National Synchrotron Radiation Research Center (NSRRC), Taiwan.[40] The powdered samples were pressed in to pellets and attached to copper sample holders. FT-IR spectra of the prior-post pellet formation for both samples indicated no molecular structure change. Cobalt 2p XAS spectrum was acquired in a low energy resolution (~0.5 eV fwhm) TFY mode to match ANKA data for RIXS excitation energy determinations. The energy resolution of the RIXS elastic (zero energy transfer) peak was calibrated to be ~90 meV fwhm, around the cobalt $2p_{3/2}$ edge (~780 eV). The linear horizontally (LH) polarized beam with incident angle ~70$^o$ with respect to the sample surface was used. The scattering angle between incoming and out-going X-rays was set to be 90$^o$. The present cobalt RIXS spectra consist of the sum of 60-90 RIXS spectra (1 minute acquisition time each). A new pristine sample position was changed for every 30 min, a time frame in which no beam damage effects were observed in prior-

post comparative RIXS measurements. The pressure and temperature during all data acquisition were $<1.0 \times 10^{-8}$ mbar and 16 K respectively.

Vanadium XAS and RIXS spectra of **$Co_4V_2$** were measured at the HORNET endstation,[41] BL07LSU,[42] SPring-8 synchrotron, Japan. The powdered sample was also pelletized and attached to sample holders. Vanadium 2p XAS spectra were obtained with the TEY mode. The beam spot size used was $20\times40$ $\mu m^2$. The XAS spectrum was used to match the data acquired in ANKA to determine excitation energies. Beam induced effects observed from vanadium XAS spectra are discussed as shown in Figure S3. For RIXS measurements, the X-rays with LH polarization were applied and the scattering angle between in-coming and out-going X-rays was 90°. The incident angle of X-rays w.r.t the sample surface was 45°. The energy resolution of RIXS elastic peak was fitted to be ~204 meV fwhm at 510 eV. The vanadium RIXS spectra present were acquired in 5400-7200 s. During RIXS measurements, a scan mode was used, under which the sample surface shinned by X-rays changed to a previously non-irradiated spot every 10 s. The pressure and temperature during XAS and RIXS acquisition were $<5.0 \times 10^{-9}$ mbar and RT respectively.

## 2.3. THEORETICAL BASIS

LFM calculations are performed to simulate the cobalt XAS and RIXS spectra. The LFM codes used in this work are the Cowan-Butler-Thole's code,[43-45] which allows the description of transitions in XAS and RIXS spectra using atomic multiplet, ligand field and superexchange fields. Since cobalt centers in both POM samples are in the 2+ oxidation states,[5-6] effects of ligand charge transfer are neglected resulting in the single $2p^63d^7$, $2p^53d^8$ and $2p^63d^8\underline{d}$ electron configuration descriptions of initial, intermediate (final for XAS) and final state of RIXS process, respectively. Here, the $3d^8\underline{d}$ notation is preferred than the $3d^7$ notation to indicate the possible d-d transitions. Also, in contrast to the X-ray photoemission spectroscopy (XPS), both XAS and RIXS processes are *charge-neutral* that implies minor charge transfer effects need to be considered. Moreover, because d-d transitions are the dominant features in cobalt 2p3d RIXS spectra, the role of vanadium 3d orbitals are neglected in simulations of cobalt spectra. We note that the LFM calculation contains a number of empirical parameters that can effectively describe the electron-electron (2p3d and 3d3d) interactions, spin-orbit couplings and the ligand field splittings.[21, 23-24, 46] Such approach captures the essence of XAS and RIXS processes, and which is capable to give us relatively precise insights of the 3d-orbital rich states. The RIXS simulations are based on the Kramers-Heisenberg equation.[21, 47] and the interference effects between the core excited process and the radiative decay process in RIXS are taken into account. The LH polarization is calculated using the summation of [$\sigma_{in}$ to $\pi_{out}$] and [$\pi_{in}$ to $\sigma_{out}$] polarizations. The simulated transitions are convoluted with a

Lorentzian and a Gaussian function to account for the lifetime and the instrumental-induced broadenings respectively. In the simulation of TEY XAS spectra, Boltzmann weighted states are included to account for the room temperature populated states. The TFY XAS spectra are simulated by integrating the 2p3d RIXS plane along the incident energy, since the 2p3d X-ray emission channel is the most dominant radiative channel and other channels such as the 2p3s and 2p4s are much weaker.

## 2.4. RESULTS AND DISCUSSION

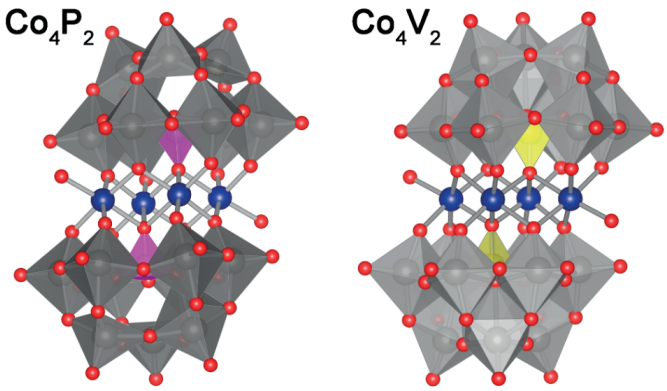


**Figure 1.** X-ray crystal structures of **$Co_4P_2$** (left) and **$Co_4V_2$** (right) in polyhedral representations. Red: oxygen; blue: cobalt; purple: $PO_4$; yellow: $VO_4$; gray: $WO_6$.

Figure 1 shows the X-ray crystal structures of **$Co_4P_2$** and **$Co_4V_2$** in polyhedral representations. The corresponding ball-and-stick representations are shown in Figure S4. Previous crystallographic characterizations have proven the two POMs to be isostructural.[5-6] In both POMs, two trilacunary B-type $[XW_9O_{34}]^{9-}$ (X= P or V) ligands sandwich a tetra-cobalt core $[Co_4O_{14}]$. All four cobalt centers in the tetra-cobalt core are octahedrally ($O_h$) coordinated, albeit with small tetragonal ($D_{4h}$) distortions. The four centers are divided into two equal inner and two equal outer atoms. The inner two centers both connect to two heteroatoms (P or V) via two oxygen bridges; while each outer center connects to only one heteroatom via an oxygen bridge; connections between each outer and inner centers are mediated by two oxygen bridges. Besides, the outer two cobalt centers are solvent accessible and each bears one terminal aqua (water) ligand. Moreover, two $PO_4$ (or $VO_4$) units are equally with approximately tetrahedral structures. Thanks to the symmetric geometry, measuring the element-specific XAS and RIXS reflects 3d electronic states of (I) average one inner and one

outer cobalt centers from cobalt spectra, and (II) equally single vanadium center from vanadium spectra.

Cobalt 2p XAS spectra of both POMs from ANKA synchrotron acquired with the high energy resolution are analyzed, and Figure 2 shows the $2p_{3/2}$ part of experimental and calculated results (see Figure S5 and S6 for full experimental spectra). The noticeable shape deviations between experimental TEY (Figure 2 left) and TFY (Figure 2 right) spectra, e.g. the lower peak intensity of the second peak (~778.4 eV), are mainly caused by the large variations in intermediate state fluorescence decay probabilities,[48-49] . Measuring at low temperature (50 K in this case) directly probes the lowest lying ground state; while measuring at RT, contributions of Boltzmann weighted excited states are also included. In general, cobalt XAS spectral shapes of both $\mathbf{Co_4V_2}$ and $\mathbf{Co_4P_2}$ measured with either TEY or TFY mode are highly similar, in correspondence with the isostructural tetra-cobalt core geometries. From the TEY spectra, small variations of peak

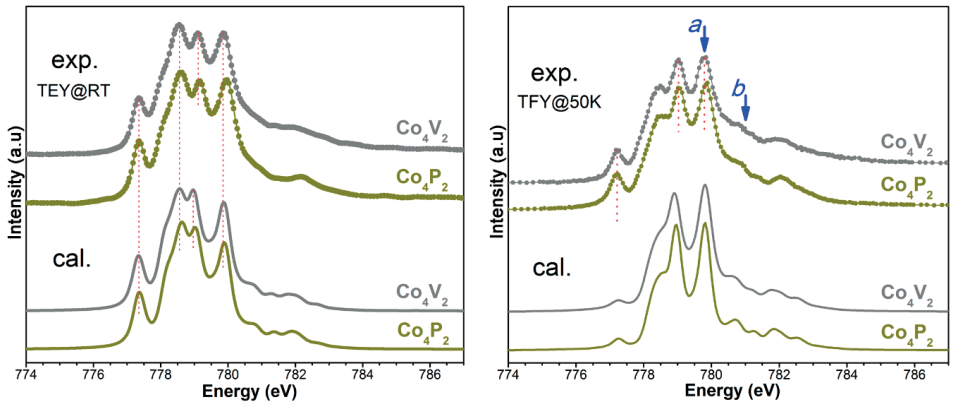


**Figure 2.** Cobalt $2p_{3/2}$ XAS spectra of $\mathbf{Co_4V_2}$ (gray) and $\mathbf{Co_4P_2}$ (dark yellow). Left upper and lower: experimental TEY spectra acquired at RT and corresponding calculated spectra. Right upper and lower: experimental TFY spectra acquired at 50 K and corresponding calculated spectra. Arrows *a* and *b* indicate excitation energies of 2p3d RIXS spectra in Figure 3. Red dotted lines indicate peak positions. Experimental data were all acquired in ANKA.

positions, such as the second left (~778.4 eV) or the fourth left (~779.8 eV) peak, can be seen that may imply the possible symmetry or ligand field related differences of multiplet states. Whereas these differences are less visible in TFY spectra. It is noted that (1) XAS spectra alone are often inadequate to demonstrate different electronic structures accurately (see the example shown in Figure S7) and (2) the same XAS spectrum can be theoretically explained with different LFM parameter values.[23] The simulation of XAS spectra use the same set of parameters determined from simulations of 2p3d RIXS spectra, as listed in Table 1. Here, the calculated results adequately

reproduce the experimental spectra, in particular the peak positions as compared in TEY spectra, suggesting the validity of electronic structure parameters found. Since 2p3d RIXS is known to be more sensitive to d-orbital rich states and simulations of RIXS spectra set the LFM parameters, we focus more on the discussion of cobalt 3d electronic states shown from the RIXS side.

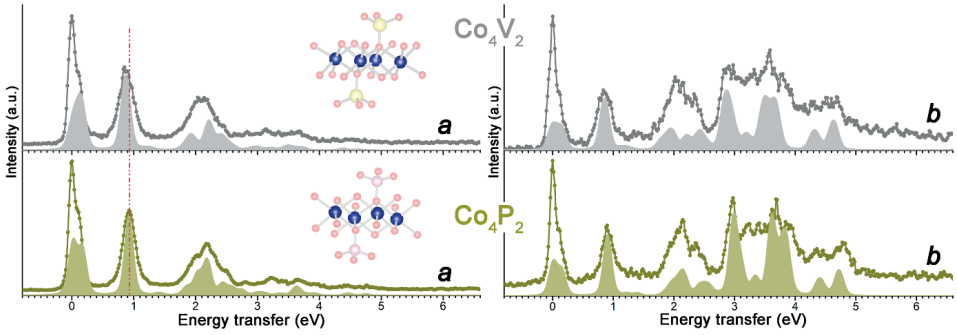


**Figure 3.** Experimental (dots+line) and calculated (fillings) cobalt 2p3d RIXS spectra of **$Co_4V_2$** (gray, upper panels) and **$Co_4P_2$** (dark yellow, lower panels) acquired at excitation energies *a* (left panels) and *b* (right panels) as indicated in Figure 2. Insets of left panels are the X-ray crystal structures of the tetra-cobalt core [$Co_4O_{14}$] together with two [$VO_4$] or [$PO_4$] units in ball-and-stick representations. Blue balls represent cobalt atoms and the faded red, yellow and pink balls represent oxygen, vanadium and phosphorous atoms, respectively. The red dotted line indicates the first d-d peak position. Experimental data were all acquired in NSRRC.

In Figure 3, the experimental cobalt 2p3d RIXS spectra acquired in NSRRC with ~90 meV instrumental resolution are present together with the calculated results. Excitation energies *a* and *b* as shown in Figure 2 were chosen for the RIXS acquisition of both POMs. The RIXS spectral shapes and features of **$Co_4V_2$** and **$Co_4P_2$**, similar as XAS analogues, resemble each other and from which the high spin (cobalt $3d^7$, S= 3/2) ground state of cobalt centers are obtained.[50-51] Nevertheless, a deviation of the lowest peak (~0.9 eV) position, corresponding to the d-d transition of the ground state $^4T_{1g}$ to the $^4T_{2g}$ state (term symbols denoted under the $O_h$ symmetry assumption and without effects of superexchange *M* and 3d spin-orbit coupling $\mathbf{L}\cdot\mathbf{S}_d$), is obviously observed. This unequivocally indicates the different ligand field strength of the tetra-cobalt core in two POMs. The ligand field strengths of **$Co_4V_2$** and **$Co_4P_2$** are described by the respective 10Dq values of 0.87 eV and 0.93 eV, and also a -0.005 eV Dt value for **$Co_4V_2$** (see the Table 1). The slightly tetragonal distortions shown in both tetra-cobalt cores are described by the Ds and Dt parameters used in LFM simulations. The tetragonal distortions mainly determined by the geometries between cobalt and oxygen atoms, including bond distances and angles, have been revealed in the X-ray crystallographic data.[5-6] The ligand field strength and the related cobalt 3d electronic states,

however, were less effectively shown in the cobalt 2p XAS spectra (*vide supra*) in this work. In 2p3d RIXS spectra, due to the ionic nature of cobalt (2+) atoms, d-d transitions are considerably probed with few (ligand to metal or metal to metal) charge transfer contributions to the spectral features, from which more accurate ligand field strength and 3d electronic states can be then obtained. The d-d transitions that represent a type of long-lived recombination center and, further, involve charge carriers localized to the metal center, are expected to be important for photocatalytic processes.[52] Here, it still remains unclear for us whether the direct relationship between the small differences of d-d transitions, hence the 3d electronic states, and the large differences of catalytic properties shown by **$Co_4V_2$** and **$Co_4P_2$** can be built.

**Table 1.** Electronic structure parameter values used in LFM simulations of 2p XAS and 2p3d RIXS spectra of both **$Co_4V_2$** and **$Co_4P_2$**. Parameter values of the RIXS final state is equivalent to the corresponding initial state and which is not shown in this Table.

| Parameters (eV) | Initial state<br>**$Co_4V_2$ / $Co_4P_2$** | Final state (XAS) & Intermediate state (RIXS)<br>**$Co_4V_2$ / $Co_4P_2$** |
|---|---|---|
| $F^2_{dd}$ | 10.005 / 10.145 | 10.716 / 10.856 |
| $F^4_{dd}$ | 6.709 / 7.397 | 7.208 / 7.908 |
| $F^2_{pd}$ | | 7.260 / 7.260 |
| $G^1_{pd}$ | | 4.857 / 4.857 |
| $G^3_{pd}$ | | 3.069 / 3.069 |
| $\mathbf{L}\cdot\mathbf{S}_d$ | 0.066 / 0.066 | 0.083 / 0.083 |
| $\mathbf{L}\cdot\mathbf{S}_p$ | | 9.748 / 9.748 |
| 10Dq | 0.870 / 0.930 | 0.870 / 0.930 |
| Ds | 0.040 / 0.050 | 0.040 / 0.050 |
| Dt | -0.005 / 0.000 | -0.005 / 0.000 |
| $M$ | 0.0003 / 0.0003 | 0.0003 / 0.0003 |

In the LFM calculations of cobalt RIXS spectra, the superexchange values used are referred to the modeling results on magnetic studies.[6] The exchange interactions between cobalt centers are different corresponding to the different types of mediated oxygen bridges, and the values are also slightly different in **$Co_4V_2$** and **$Co_4P_2$** due to variations of geometries. Effects of such subtle deviations (e.g. $2.61 \times 10^{-4}$ eV for **$Co_4V_2$** and $2.99 \times 10^{-4}$ eV for **$Co_4P_2$**) on the X-ray spectra, however, are too minor to be detected. Thus, the same values are used for both POMs. Atomic values of spin-orbit coupling (both $\mathbf{L}\cdot\mathbf{S}_p$ and $\mathbf{L}\cdot\mathbf{S}_d$) for cobalt (2+) ions are used for both tetra-cobalt cores. The ligand field parameters (10Dq, Ds and Dt) are determined mainly based on the position of the first d-d excitation peak ~0.9 eV, similar to a few other cobalt 2p3d RIXS studies.[24, 51] The Slater integrals that describes the multi-electron coulomb and exchange interactions are related to the ion covalency (e.g. the nephelauxetic effect), and which were firstly reduced to 80%

of their Hartree-Fock values. Fine tunes of $G_{pd}$ and $F_{dd}$ are further performed in the current work to improve the theoretical match to experimental results. In particular, here the reductions of $F^2_{dd}$ and $F^4_{dd}$ coulomb Slater integrals from their Hartree-Fock values vary from the fixed classical ratio,[44] followed the arguments offered in prior work of Schmidtke[53] and Hunault *et al*.[54] The calculated RIXS 2D map of **$Co_4V_2$** and **$Co_4P_2$** are present in Figure S8.

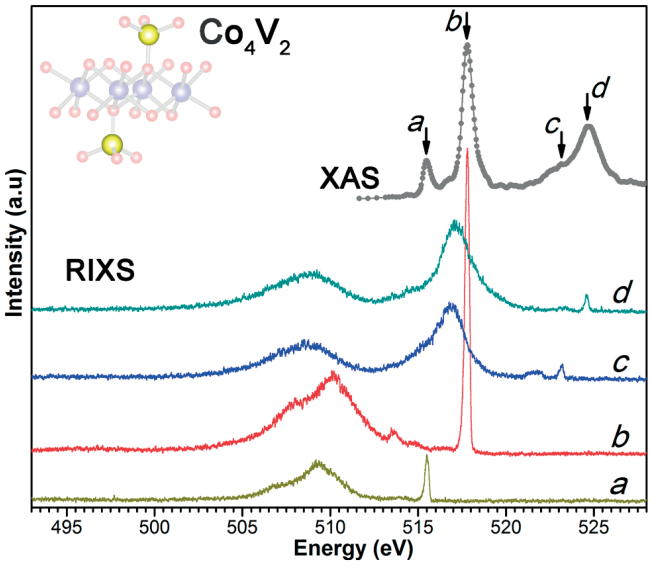


**Figure 4.** Experimental vanadium 2p XAS and 2p3d RIXS spectra of **$Co_4V_2$**. Excitation energies *a-d* of RIXS spectra are indicated by arrows on the XAS spectrum. Insets is the X-ray crystal structures of the tetra-cobalt core [$Co_4O_{14}$] together with two [$VO_4$] units in ball-and-stick representation. Yellow balls represent vanadium atoms and the faded red and blue balls represent oxygen and cobalt atoms respectively. The XAS spectrum was acquired in ANKA and RIXS spectra were measured in SPring-8.

To understand the roles of vanadium centers in **$Co_4V_2$**, vanadium electronic structures are also investigated by the X-ray spectra as shown in Figure 4. Previous bond valence sum (BVS) calculations[6] revealed that vanadium centers are in the 5+ oxidation state, suggesting the empty valence orbital ($3d^0$) nature. Clearly, the spectral shape of transition metal 2p XAS is strongly correlated to the coordination environment and number of 3d electrons of the metal center.[55] The 2p XAS spectrum of two iso-pseudotetrahedral vanadium centers in **$Co_4V_2$** (in Figure 2) is, indeed, remarkably similar as a series of $3d^0$ transition metal counterparts shown in literatures,[38, 56-58] which confirms the BVS calculation result. We note that vanadium (5+) centers can suffer from the soft X-ray induced effects, such as the photoreduction that lead to the change of vanadium oxidation state to 4+.[59] In the current work, we compare the XAS spectra measured in ANKA with a defocus

mode and the spectra in SPring-8 with the normal mode (smaller beam size than in ANKA, see the Experimental Section). The spectra comparison is shown in Figure S3. Considering the difference of flux density (photon $s^{-1}$ $\mu m^2$)[39] in the two beamlines and the prominent change of the spectral shape, we believe that spectra acquired in SPring-8 are with presence of vanadium 4+ in the sample due to the beam induced photoreduction; while for the ANKA XAS data in Figure 2, though it is hard to fully exclude the photoreduction effects, the spectrum dominantly reveals features of the vanadium 5+ ions. Selections of excitation energies *a-d* for RIXS acquisitions, however, were not affected by photoreduction effects shown in XAS data acquired in SPring-8.

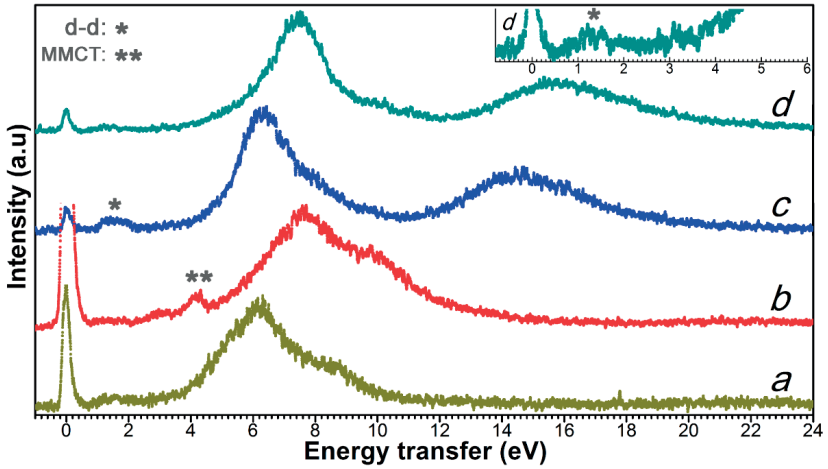


**Figure 5.** Vanadium 2p3d RIXS spectra acquired at excitation energies *a-d*, plotted as the energy transfer spectra. The inset shows the low energy transfer range of the RIXS spectrum acquired at the excitation energy *d*. One grey asterisk indicates the d-d excitation. Two grey asterisks indicate the MMCT.

The vanadium sites in $\mathbf{Co_4V_2}$, unlike the cobalt centers, are highly covalent, where charge transfer effects between oxygen ligand and metal centers are non-negligible. The ground state can be effectively described as a mixture of $3d^0$ and $3d^1\underline{L}$ configurations, where the $\underline{L}$ stands for a hole in the oxygen ligand 2p band. Note that the $3d^2\underline{L}^2$ configuration is ignored here. Similar configuration mixtures are also present in the intermediate and final states of the 2p3d RIXS process. Within the configuration interaction model, four main peaks (corresponding to excitation energies *a-d*) in the XAS spectrum have mostly the $e_g$- (peak *a* and *c*) and $t_{2g}$- (peak *b* and *d*) like characters.[38, 60] For vanadium (5+) ions, the 2p XAS final state comprises one or two electrons ($3d^1$, $3d^2\underline{L}$), in which multiplet effects must be taken into account; on the contrary, the initial and final states of the 2p3d RIXS process have either zero or one electron ($3d^0$, $3d^1\underline{L}$) where multiplet effects are much less significant. Moreover, the absence of filled 3d states implies the absence of d-d transitions features.

Thus, a more transparent observation on the bound electronic states, e.g. charge transfer, of vanadium (5+) is expected from RIXS results than from the XAS spectrum.

For both RIXS spectra acquired with excitation energies *a* (= 515.5 eV) and *b* (= 517.8 eV) at $2p_{3/2}$ absorption edge, a broad inelastic feature can be observed, with the respective energy transfer (see Figure 5) maximum of ~6.3 eV and ~7.5 eV. Similarly, a shoulder is shown on the lower energy side of each inelastic feature with the emission energy (see Figure 4) of ~507.2 eV and ~508 eV, respectively. When excitation energies move to *c* (= 523.1 eV) and *d* (=524.6 eV) at $2p_{1/2}$ absorption edge, RIXS spectra show prominent double inelastic features. Inelastic peaks: (I) at the lower emission energy (see Figure 4), are between 506 and 512 eV in both spectra, and with a ~0.2 eV maximum difference; (II) at the lower energy transfer (see Figure 5), are with energy transfer maximum of ~6.3 eV and ~7.5 eV in spectra *c* and *d*, respectively.

In all four RIXS spectra acquired, inelastic features with energy transfer ~6.3 eV and ~7.5 eV correspond to the nonbonding $3d^1\underline{L}$ configuration, due to different symmetry between the 3d state and the ligand hole ($\underline{L}$). The 3d states with the $e_g$ symmetry are selectively excited to intermediate states with energies *a* and *c*, and similarly the $t_{2g}$ symmetry with energies *b* and *d*. The 3d states in the nonbonding $3d^1\underline{L}$ final state keep the corresponding symmetries, and from which the ~1.2 eV difference between $e_g$ and $t_{2g}$ symmetries is obtained, indicating a 10Dq value of approximate 1.2 eV for the vanadium centers in $\mathbf{Co_4V_2}$. Note that the obtained 10Dq value and the energy difference (2.3 eV) between peaks *a* and *b* at $2p_{3/2}$ absorption edge match the rule revealed by de Groot *et al*.[46] The nonbonding peaks in RIXS spectra *c* and *d* are drastically enhanced w.r.t the elastic peak intensity, when comparing to their counterparts in spectra *a* and *b*. One relaxation mechanism that explained the similar enhancements found in titanium (4+, $3d^0$) RIXS spectra of $TiCl_4$ was discussed by Hague *et al*.[60] With energies *c* and *d*, the $2p_{1/2}$ core-level is resonantly excited, and the subsequent Coster-Kronig transition yields the $3d^1c\underline{L}$ and $3d^0c$ (c represents an electron in the continuum) configurations. The radiative decay can happen between these two configuration, and the emission energy of which may coincide with energy of nonbonding features. Therefore, the presence of such extra decay channel explains the intensity enhancement of corresponding nonbonding peaks.

The shoulders on the lower energy side of inelastic features in spectra *a* and *b*, as well as the lower energy inelastic peaks in both spectra *c* and *d*, correspond to the antibonding state. In Figure 4, it can be seen that all transitions to the antibonding state remain almost at the fixed emission energy. This is because the antibonding state has a broad band-like structure, and decay from antibonding state in the intermediate state to the antibonding state in the final state keeps the same symmetry and the small varied energies, making the antibonding feature like a fluorescence peak with the constant emission energy.

Apart from inelastic peaks corresponding to nonbonding and antibonding states, two other inelastic features are also observed respectively in RIXS spectra *b* and *c*, with energy transfer 4.2 eV and 1.5 eV (see Figure 5). The 1.5 eV inelastic feature, which is conspicuous in the spectrum *c*, also appears in the spectrum *d* (see the inset in Figure 5), notwithstanding the lower intensity. The fact that 2p3d RIXS efficaciously probes d-d excitations and 1.5 eV represents a typical ligand field strength of transition metal ions, reasonably suggests this feature to be the d-d excitation of vanadium 4+ ions, as photoreduction on vanadium 5+ ions was unavoidably induced by X-ray beams. A fast scan mode was used (see the Experimental Section) during RIXS acquisitions to minimize the photoreduction effects, even though, the beam induced modifications on the sample are hard to be fully excluded without further experimental proofs. Importantly, current spectral features should, to a large extent, promise the dominant species of vanadium revealed by RIXS to be vanadium 5+ ions. One may ask why the d-d excitation is only visible in the spectrum *c* and much less visible in the spectrum *d*, and in spectra *a* and *b*, however, corresponding positions are almost featureless. When comparing the shapes of XAS spectra in Figure S3, one can find that the XAS cross section ratio between vanadium 4+ and 5+ at excitation energy *c* should be the highest among those at energies *a*-*d*. At the energy *d*, this ratio decreases; while the vanadium 5+ resonances are much stronger at energies *a* and *b*. This explains the d-d feature from photo-reduced vanadium 4+ ions to be most visible at the RIXS spectrum *c*. Note that although photoreduction effects in RIXS spectra should be quite different from those shown in XAS spectra considering the different acquisition methods, the understanding of such effects in RIXS should be judicious through XAS results. In the left panel of Figure 6, a simplified single electron schematic representation of vanadium 4+ d-d excitation in 2p3d RIXS processes is shown. In Figure S9, we show a model LFM RIXS calculation result of vanadium 4+ ions, in which only the single d-d excitation feature can be observed. Note that the symmetry of vanadium 4+ ions in this calculation is assumed to be the tetrahedral, without considering the possible symmetry change during photoreduction processes.

Other than the 1.5 eV d-d excitation, another inelastic feature with 4.2 eV energy transfer is clearly seen in the spectrum *b*, but not in any of other three spectra. This inelastic feature can neither be a first d-d excitation because the 4.2 eV value largely exceeds the ligand field strength of any known transition metal ions, nor be the features represent charge transfer between oxygen ligand and vanadium metal centers, since if so, it should be observed the same as other counterparts in all four RIXS spectra. The only logical source of this feature, therefore, becomes the metal to metal charge transfer between cobalt ions and vanadium ions in **$Co_4V_2$**. The metal to metal charge transfer, or named as intersite d-d charge transfer, has been demonstrated in manganese RIXS spectra of manganite,[61] and in titanium RIXS spectra of a series of $MTiO_3$,[26-27] where M is the manganese, iron, cobalt and nickel. In **$Co_4V_2$**, each vanadium tetrahedra shares one oxygen corner with three

cobalt ions in the tetra-cobalt core. The 3d orbitals of cobalt and vanadium can then overlap via the mediation of hybridized oxygen 2p orbital, which proceeds by the charge transfer between cobalt and vanadium ions. The right panel of Figure 6 shows schematically the energy diagram of lowest bases of the vanadium initial state, where the state corresponding to the cobalt 3d and vanadium 3d charge transfer ($d^6d^1$) locates between the bonding and nonbonding states. The spectral intensity of this state, comparing with those of nonbonding or/and antibonding states, is much weaker that should relate to the indirect nature of the cobalt-vanadium charge transfer path via the mediator oxygen, while the charge transfer path between ligand oxygen and vanadium is direct. When exciting at the energy *b*, the large absorption cross section give rise to the enhancement of the total RIXS cross section, which allows the direct observation on the 3d orbital admixture between cobalt and vanadium centers. At other three excitation energies (*a*, *c* and *d*), however, other stronger transition channels overwhelm more, obscuring the trace of the weak cobalt-vanadium charge transfer channel to be visible in RIXS spectra.

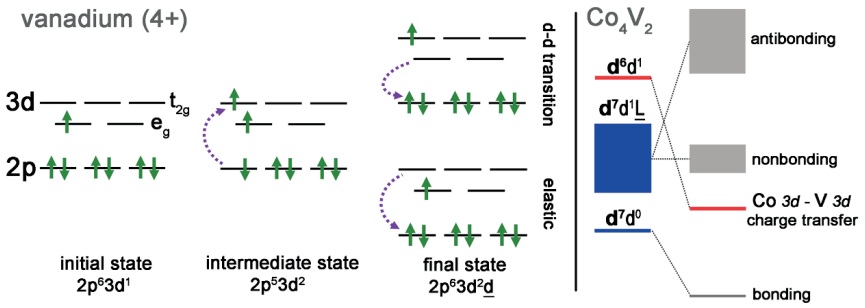


**Figure 6.** Left panel: a simplified single electron schematic representation of 2p3d RIXS processes for the vanadium 4+ ion. Right panel: the energy diagram of lowest bases for the vanadium initial state of **$Co_4V_2$**. The bold $d^n$ and narrow $d^m$ or $d^m\underline{L}$ indicate the cobalt and vanadium configurations, respectively.

The spectroscopic evidence of the cobalt-vanadium charge transfer in **$Co_4V_2$**, revealed by vanadium 2p3d RIXS spectra, experimentally proves the previous DFT calculated orbital mixture between $VO_4$ and $Co_4O_x$.[6] Consistently, the smaller ligand field strength of the tetra-cobalt core in **$Co_4V_2$** than that in **$Co_4P_2$**, revealed by cobalt 2p3d RIXS spectra, indicates effectively the smaller electron delocalization on the cobalt core of **$Co_4V_2$**. The intervalence charge transfer could lead to the change of cobalt ($3d^7$), vanadium ($3d^0$) to the cobalt ($3d^6$) and the vanadium ($3d^1$), and *vice versa*.

## 2.5. CONCLUSION

We use element-specific 2p XAS and 2p3d RIXS spectra to separately investigate the 3d transition metal sites in **$Co_4P_2$** and **$Co_4V_2$** POM WOCs. Differences of the cobalt 3d electronic structures of each tetra-cobalt core are revealed by both XAS and RIXS. Cobalt experimental spectra are simulated via the LFM approach and by which the ligand field influenced 3d electronic states are understood. High energy resolution 2p3d RIXS results unveil the small deviations of the ligand field strength for two isostructural cobalt cores. From the vanadium 2p XAS and 2p3d RIXS spectra, the oxidation states and ligand field strengths of iso-vanadium centers are obtained. RIXS results effectively show the bound electronic states of vanadium with oxygen ligands and cobalt heteroatoms. The spectral evidence of vanadium and cobalt 3d orbital hybridization in **$Co_4V_2$** supports the previous theoretical predictions. Such charge transfer between transition metal centers favors the **$Co_4V_2$** with unique properties for redox chemistry, like the water oxidation processes. While in **$Co_4P_2$**, no analogous orbitals, or the charge transition channels, assist redox properties of the tetra-cobalt core. However, we note that the different ground electronic structure of **$Co_4P_2$** and **$Co_4V_2$**, obtained here, are expected to be modified during catalytic reactions. The trace of charge transfer between cobalt and vanadium in **$Co_4V_2$** adds the useful insight to understand the potential electron transfer routes related catalytic properties, whereas a complete *in-situ* investigation on electronic structures of **$Co_4V_2$** are definitely further needed to unveil its mysteriousness.


## ACKNOWLEDGEMENT

This work is financially supported by the China Scholarship Council (CSC) and the ERC advanced grant XRAYonACTIVE, number 340279. We thank the onsite assistances from beamline staffs in ANKA, NSRRC and SPring-8. The sample are offered by Elliot N. Glass and Craig L. Hill from Emory University in USA. Ru-pan Wang and Frank de Groot in Utrecht University are appreciated for data analysis.


**This chapter is special for me since I wish to use it as a memory of my dearest grandma. When I was acquiring the cobalt RIXS spectra in Taiwan, she passed away suddenly on Friday, May 27$^{th}$, 2017, in Ya-an, Sichuan, P.R. China. This terrible shock came to me a few days later when I came back to Netherlands, and I missed the last chance to see her. The grievousness in my heart is impossible to be expressed by any words, but which lasts forever. My grandma stays with me forever, and I believe that every progress and happiness of mine will be brought to her in the Heaven.**

## Supporting Information available in Appendix 2

## REFERENCES


(1) de Smit, E.; Weckhuysen, B. M. *Chem. Soc. Rev*. **2008**, *37*, 2758-2781.

(2) Calderone, V. R.; Shiju, N. R.; Ferre, D. C.; Rothenberg, G. *Green Chem*. **2011**, *13*, 1950-1959.

(3) Calderone, V. R.; Shiju, N. R.; Curulla-Ferre, D.; Chambrey, S.; Khodakov, A.; Rose, A.; Thiessen, J.; Jess, A.; Rothenberg, G. *Angew. Chem., Int. Ed*. **2013**, *52*, 4397-4401.

(4) Eschemann, T. O.; Lamme, W. S.; Manchester, R. L.; Parmentier, T. E.; Cognigni, A.; Ronning, M.; de Jong, K. P. *J. Catal.* **2015**, *328*, 130-138.

(5) Yin, Q. S.; Tan, J. M.; Besson, C.; Geletii, Y. V.; Musaev, D. G.; Kuznetsov, A. E.; Luo, Z.; Hardcastle, K. I.; Hill, C. L. *Science* **2010**, *328*, 342-345.

(6) Lv, H. J.; Song, J.; Geletii, Y. V.; Vickers, J. W.; Sumliner, J. M.; Musaev, D. G.; Kogerler, P.; Zhuk, P. F.; Bacsa, J.; Zhu, G. B.; Hill, C. L. *J. Am. Chem. Soc.* **2014**, *136*, 9268-9271.

(7) Nilsson, A.; Pettersson, L. G. M.; Hammer, B.; Bligaard, T.; Christensen, C. H.; Norskov, J. K. *Catal. Lett.* **2005**, *100*, 111-114.

(8) Chow, J.; Kopp, R. J.; Portney, P. R. *Science* **2003**, *302*, 1528-1531.

(9) Lewis, N. S.; Nocera, D. G. *Proc. Natl. Acad. Sci.* U. S. A. **2006**, *103*, 15729-15735.

(10) Gray, H. B. *Nat. Chem*. **2009**, *1*, 7-7.

(11) Geletii, Y. V.; Botar, B.; Koegerler, P.; Hillesheim, D. A.; Musaev, D. G.; Hill, C. L. *Angew. Chem., Int. Ed*. **2008**, *47*, 3896-3899.

(12) Geletii, Y. V.; Huang, Z. Q.; Hou, Y.; Musaev, D. G.; Lian, T. Q.; Hill, C. L. *J. Am. Chem. Soc.* **2009**, *131*, 7522-7523.

(13) Huang, Z. Q.; Luo, Z.; Geletii, Y. V.; Vickers, J. W.; Yin, Q. S.; Wu, D.; Hou, Y.; Ding, Y.; Song, J.; Musaev, D. G.; Hill, C. L.; Lian, T. Q. *J. Am. Chem. Soc.* **2011**, *133*, 2068-2071.

(14) Toma, F. M.; Sartorel, A.; Iurlo, M.; Carraro, M.; Parisse, P.; Maccato, C.; Rapino, S.; Gonzalez, B. R.; Amenitsch, H.; Da Ros, T.; Casalis, L.; Goldoni, A.; Marcaccio, M.; Scorrano, G.; Scoles, G.; Paolucci, F.; Prato, M.; Bonchio, M. *Nat. Chem.* **2010**, *2*, 826-831.

(15) Murakami, M.; Hong, D. C.; Suenobu, T.; Yamaguchi, S.; Ogura, T.; Fukuzumi, S. *J. Am. Chem. Soc.* **2011**, *133*, 11605-11613.

(16) Car, P. E.; Guttentag, M.; Baldridge, K. K.; Alberto, R.; Patzke, G. R. *Green Chem.* **2012**, *14*, 1680-1688.

(17) Zhu, G. B.; Glass, E. N.; Zhao, C. C.; Lv, H. J.; Vickers, J. W.; Geletii, Y. V.; Musaev, D. G.; Song, J.; Hill, C. L. *Dalton Trans.* **2012**, *41*, 13043-13049.

(18) Vickers, J. W.; Lv, H. J.; Sumliner, J. M.; Zhu, G. B.; Luo, Z.; Musaev, D. G.; Geletii, Y. V.; Hill, C. L. *J. Am. Chem. Soc.* **2013**, *135*, 14110-14118.

(19) Schiwon, R.; Klingan, K.; Dau, H.; Limberg, C. *Chem. Commun.* **2014**, *50*, 100-102.

(20) Kotani, A.; Shin, S. *Rev. Mod. Phys.* **2001**, *73*, 203-246.

(21) de Groot, F.M.F.; Kotani, A. *Core Level Spectroscopy of Soli*ds; CRC Press: Boca Raton, FL, 2008.

(22) Ament, L. J. P.; van Veenendaal, M.; Devereaux, T. P.; Hill, J. P.; van den Brink, J. *Rev. Mod. Phys.* **2011**, *83*, 705-767.

(23) van Schooneveld, M. M.; Gosselink, R. W.; Eggenhuisen, T. M.; Al Samarai, M.; Monney, C.; Zhou, K. J. J.; Schmitt, T.; de Groot, F. M. F. *Angew. Chem., Int. Ed*. **2013**, *52*, 1170-1174.

(24) Liu, B. Y.; Wang, R. P.; Glass, E. N.; Hill, C. L.; Cuk, T.; Okamoto, J.; Huang, D. J.; van Schooneveld, M. M.; de Groot, F. M. F. *Inorg. Chem.* **201**6, *55*, 10152-10160.

(25) van Veenendaal, M. A.; Sawatzky, G. A. *Phys. Rev. Lett.* **1993**, *70*, 2459-2462.

(26) Agui, A.; Uozumi, T.; Mizumaki, M.; Kaambre, T. *Phys. Rev. B* **2009**, *79*, 092402.

(27) Agui, A.; Mizumaki, M.; Uozumi, T. *J. Electron Spectrosc. Relat. Phenom.* **2015**, *205*, 106-110.

(28) Glass, E. N.; Fielden, J.; Kaledin, A. L.; Musaev, D. G.; Lian, T. Q.; Hill, C. L. *Chem.-Eur. J.* **2014**, *20*, 4297-4307.

(29) Stavitski, E.; de Groot, F. M. F. *Micron* **2010**, *41*, 687-694.

(30) Haverkort, M. W.; Zwierzycki, M.; Andersen, O. K. *Phys. Rev. B* **2012**, *85*, 165113.

(31) Hariki, A.; Yamanaka, A.; Uozumi, T. *J. Phys. Soc. Jpn.* **2015**, *84*, 073706.

(32) Maganas, D.; Roemelt, M.; Havecker, M.; Trunschke, A.; Knop-Gericke, A.; Schlogl, R.; Neese, F. *Phys. Chem. Chem. Phys.* **2013**, *15*, 7260-7276.

(33) Lundberg, M.; Kroll, T.; DeBeer, S.; Bergmann, U.; Wilson, S. A.; Glatzel, P.; Nordlund, D.; Hedman, B.; Hodgson, K. O.; Solomon, E. I. *J. Am. Chem. Soc.* **2013**, *135*, 17121-17134.

(34) Suljoti, E.; Garcia-Diez, R.; Bokarev, S. I.; Lange, K. M.; Schoch, R.; Dierker, B.; Dantz, M.; Yamamoto, K.; Engel, N.; Atak, K.; Kuhn, O.; Bauer, M.; Rubensson, J. E.; Aziz, E. F. *Angew. Chem., Int. Ed*. **2013**, *52*, 9841-9844.

(35) Pinjari, R. V.; Delcey, M. G.; Guo, M. Y.; Odelius, M.; Lundberg, M. *J. Chem. Phys.* **2014**, *141*, 124116.

(36) Haverkort, M. W.; Sangiovanni, G.; Hansmann, P.; Toschi, A.; Lu, Y.; Macke, S. *EPL* **2014**, *108*, 57004.

(37) Garvie, L. A. J.; Craven, A. *J. Phys. Chem. Miner.* **1994**, *21*, 191-206.

(38) Brydson, R.; Garvie, L. A. J.; Craven, A. J.; Sauer, H.; Hofer, F.; Cressey, G. *J. Phys.-Condes. Matter* **1993**, *5*, 9379-9392.

(39) van Schooneveld, M. M.; DeBeer, S. *J. Electron Spectrosc. Relat. Phenom.* **2015**, *198*, 31-56.

(40) Lai, C. H.; Fung, H. S.; Wu, W. B.; Huang, H. Y.; Fu, H. W.; Lin, S. W.; Huang, S. W.; Chiu, C. C.; Wang, D. J.; Huang, L. J.; Tseng, T. C.; Chung, S. C.; Chen, C. T.; Huang, D. J. *J. Synchrot. Radiat.* **2014**, *21*, 325-332.

(41) Harada, Y.; Kobayashi, M.; Niwa, H.; Senba, Y.; Ohashi, H.; Tokushima, T.; Horikawa, Y.; Shin, S.; Oshima, M. *Rev. Sci. Instrum.* **2012**, *83*, 013116.

(42) Yamamoto, S.; Senba, Y.; Tanaka, T.; Ohashi, H.; Hirono, T.; Kimura, H.; Fujisawa, M.; Miyawaki, J.; Harasawa, A.; Seike, T.; Takahashi, S.; Nariyama, N.; Matsushita, T.; Takeuchi, M.; Ohata, T.; Furukawa, Y.; Takeshita, K.; Goto, S.; Harada, Y.; Shin, S.; Kitamura, H.; Kakizaki, A.; Oshima, M.; Matsuda, I. *J. Synchrot. Radiat.* **2014**, *21*, 352-365.

(43) Cowan, R. D. *J. Opt. Soc. Am.* **1968**, 58 (6), 808-818.

(44) Cowan, R. D. *The Theory of Atomic Structure and Spectra*; University of California Press: Berkeley, CA 1981.

(45) Thole, B. T.; van der Laan, G.; Butler, P. H. *Chem. Phys. Lett.* **1988**, *149*, 295-299.

(46) de Groot, F. M. F.; Fuggle, J. C.; Thole, B. T.; Sawatzky, G. A. *Phys. Rev. B* **1990**, *41*, 928-937.

(47) Kramers, H. A.; Heisenberg, W. *Z. Phys.* **1925**, *1*, 681-701

(48) de Groot, F. M. F.; Arrio, M. A.; Sainctavit, P.; Cartier, C.; Chen, C. T. *Solid State Commun.* **1994**, *92*, 991-995.

(49) Kurian, R.; Kunnus, K.; Wernet, P.; Butorin, S. M.; Glatzel, P.; de Groot, F. M. F. *J. Phys. Condens. Matter* **2012**, *24*, 452201.

(50) Magnuson, M.; Butorin, S. M.; Guo, J. H.; Nordgren, *Phys. Rev. B* **2002**, *65*, 205106.

(51) van Schooneveld, M. M.; Kurian, R.; Juhin, A.; Zhou, K. J.; Schlappa, J.; Strocov, V. N.; Schmitt, T.; de Groot, F. M. F. *J. Phys. Chem. C* **2012**, *116*, 15218-15230.

(52) Waegele, M. M.; Doan, H. Q.; Cuk, T. *J. Phys. Chem. C* **2014**, *118*, 3426-3432.

(53) Schmidtke, H.-H. *The Variation of Slater-Condon Parameters $F^k$ and Racah Parameters B and C with Chemical Bonding in Transition Group Complexes. in Optical Spectra and Chemical Bonding in Inorganic Compounds: Special Volume dedicated to Professor Jørgensen I*; Springer Berlin Heidelberg: Berlin, Heidelberg, 2004.

(54) Hunault, M.; Harada, Y.; Miyawaki, J.; Wang, J.; Meijerink, A.; de Groot, F.M.F.; van Schooneveld, M. M. Unpublished results.

(55) de Groot, F. M. F. *Coord. Chem. Rev.* **2005**, *249*, 31-63.

(56) Butorin, S. M.; Guo, J. H.; Magnuson, M.; Nordgren, J. *Phys. Rev. B* **1997**, *55*, 4242-4249.

(57) Wen, A. T.; Hitchcock, A. P. *Can. J. Chem.* **1993**, *71*, 1632-1644.

(58) Hoche, T.; Ikeno, H.; Mader, M.; Henderson, G. S.; Blyth, R. I. R.; Sales, B. C.; Tanaka, I. *Am. Miner.* **2013**, *98*, 665-670.

(59) Collison, D.; Garner, C. D.; Grigg, J.; McGrath, C. M.; Mosselmans, J. F. W.; Pidcock, E.; Roper, M. D.; Seddon, J. M. W.; Sinn, E.; Tasker, P. A.; Thornton, G.; Walsh, J. F.; Young, N. A. *J. Chem. Soc., Dalton Trans.* **1998**, 2199-2204.

(60) Hague, C. F.; Tronc, M.; Yanagida, Y.; Kotani, A. *Phys. Rev. A* **2001**, *63*, 012511.

(61) Grenier, S.; Hill, J. P.; Kiryukhin, V.; Ku, W.; Kim, Y. J.; Thomas, K. J.; Cheong, S. W.; Tokura, Y.; Tomioka, Y.; Casa, D.; Gog, T. *Phys. Rev. Lett.* **2005**, *94*, 047203.

# Appendix 2

UV/vis and FT-IR data of **$Co_4P_2$** and **$Co_4V_2$**.

Comparisons of vanadium 2p XAS acquired in ANKA and SPring-8.

X-ray crystal structures of **$Co_4P_2$** and **$Co_4V_2$** in ball-and stick representations.

Experimental cobalt 2p XAS of **$Co_4P_2$** and **$Co_4V_2$** acquired in ANKA with TEY (at room temperature) and TFY (at 50K) mode respectively.

Experimental cobalt 2p XAS and 2p3d RIXS spectra of **$Co_4P_4$**, **$Co_4P_2$** and **$Co_4V_2$**.

LFM simulated cobalt 2p3d RIXS planes of **$Co_4V_2$** and **$Co_4P_2$**.

LFM simulated 2p3d RIXS plane of the vanadium 4+ ion.

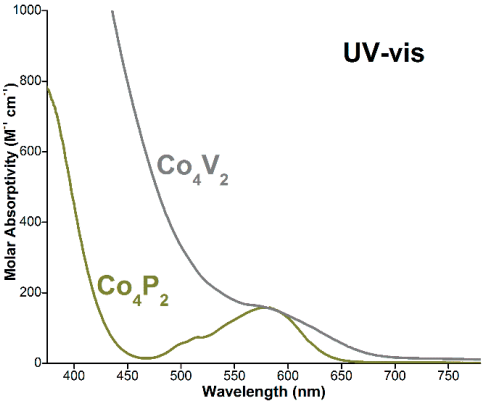


**Figure S1.** UV-vis spectra of $Co_4P_2$ (dark yellow) and $Co_4V_2$ (gray) acquired of ~1 mM aqueous solutions.

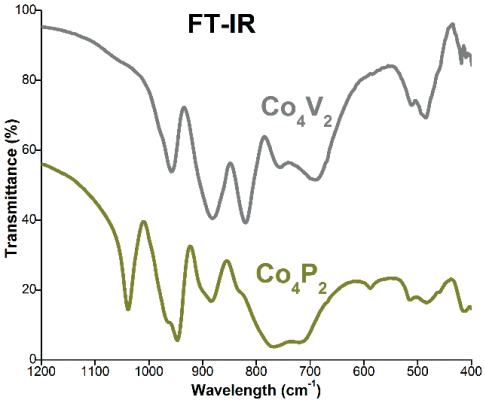


**Figure S2.** FT-IR spectra of $Co_4P_2$ (dark yellow) and $Co_4V_2$ (gray), 2 wt % in KBr.

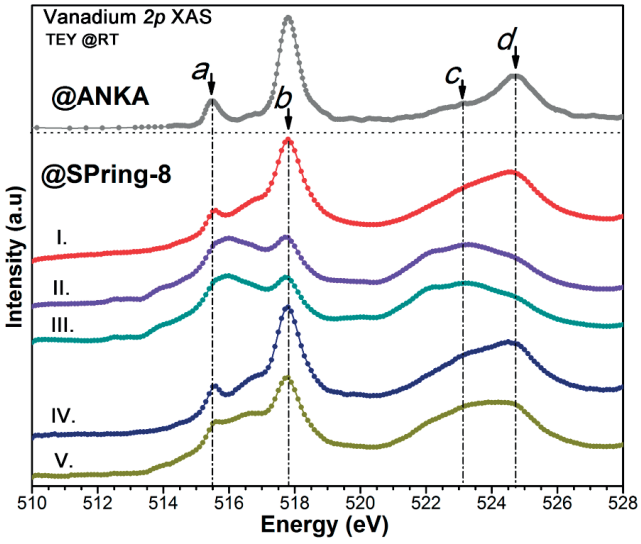


**Figure S3.** Vanadium experimental 2p XAS: (upper panel) data acquired in ANKA synchrotron; (lower panel) data acquired in SPring-8 synchrotron. Arrow *a-d* indicate the exaction energies of 2p3d RIXS. The spectra I-V acquired in SPring-8 were measured at: (I). a new pristine position; (II) the same position as I; (III) the same position as I and II; (IV). a new pristine position; (V) the same position as IV on the pressed sample pellet.

In Figure S3, the vanadium 2p XAS acquired in ANKA (upper panel) and in SPring-8 (lower panel) are compared. The spectra from SPring-8 shows the beam induced photoreduction of vanadium 5+ ions. The two spectra (I and IV) that were measured at a pristine new sample position shows higher intensity of the peak *c*. For spectra II, III that are acquired with the same sample position as spectrum I, and for the spectrum V that is acquired with the same sample position as spectrum IV, the intensity of peak c enhances even higher. The change of the intensity indicates the photoreduction of vanadium 5+ to 4+, similar as found in literatures.[59] Besides, the 1.5 eV difference of peak *c* and *d* is approximately the $L_2$ edge maxima between vanadium 4+ and 5+, suggesting that the RIXS spectrum acquired with excitation energy *c*, if the photoreduction effect is unavoidable within the fast scan mode of RIXS measurement, shows the most prominent vanadium 4+ RIXS d-d features.

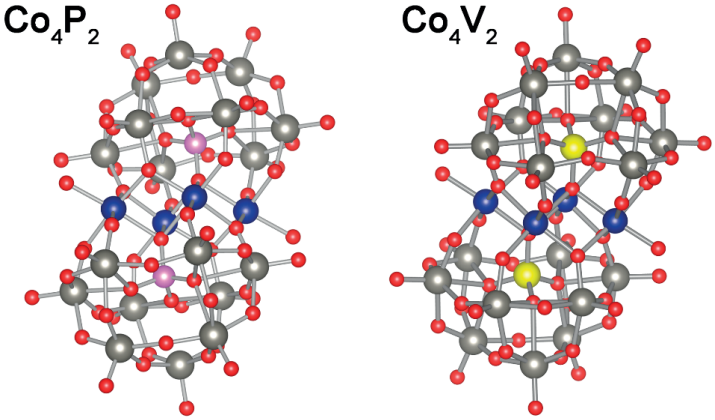


**Figure S4.** X-ray crystal structures of **$Co_4P_2$** (left) and **$Co_4V_2$** (right) in ball-and stick representations. Red: oxygen; blue: cobalt; purple: phosphorous; yellow: vanadium; gray: tungsten.

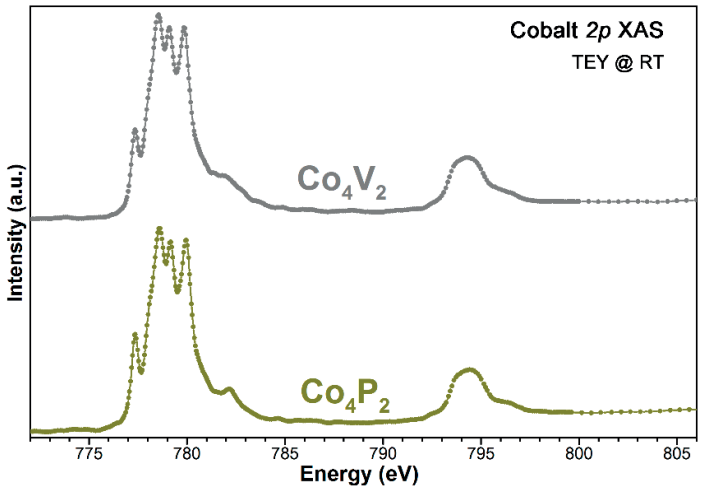


**Figure S5.** Experimental cobalt 2p XAS spectra of **$Co_4P_2$** (lower, dark yellow) and **$Co_4V_2$** (upper, gray) acquired in ANKA synchrotron, with TEY mode at the room temperature.

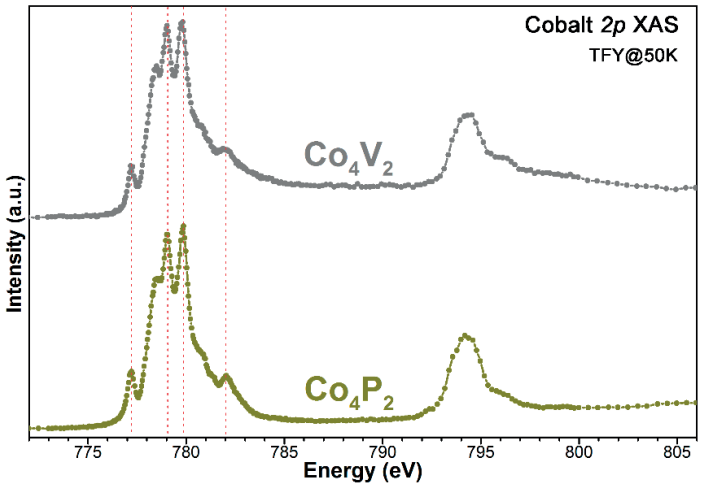


**Figure S6.** Experimental cobalt 2p XAS spectra of **$Co_4P_2$** (lower, dark yellow) and **$Co_4V_2$** (upper, gray) acquired in ANKA synchrotron, with TFY mode at the temperature of 50 K.

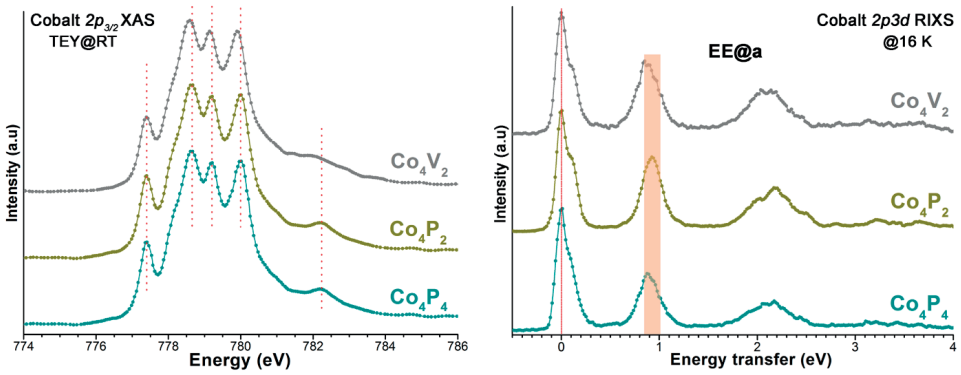


**Figure S7.** Experimental cobalt $2p_{3/2}$ TEY XAS (left panel) and 2p3d RIXS (right panel) spectra of **$Co_4P_4$** (bottom, green), **$Co_4P_2$** (middle, dark yellow) and **$Co_4V_2$** (top, gray). The **$Co_4P_4$** is short for the POM $Na_{16}[Co_4(H_2O)_2(P_2W_{15}O_{56})_2]\cdot xH_2O$,[5] which has the isostructural tetra-cobalt core as **$Co_4P_2$** and **$Co_4V_2$**. All XAS spectra were acquired in ANKA synchrotron and RIXS spectra were acquired in SPring-8 synchrotron. RIXS spectra were acquired with the excitation energy *a*, which was indicated in the Figure 2.

In $2p_{3/2}$ XAS of **$Co_4P_2$** and **$Co_4P_4$**, the red-dotted lines indicate the same positions of all prominent multiplet peaks, and from which the same LFM parameters may use for the spectra simulation. Whereas in 2p3d RIXS, the first d-d excitation peak of **$Co_4P_2$** and **$Co_4P_4$** shows the observable deviations that indicate a smaller (effective) ligand field strength of the tetra-cobalt core in **$Co_4P_4$**. This example implies that differences shown in the $2p_{3/2}$ XAS of **$Co_4P_2$** and **$Co_4V_2$** may not be enough to demonstrate detailed ligand field information, while 2p3d RIXS results are more sensitive to show the information with higher accuracy. Fortunately, for **$Co_4P_2$** and **$Co_4V_2$**, 2p XAS and 2p3d RIXS results can be interpreted with a unique set of LFM parameters (in Table 1), suggesting the effectiveness of the LFM parameters found.

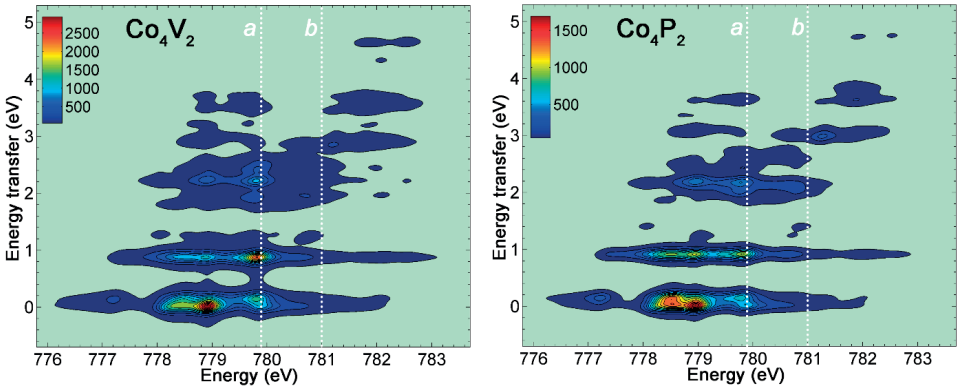


**Figure S8.** LFM simulated cobalt 2p3d RIXS planes of $Co_4V_2$ (left) and $Co_4P_2$ (right). The white dotted lines *a* and *b* in both RIXS planes correspond to the excitation energies *a* and *b* as indicated in Figure 2.

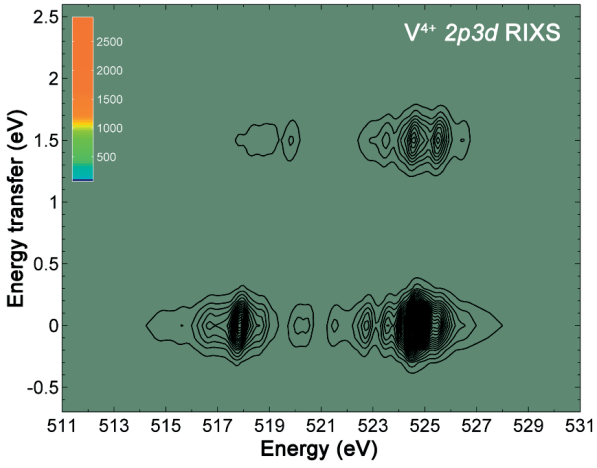


**Figure S9.** LFM simulated 2p3d RIXS plane of the vanadium 4+ ion, with the ligand field strength 10Dq of -1.5 eV.

Chapter 3.

# Distorted tetrahedral $Co^{II}$ in $K_5H[CoW_{12}O_{40}]\cdot xH_2O$ probed by 2p3d resonant inelastic X-ray scattering

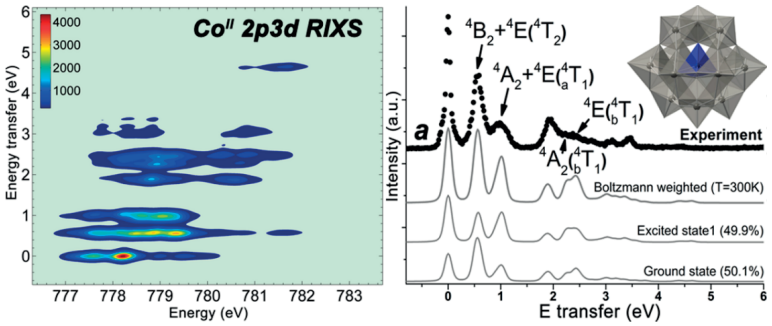


The Co $2p_{3/2}$ X-ray absorption (XAS) and the high energy resolution (~0.09 eV FWHM) 2p3d resonant inelastic X-ray scattering (RIXS) spectra of the single cobalt centered polyoxometalate $K_5H[CoW_{12}O_{40}]\cdot xH_2O$ were measured. The low energy dd transition features at 0.55 eV, unmeasurable with ultraviolet-visible (UV/vis) spectroscopy, were experimentally revealed in 2p3d RIXS spectra. RIXS simulations based on ligand field multiplet theory were performed to assess the potential cobalt tetragonal symmetry distortion, which is described with the ligand field parameters10Dq (-0.54 eV), Ds (-0.08 eV) and Dt (0.005 eV). As 2p3d RIXS probes not only the optical spin allowed but also the spin forbidden transitions, we show that the current 2p3d RIXS simulation enables a series of dd feature assignments with higher accuracy than those from previous optical data. Furthermore, by wavefunction decomposition analyses, we demonstrate the more realistic and detailed origins of a few lowest dd transitions using both one electron orbital and term symbol descriptions.

## 3.1. INTRODUCTION

Cobalt containing materials, in which the cobalt possesses a partially filled 3d shell, exhibit unique electronic and magnetic properties for a wide range of applications. The oxide ($\alpha$-$Al_2O_3$, $SiO_2$, $TiO_2$, etc.) supported or carbon supported cobalt Fischer-Tropsch catalysts are, for example, industrially optimal for the synthesis of long-chain hydrocarbons and clean fuels,[1] while cobalt doped $TiO_2$ is of interest for spintronic devices owing to its room temperature ferromagnetism.[2] More recently, a series of Co-containing polyoxometalates (POMs) have been developed as fast water oxidation catalysts (WOCs)[3-5] to harness the solar energy via artificial photosynthesis. Among the numerous POMs that have been reported as WOCs, POMs containing tetra-cobalt cores, such as $[Co_4(H_2O)_2(PW_9O_{34})_2]^{10-}$ and $[Co_4(H_2O)_2(VW_9O_{34})_2]^{10-}$, are particularly active.[6] Since Co-oxo cores in POMs are suspected to be the active catalytic center,[3] probing the Co electronic structure attracts great interest as to understand catalytic behaviors. Single cobalt centered POMs are to date found to be catalytic inactive for water oxidation, but the structural similarity of the Co-oxo core to those of active POMs make them important model systems to elaborate on the electronic structure of this class of compounds. To this end various spectroscopic techniques have been applied, including optical absorption and XAS.[7-11] Owing to the superior discriminative power of 2p3d RIXS,[12] here we probe the electronic structure of 3d-rich cobalt in a single Co centered POM $K_5H[CoW_{12}O_{40}]\cdot xH_2O$ (originally $K_5H[CoW_{12}O_{40}]\cdot 12H_2O$, *vide infra*), with an energy resolution better than 100 meV. A large number of dd excitations, including optical forbidden transitions, were probed. Ligand field multiplet [13] spectral simulations clearly reveal the presence of $Co^{II}$ ($3d^7$, high spin) ions in a small tetragonal $D_{2d}$ distorted tetrahedral ($T_d$) field.

To understand the improvement this work made on the accurate probing and description of the Co electronic structure, previous results on $\alpha$-Keggin $[CoW_{12}O_{40}]^{6-}$ anions are here briefly reviewed with a focus on comparisons to spectroscopic studies. UV/vis absorption and 2p ($L_{2,3}$ edge, 2p to 3d) XAS spectra are mostly used as probes for the 3d-rich electronic structure of cobalt (see Ref. 12 for a RIXS-XAS-UV/vis comparison of cobalt carboxylates). In UV/vis, dd transitions excited by UV and visible light are used to probe 3d excited states. Commonly, excitations below 1.0 eV (~1240 nm) are not measured. The lack of low energy dd transitions can be found in UV/vis analyses of $K_2[(C_4H_9)_4N]_4[CoW_{12}O_{40}]\cdot CH_3CN$,[7] and $K_5H[CoW_{12}O_{40}]\cdot 12H_2O$,[9] the compound measured in the current work. While some advanced spectrometers allow wider range (longer wavelength range) detections, low-energy excitations are often masked by vibrational bands of the material. This limitation is seen in the low-energy optical absorption studies on $K_6[CoW_{12}O_{40}]\cdot mH_2O$,[8] in which the expected $^4A_2$ to $^4T_2$ ($^4F$) transition at 4600 $cm^{-1}$ (~0.57 eV) was not observed due to shadowing by water vibrational bands in the same energy region.

Nevertheless, this lowest transition in the $T_d$ $Co^{II}$ system is important as it effectively reveals the ligand field parameter 10Dq.[12] Also, since these dd transitions are the lowest energy electronic states and further, involve charge carriers localized to the metal center, catalysis is expected to proceed from them.[14] In above mentioned studies, this value could only be theoretically predicted without direct experimental demonstration. Additionally, strong metal to metal (Co to W) or metal to ligand (Co to O) charge transfer peaks on the high-energy side of UV/vis data, shade dd features, while in 2p3d RIXS, dd transitions can be more effectively demonstrated as they can be selectively excited.[15] Other than in UV/vis, in 2p XAS, the 3d empty states are indirectly probed as the final state is dominated by strong 2p3d interactions. Cobalt 2p XAS of $[CoW_{12}O_{40}]^{6-}$ was observed[11] to be featureless mainly due to the final state lifetime broadening, which obscured the accurate determination of electronic structure parameters (e.g. through multiplet analyses). Moreover, various parameter values in multiplet simulations could yield the same 2p XAS shape. This problem was also met in the current 2p XAS simulation, but with the aid of parameters obtained from 2p3d RIXS, the current experimental XAS was well interpreted. Details of differences in XAS interpretations are discussed. Importantly, both Co 2p XAS and 2p3d RIXS are element specific which constrains the probed electronic structure to the suspected catalytic center of the POM. Similar to advantages of 2p3d RIXS over UV/vis and 2p XAS as shown for the ligand field determination of cobalt carboxylates,[12] current RIXS analyses provide more previously unreached details of the Co electronic structure in $K_5H[CoW_{12}O_{40}]\cdot xH_2O$. Particularly, by analyzing low energy dd transition features, ligand field multiplet simulations enable a more effective discussion about the potential symmetry distortions of the Co center which is inaccessible by X-ray diffraction characterization and was only alluded or assumed based on the limited information from UV/vis spectra.[7, 16] Finally, the wavefunction decomposition analyses by using ligand field multiplet projection methods reveal the detailed origins of each dd transition.

## 3.2. EXPERIMENTAL SECTION

### 3.2.1. General Methods and Materials

$K_5H[Co^{II}W_{12}O_{40}]\bullet 12H_2O$ was prepared according to published procedures and ground to fine powders for analysis.[9, 17] The identity, purity, and waters of hydration were confirmed by Fourier transform infrared spectroscopy (FT-IR), UV-visible spectroscopy, and thermogravimetric analysis. Infrared spectra (2% by weight in KBr) were recorded on a Thermo Nicolet 6700 FT-IR spectrometer. UV-visible spectra were acquired using an Agilent 8453 spectrophotometer equipped with a diode-array detector and Agilent 89090A cell temperature controller unit. Thermogravimetric analysis was performed on a Perkin Elmer STA 6000 analyzer.

Characterizations by UV/vis and FT-IR are provided in Figures S1 and S2 of the Supporting Information.

### 3.2.2. Sample preparation for synchrotron XAS and RIXS measurements

The blue powdered $K_5H[CoW_{12}O_{40}]\cdot 12H_2O$ was pressed into a round pellet (8 mm ø; < 2 mm thick). FT-IR spectra prior and post pellet formation showed identical spectra, indicating the molecular structure to be unaffected by the process. The pellet was attached with conductive adhesive carbon tape onto an oxygen free copper holder. The holder was introduced into the load lock chamber, where the pressure was pumped down to $10^{-8}$ mbar before sample transfer to the main chamber for XAS/RIXS measurements. In vacuum, water molecules could potentially leave the $K_5H[CoW_{12}O_{40}]\cdot 12H_2O$ sample as they are often located in solvent accessible channels in the crystal structure, which facilitates their evaporation. The number of remaining water molecules largely depends on the ambient pressure, but FT-IR spectra of samples upon dehydration under different drying conditions remain identical (not shown). In our case, the number of water molecules left during measurements at $10^{-8}$ mbar was unclear, thus we prefer to name the sample as $K_5H[CoW_{12}O_{40}]\cdot xH_2O$ for XAS/RIXS measurements.

### 3.2.3. XAS and RIXS measurements

The Co $2p_{3/2}$ XAS was acquired in the total fluorescence yield (TFY) detection mode by using a photodiode located in the main chamber with a ~90° angle to the incident beam. The linear horizontal (LH, also called depolarized or linear parallel) polarized beam with a grazing incident angle of ~20° to the sample surface was used for both XAS and RIXS recording. Each XAS spectrum was sampled with 10 points $eV^{-1}$ ranging from 775 to 785 eV. Seven spectra were acquired at pristine sample positions each and averaged to present in this paper. The calibration of incident photon energy was done at the $2p_{3/2}$ ($L_3$) edge of a reference CoO single crystal and compared to literature values.[18] During XAS measurements, 50 μm exit slits were opened to optimize and also balance photon counts and the energy resolution (being ~0.5 eV full width at half maximum - FWHM).[19] The RIXS spectra were measured by the high energy spectrometer at beamline 05A1, National Synchrotron Radiation Research Center (NSRRC), Taiwan, where the optical system was designed based on the energy compensation principle of grating dispersion.[19, 20] For RIXS measurements, the active grating monochromator (AGM) and active grating spectrometer (AGS) need to be kept at the mirror condition, while the energy resolution of RIXS is determined by the width of the entrance slit without being influenced by the width of the exit slit. During current RIXS acquisition, the entrance slit was set to be ~7 μm and the exit slit was opened to 100 μm to increase photon flux, which led to a ~1.0 eV (FWHM) incoming x-ray window on

the sample. The out-going x-ray was focused by the AGS to the CCD detector. The scattering angle between vectors of incoming and outgoing beam was set to 90°. Measuring RIXS with LH polarization suppresses the cross section of the elastic peak with respect to non-resonant scattering features; and a grazing incident geometry minimizes the self-absorption of the elastic peak.[21, 22] By positioning the incident beam on the carbon tape and measuring elastic scattering peaks with incoming energies at 780 eV and 782 eV, the RIXS detector was calibrated. Two elastic peaks were fitted with Gaussian functions, and a linear relation between the fitted maxima was plotted against detector channels as an energy calibration. Around the Co $2p_{3/2}$ edge (~780 eV) of this POM sample, the RIXS energy resolution of the zero energy transfer peak was ~90 meV FWHM (for details see the Supporting Information.). The RIXS spectra were sampled with 56 points $eV^{-1}$ and at five different excitation energies. Presented RIXS spectra consist of the sum of 30-141 RIXS spectra (1 minute acquisition time each). During RIXS acquisition, a new, pristine position on the sample surface was exposed each 30 min, a timeframe in which no beam damage effects were observed in prior-post comparative XAS and RIXS measurements (prior-post comparative RIXS studies with 1 min acquisition time did also not reveal spectral changes). The pressure and temperature during all XAS/RIXS measurements were $< 2.0 \times 10^{-8}$ mbar and room temperature (~300 K), respectively.

## 3.3. THEORETICAL BASIS

### 3.3.1. Multiplet simulations

XAS and RIXS simulations were performed via the ligand field multiplet approach by using Cowan-Butler-Thole's code which was further modified and developed by Thole et al.[23-25] This code is implemented in free software interface suites: Charge Transfer Multiplets for XAS, RIXS and differential orbital covalency (CTM4XAS, CTM4RIXS and CTM4DOC).[26, 27] In the ligand field multiplet model, multiplets obtained under atomic symmetry were branched by using group theory to the $D_{2d}$ double group with the branching route following the $SO_3 > O_h > T_d > D_{2d}$ symmetry groups. This approach, by using atomic multiplets, ligand and superexchange fields to interpret the origin of 2p XAS and 2p3d RIXS transitions, has successfully simulated a large variety of 3d transition metal $L_{2,3}$ XAS and 2p3d RIXS.[12, 18, 28]

In the charge transfer multiplet model, the effects of charge fluctuations in initial and final states are taken into account by combining multiple configurations instead of using a single configuration in the atomic or ligand multiplet model. The simulated XAS by using this model showed satisfactory consistency to experimental results of those highly covalent sites.[29] The charge transfer effects associated with the covalency, however, were neglected in this simulation for ionic $Co^{II}$ sites, since each single $2p^63d^7$, $2p^53d^8$ and $2p^63d^8\underline{d}$ configuration is the dominant configuration in

respective states. Here the notation $3d^8\underline{d}$ is used to indicate the possible dd transitions (for the calculation the $2p^63d^7$ configuration is used). Moreover, in contrast to the X-ray photoemission spectroscopy (XPS), XAS and RIXS are neutral processes, which imply that only minor charge transfer effects need to be considered. The omission of charge transfer effects limits the number of semi-empirical parameters used for describing the electronic structures and it leads to the more precise determination of the ligand field parameters that are related to the symmetry of Co sites.

We note that the ligand field multiplet calculation is a semi-empirical approach to simulate the 2p XAS and 2p3d RIXS spectral shapes. This approach contains a number of approximations and empirical parameters. The main approximation is that the transition metal ion is described with a model where only the local 2p and 3d electrons are included. The 2p3d and 3d3d electron-electron interactions and the spin-orbit couplings are calculated from first principles for an ion. The crystal field splitting is used as empirical parameter, but in this case the value of 10Dq can be directly read from the first dd-excitation energy. In addition, small crystal site distortions can be explicitly considered. In our view it is important to use the ligand field multiplet model as it captures the essence of the 2p3d RIXS plane in a relatively simple model with a limited number of justifiable parameters.

It is however obvious that the semi-empirical ligand field multiplet model is not supposed to replace first-principle calculations. First principle calculations ultimately will correlate the molecular structure with the electronic structure and subsequently with the excited state properties such as 2p3d RIXS. It is noted that at this stage, first principle methods are not capable yet to describe the 2p3d RIXS spectra of open shell systems as accurate as semi-empirical codes. This is the case for both the solid-state based methods of Haverkort *et al.*,[30, 31] Hariki *et al.*[32, 33] and the quantum-chemistry based methods from the groups of Neese, [34, 35] Lundberg[36] and Odelius.[37] The first principle codes still have difficulties to accurately describe high-spin transition metal systems with the 90 meV resolution details as visible from 2p3d RIXS.

### 3.3.2. Ligand field multiplet XAS and RIXS simulations

A detailed description of the ligand field multiplet model is given in the Supporting Information,[13, 26, 38, 39] while Table 1 summarizes all the applied ligand field multiplet parameters used in current simulations.

### 3.3.3. Descriptions of the electronic states

The electronic states of transition metal systems are described with a number of approximate models,[26] which include:

i. the one-electron orbital model, e.g. with e and $t_2$ states in the $T_d$ symmetry, or analogous $a_1$, $b_1$, e and $b_2$ states in the $D_{2d}$ symmetry.
ii. the term symbol model, with term symbol notations in different symmetries. A state represented by a term symbol in lower symmetries (e.g. $D_{2d}$ or $D_{4h}$), can be decomposed into linear combinations of the atomic or the cubic symmetry term symbols.

States of the $3d^7$ initial state and equivalently the 2p3d RIXS final state $3d^8\underline{d}$, are described by term symbols in the $D_{2d}$ double group when including the 3d spin-orbit coupling, or described by a $D_{2d}$ ligand field term symbol without considering the 3d spin-orbit coupling effects. By using the projection method[29] implemented in CTM4DOC program, each state is expressed in atomic and cubic symmetry term symbols and one-electron orbital components. Detailed wavefunction expressions of the ground state and a few lowest excited states are presented in Table 2.

## 3.4. RESULTS AND DISCUSSION

### 3.4.1. Crystal structure

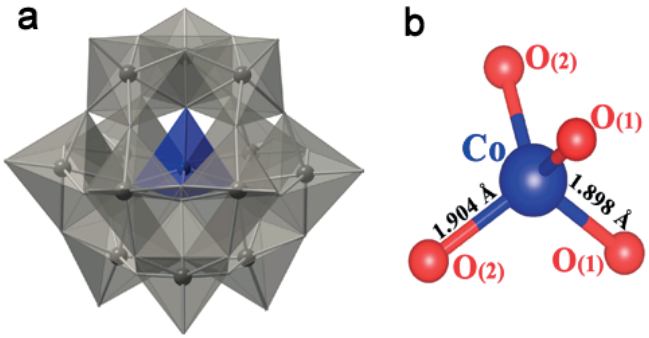


**Figure 1.** (a) X-ray crystal structure of the $[CoW_{12}O_{40}]^{6-}$ anions in polyhedral representation (the cobalt-oxo core in blue and tungstate octahedra in grey). (b) Ball-and-stick representation of the core cobalt ion coordinated with four oxygen ions. Experimental (crystallographic) bond lengths (Å): Co-$O_{(1)}$=1.898(12) and Co-$O_{(2)}$=1.904(12).

A polyhedral representation of the α-Keggin $[CoW_{12}O_{40}]^{6-}$ anion is shown in Figure 1a, obtained from a previously published crystal structure (ICSD 427379).[9] The $Co^{II}$ ion can be viewed as encapsulated by the $W_{12}O_{40}$ cage. Crystallographically determined four Co-O bond lengths are 1.898(12) Å and 1.904(12) Å, each length for two bonds as shown in Figure 1b as Co-$O_{(1)}$ and Co-$O_{(2)}$. Similar values can be found in literature,[9, 40] where all four bond lengths are reported as 1.900(12) or 1.895(12) Å, respectively. Note that bond lengths derived from X-ray crystallography

only reveal bonds of the crystalline sample, and the information obtained is limited by symmetry-derived crystallographic disorder.

### 3.4.2. XAS experiment and simulation

The experimental Co $2p_{3/2}$ XAS (TFY) of $K_5H[CoW_{12}O_{40}]\cdot xH_2O$ and the corresponding ligand field multiplet simulation are shown in Figure 2. The simulation was performed using parameters listed in Table 1. The ligand field parameter 10Dq was found to be -0.54 and -0.43 eV (a negative value is used in $T_d$ symmetry) for ground states and core hole excited states, respectively. The initial state 10Dq is obtained with high certainty (<5% error) from the RIXS data and the excited state value from the XAS data (see supporting Figure S3 and its discussion for details). We ascribe the decreased crystal field in the excited state, to the 2p core hole localization of the 3d electrons thereby decreasing the overlap with the oxygen 2p orbitals.[41] The electron interactions were scaled to effectively include the screening effect of solids.[24] Here, the scaling of 3d3d ($F_{dd}$) and 2p3d ($F_{pd}$, $G_{pd}$) interactions was set to 87% and 95% of their atomic values, respectively. The scaling of the Fdd parameter is obtained accurately (~2% error) from the RIXS data as explained in supporting Figure S4 and its discussion. The reduction of the 3d3d interactions is approximately twice that of the 2p3d interactions as they contain two valence electrons. Through these parameter determination methods a well simulated $2p_{3/2}$ XAS spectrum was achieved as shown in Figure 2.

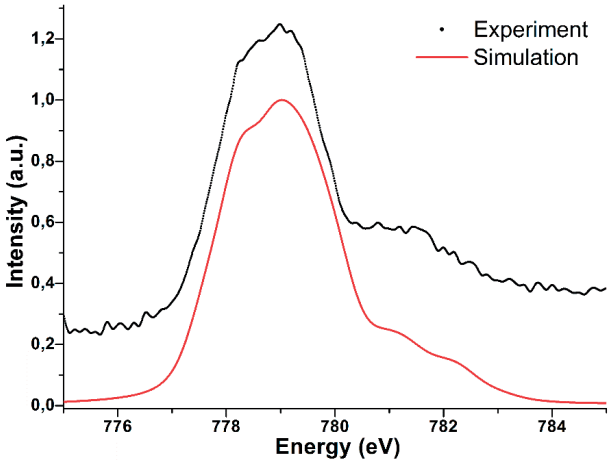


**Figure 2.** Experimental (black dots) and simulated (red solid line) cobalt $2p_{3/2}$ XAS (TFY) of $K_5H[CoW_{12}O_{40}]\cdot xH_2O$.

The presented experimental spectrum varies from a previously reported $2p_{3/2}$ XAS obtained on the same sample, but which was measured in the total electron yield (TEY) mode.[11] The observed spectral shape difference may result from a number of reasons, including: i) TFY detected XAS is a bulk probe and as such less sensitive to surface effects compared to electron yield detection (additionally, potential beam induced effects are strongest at the surface[43]). ii) Potentially TFY is sensitive to saturation effects, but the low cobalt loading and the presence of twelve heavy tungsten atoms for each cobalt likely prevent any detectable saturation effects. iii) Different experimental XAS broadenings in the different experiments.

### 3.4.3. RIXS experiment and simulation

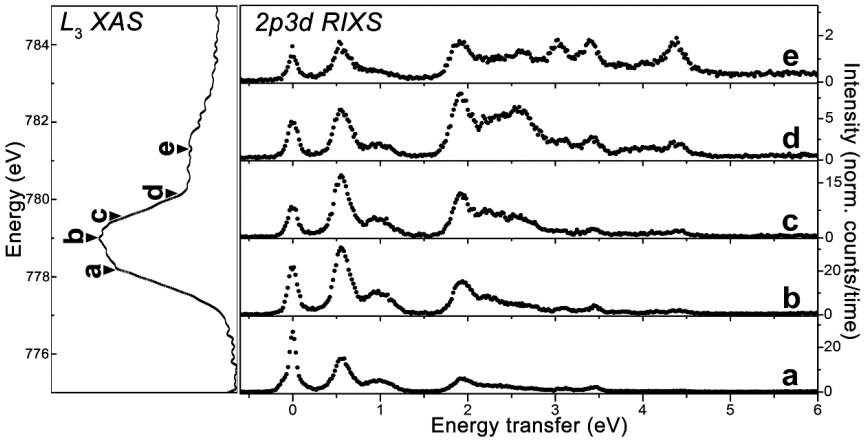


**Figure 3.** Experimental cobalt $2p_{3/2}$ XAS (left) and 2p3d RIXS (right) spectra of the $K_5H[CoW_{12}O_{40}]\cdot xH_2O$ POM, both acquired at 300 K with an LH polarized incident beam. The five RIXS spectra were acquired at excitation energies a-e indicated at the XAS spectrum.

The experimental $2p_{3/2}$ XAS and 2p3d RIXS spectra are shown in Figure 3. In the XAS panel (left), excitation energies chosen for RIXS measurements are indicated by arrows a-e. This a-e letter denomination is applied in the whole text. Note here that energy positions a-e represent the centers of incident energy windows of approximately 1.0 eV FWHM (see the Experimental Section). The corresponding 2p3d RIXS spectra (right panel) are intensity normalized to the acquisition time. The 2p3d RIXS probed at cobalt $2p_{3/2}$ edge carries the information of the elastic scattering and elementary excitations including dd, charge transfer (ligand to metal and metal to ligand), magnon and phonon (< 100 meV) excitations.[44] Low-energy phonon and magnon excitations of the $^4A_2$ ground state are invisible as the experimental resolution of 90 meV is larger than their excitation

energies. However, phonons and magnons could lead to a broadening of the elastic peak related to the $^4A_2$ ground state, as well as additional broadening of the dd-excitations to the $^4T_1$ and the $^4T_2$ states. Charge transfer excitations are typically minor for $Co^{II}$-$O_x$ species[18] and broader than the observed features, especially at excitation energy e, were they appear relatively strong. The main energy transfer spectral features are thus ascribed to dd excitations. From the five RIXS spectra, it can be found that: i) spectral features appear at fixed energy transfer exhibiting their dd excitation nature; ii) the intensity ratio between dd features changes with excitation energy; iii) more dd features are observed at higher energy transfer in RIXS spectra acquired at higher excitation energies.

**Table 1.** Electronic structure parameter values (in eV) used in the ligand field multiplet simulations of $2p_{3/2}$ XAS and 2p3d RIXS spectra of $K_5H[CoW_{12}O_{40}]\cdot xH_2O$.

| | initial states | intermediate states (RIXS)/ final state (XAS) | final states (RIXS) |
|---|---|---|---|
| $Co^{II}$ config | $2p^63d^7$ | $2p^53d^8$ | $2p^63d^8\underline{d}$ |
| $F^2_{dd}$ | 8.077 | 8.628 | 8.077 |
| $F^4_{dd}$ | 5.018 | 5.365 | 5.018 |
| $F^2_{pd}$ | | 5.518 | |
| $G^1_{pd}$ | | 4.102 | |
| $G^3_{pd}$ | | 2.333 | |
| $\zeta_{3d}$ | 0.066 | 0.083 | 0.066 |
| $\zeta_{2p}$ | | 9.748 | |
| 10Dq | -0.540 | -0.430 | -0.540 |
| Ds | -0.080 | -0.080 | -0.080 |
| Dt | 0.005 | 0.005 | 0.005 |
| Γ (FWHM) | | 0.400 | 0.050 |
| G (FWHM) | | 0.100/0.500 | 0.090 |

The ligand field multiplet simulation of the $Co^{II}$ 2p3d RIXS spectra employed the parameters listed in Table 1. The simulation (at 300 K) of the full RIXS transition process from $2p^63d^7$ to $2p^53d^8$ and then to $2p^63d^8\underline{d}$ yields the two-dimensional (2D) plane shown in Figure 4a. In this 2D RIXS plane, the energy transfer ($\Omega$-$\omega$) is plotted against each incident/excitation energy ($\Omega$) over the Co $2p_{3/2}$ edge. The incident energy of this generated 2D plane was shifted to fit with energies of the experimental XAS. To simulate the experimental incident beam, 1 eV FWHM Gaussian-broadened incident energy bands ($\Omega'$), centered at a-e were used. The five selected cross sections $I(\Omega'-\omega)|_{\Omega'}$ were plotted against their respective experimental spectra in Figure 4b. Here, the simulated spectra were normalized to the intensity of the first experimental dd peak (at ~0.55 eV). Although the

scaling factor for each simulated RIXS cross section is now slightly different (ratio varying between 1.0 and 1.8), this procedure allows a straightforward comparison between the inelastic features of the theoretical and experimental results. The normalization method is justified, since each spectrum was either measured at a new sample position or an averaged result from spectra measured at several positions (cf. Experimental Section), with a varying surface roughness. Surface roughness can lead to additional intensities due to reflectivity.

Overall, the simulated RIXS spectra reproduce the energy positions of the dd peaks well, especially in the energy transfer region below 2 eV. The dd features at 3.06 and 3.36 eV are also reproduced especially in spectrum e, although an additional feature at higher energy transfer is observed in the simulation. This is potentially a result of ignoring charge transfer effects in the current simulation, as charge transfer mainly affects high-energy transfer features.[15, 18]

Based on the ligand field multiplet calculations, a few selected dd excitations were labeled in Figure 5 with $D_{2d}$ and $T_d$ (in brackets) symmetry term symbols. The peak at 0.55 eV corresponds to the $^4T_2$ excited state in the $T_d$ symmetry, which is further split into $^4B_2$ and $^2E$ states due to the tetragonal $D_{2d}$ distortion. The dd peak at ~1 eV contains two dd transitions: the ground state $^4B_1$ to the $^4A_2$ and $^4E$ states. Similarly, the two states are split from the $^4T_1$ state in the $T_d$ symmetry. This ~1 eV $^4T_1$ state, indicated in Figure 5 as $^4_aT_1$, represents the $^4T_1$ state originating from the atomic multiplet $^4F$, and the $^4_bT_1$ represents the $^4T_1$ state from the atomic multiplet $^4P$. The $^4B_1$ to $^4A_2$ ($^4_bT_1$) and $^4E$ ($^4_bT_1$) transitions are at ~2.24 and ~2.43 eV (Figure 5a), respectively. The calculations show that the broad peak at ~1.93 eV consists of four doublets: $^2A_1$, $^2B_1$, $^2A_2$ and $^2E$ in $D_{2d}$ symmetry (originating from the $^2E$ and $^2T_1$ states in the $T_d$ symmetry as shown in Figure 5b).

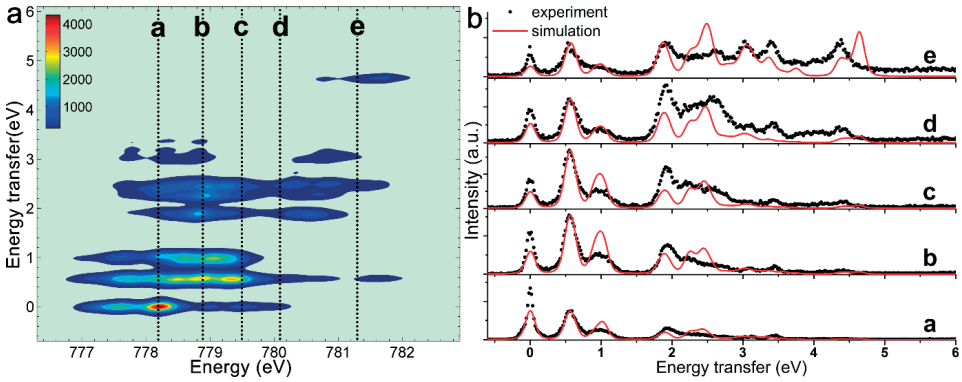


**Figure 4.** (a) The ligand field multiplet 2p3d RIXS plane of $Co^{II}$ in $K_5H[CoW_{12}O_{40}]\cdot xH_2O$. The black dotted lines correspond to centers of ~1 eV FWHM excitation bands a-e (see Figure 3). (b) The LH polarized experimental (black dotted line) and corresponding ligand field multiplet (red solid line) RIXS spectra at excitation energies a-e.

Similar excited states have been determined from optical spectra and density functional theory (DFT) calculations of the $[CoW_{12}O_{40}]^{6-}$ anions.[7-9, 16] The optical absorption measurable features at $7.8\times10^3$ cm$^{-1}$ (~0.97 eV) and $16\times10^3$ cm$^{-1}$ (~1.98 eV) were in $T_d$ symmetry assigned to the spin allowed transitions of the $^4A_2$ ground state to $^4_aT_1$ and $^4_bT_1$ states [7, 9] Equivalent assignments can also be found in the optical absorption and emission data of $T_d$ $Co^{II}$ sites in $MgAl_2O_4$.[45] Naturally, for different $Co^{II}$ $T_d$ sites, different transition energies are found. The main difference between optical absorption and 2p3d RIXS is that the relative intensities of the dd excitations are different in 2p3d RIXS, partly because the spin forbidden transitions have equivalent intensity to the spin-allowed transitions.

### 3.4.4. Boltzmann weighted RIXS simulation

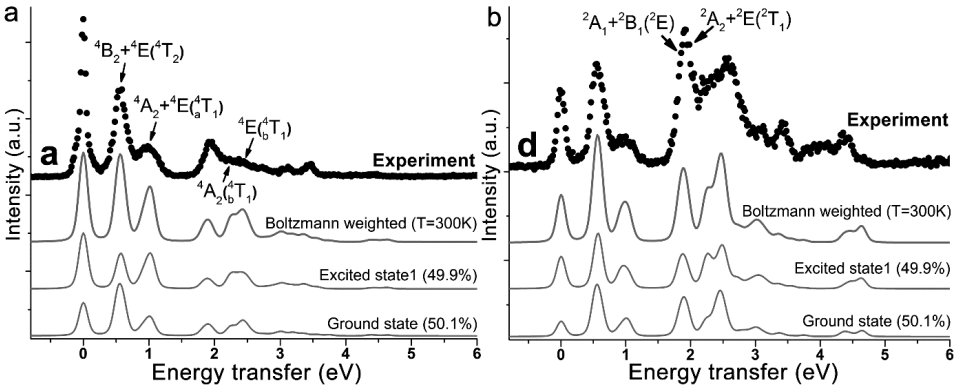


**Figure 5.** Experimental (black dots) and corresponding ligand field multiplet (grey lines) RIXS spectra at excitation energy a (panel a) and d (panel b), respectively. The theoretical ground and the first excited state RIXS spectrum are shown, together with their Boltzmann weighted sum at 300 K (spectral weights in brackets). The ligand field multiplet obtained symmetry labels of selected dd manifolds in $D_{2d}$ and $T_d$ (in brackets) symmetry are indicated.

As stated previously, the ligand field multiplet simulations for XAS and RIXS were both performed by taking into account the temperature dependent occupation of excited states. All experimental spectra were acquired at 300 K and ligand field multiplet analysis indicated that the spectral weight from the ground and first excited state needs to be considered. The spectral effect of summing Boltzmann-weighted excited states with the ground state was demonstrated for CoO 2p3d RIXS,[18] in which the first five states account for 93% of room temperature populated states. Here, the energy difference between the ground and first excited state was calculated to be ~0.6 meV. These two states account for ~100% of room temperature populated states, where the population

percentage of the first excited state is ~49.9% (the occupation fraction $p_i = \exp[-\Delta E_i/kT)/\Sigma_j \exp(-\Delta E_j/kT]$, with k being the Boltzmann constant). RIXS simulations for the ground state, the first excited state, and the Boltzmann weighted spectra at 300 K, along with respective experimental spectra at excitation energies a and d, are shown in Figure 5. The comparison for excitation energies b, c and e are given in Figure S5. The simulated RIXS spectra of the ground and first excited state are similar, except for minor different intensity ratios between dd features. This results from the different intermediate states which the ground and the excited states reach.

### 3.4.4. Investigation of $Co^{II}$ site $D_{2d}$ distortion

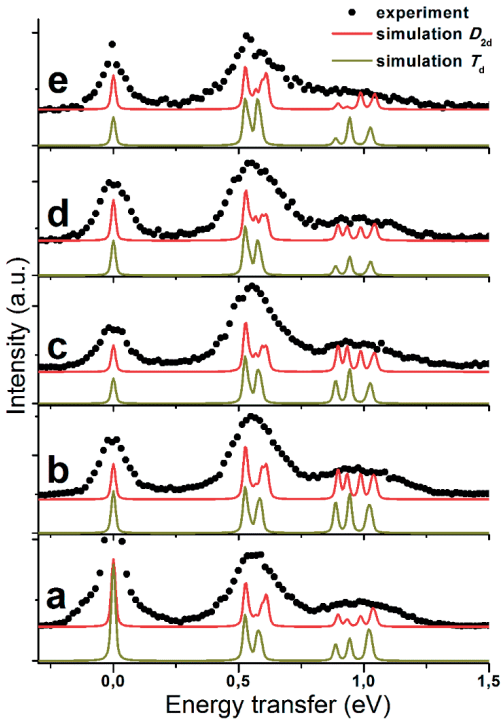


**Figure 6.** Low energy transfer 2p3d RIXS spectral cross sections at excitation energies a-e: experiment (black dots) and simulations in $T_d$ (dark yellow solid lines) and $D_{2d}$ (red solid lines) symmetries.

The present RIXS data suggest that the $Co^{II}$ site is distorted in the α-Keggin $[CoW_{12}O_{40}]^{6-}$ anion. Figure 6 shows the low energy transfer features of simulated 2p3d RIXS spectra in $T_d$ and $D_{2d}$ symmetries in comparison with the experimental results. The calculations represent room temperature spectra (Boltzmann weighting included) and their parameters are listed in Table S1.

The deliberately applied, too small final state broadening allows to view the 3d spin-orbit coupling induced splittings of the $^4T_2$ peak at ~0.55 eV and the $^4T_1$ peak at ~1.0 eV in $T_d$ symmetry and the additional splittings in $D_{2d}$ symmetry. In our calculations the 3d spin-orbit coupling is unquenched and thus at its atomic value. Even for this maximum value, it alone cannot account for the broadening of the $^4T_2$ and $^4T_1$ peaks. Including the $D_{2d}$ site distortion an improved agreement is found for: the broadening of the $^4T_2$ peak in spectra a-e, the asymmetric shape of the $^4T_2$ peak (especially for spectrum c), the spectral weight distribution of the $^4T_1$ peak for all spectra, and the relative intensity ratio between the $^4T_2$ and $^4T_1$ peaks (especially for spectra a and b). Note that figure 4b gives the comparison of the calculation in $D_{2d}$ symmetry to the experiment, using appropriate broadenings. From Figure 6 it can now be seen that a description of the system in pure $T_d$ symmetry would lead to almost equal intensity ratios of the $^4T_2$ to $^4T_1$ peaks in spectra a and b, which is not the case in the experiment. This relative intensity ratio is also not likely to be influenced by phonons (an alternative reason for broadening of the $^4T_2$ and $^4T_1$ peaks) as both peaks are likely to have similar vibrational couplings (both quartet in nature). The here obtained distortion parameters are Ds= -0.08 eV and Dt= 0.005 eV. The exact values of the distortion parameters is difficult to obtain from the RIXS spectra with the current resolution, but in the Supporting Information and supporting Figure S6 it is explained how these parameters were obtained precisely. Using the derived Ds and Dt values, the point charge model[47] and a $Co^{II}$ radius of 72 pm[48] we obtain two sets of Co-O distances of 1.89 and 1.90-1.97 Å, roughly in agreement with the 1.898(12) and 1.904(12) Å values found by X-ray crystallography.[9] Note that the accuracy in numbers obtained from crystallography is much higher than those obtained from the point charge model (LFM/RIXS), but that there is a difference between x-ray diffraction and x-ray spectroscopy regarding symmetry distortions. Spectroscopy measures the energy position of states that are determined by the point group, while diffraction measures the symmetry distortions in the unit cell of the space group. This implies that if the distortion is not ordered, it will not be visible in diffraction, while in 2p3d RIXS such unordered distortions will be visible in energy position shifts. Despite our solid arguments in favor of the presence of a $Co^{II}$ site distortion, the present experimental resolution cannot definitively establish it, especially when it comes to the exact determination of the Ds and Dt values. The experimental resolution of cobalt 2p3d RIXS has been improved to around 20 meV at the new beamline ID 32 in the European Synchrotron Radiation Facility (ESRF; Grenoble, France) and with a 20 meV resolved experiment, the cobalt symmetry distortions would be more clearly and accurately probed.

### 3.4.5. Energy levels under atomic multiplet, tetrahedral field, tetragonal distortion and 3d spin-orbit coupling

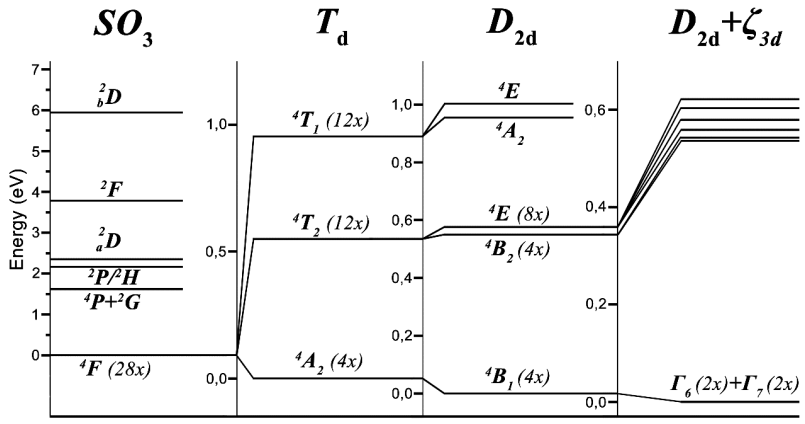


**Figure 7.** From left to right: branching of the $Co^{II}$ energy levels due to atomic multiplet effects (spherical $SO_3$ symmetry), followed by branching in tetrahedral $T_d$ and tetragonal $D_{2d}$ symmetric ligand fields, followed by application of 3d spin-orbit coupling $\zeta_{3d}$. The energy of the ground state is set to zero in each scheme. The notation '+' indicates the energy difference between two term symbols is too small to be shown. The notation '/' indicates the term symbols are degenerate.

Figure 7 shows the energetic levels of the ground and selected excited states due to atomic multiplets, tetrahedral crystal fields, tetragonal crystal fields, and 3d spin-orbital coupling. Energy values of most presented states are listed in Table 2. In the spherical symmetry ($SO_3$), the 28-fold $^4F$ multiplet state is the ground state. Note that the energy difference of $^4P$ and $^2G$ states was calculated to be 7.3 meV, which renders the states indistinguishable in Figure 7. The $^2P$ and $^2H$ multiplet states were calculated to be the 28-fold degenerate[46] at 2.17 eV above the ground state. In the second panel (from the left) atomic multiplet states are branched in tetrahedral symmetry (10Dq= -0.54 eV). The four-fold $^4A_2$ multiplet state, branched from $^4F$ state, forms the ground state, while $^4T_2$ and $^4T_1$ are the first two excited states. The $^4A_2$ state further branches to the $^4B_1$ state under the tetragonal ($D_{2d}$) distortion of the cobalt ion. The first two excited states $^4T_2$ and $^4T_1$ further branch into four excited states $^4B_2$, $^4E$, $^4A_2$ and $^4E$. The obtained distortion parameters are Ds= -0.08 eV and Dt= 0.005 eV. The application of 3d spin-orbit coupling (66 meV) gives rise to two double degenerate $\Gamma_6$ and $\Gamma_7$ states, branched from the $^4B_1$ ground state, which are the Kramer's doublets. Note that Figure 7 is an incomplete picture in which compositions of each energy level, as well as the energy branching, are assumed to be 100% pure without mixing. Such assumption is improper and can hardly explain the splitting of $^4B_1$ or $^4B_2$ states into $\Gamma_6$ and $\Gamma_7$ states due to the 3d spin-orbit coupling. A more realistic demonstration of compositions and branchings of microstates is discussed in the section below.

### 3.4.6. Wavefunction decomposition

**Table 2.** Wavefunction description of the system ground state and selected lowest states. Columns 1-4: point group symmetries, energies of states, degeneracies of states, the term symbol representation of states in corresponding symmetries, respectively. Columns 5-7: compositions of states in atomic term symbols, cubic symmetry term symbols and one-electron orbitals. Calculations in each point group symmetry are all based on ligand field multiplet parameters listed in Table 1.

| Symmetry | Energy (eV) | Deg. | Term Symbol | Atomic Composition (%) | Cubic Composition (%) | Orbital Composition (%) |
|---|---|---|---|---|---|---|
| $SO_3$ | 0.0000 | 28 | $^4F$ | 100 | | |
| | 1.6192 | 12 | $^4P$ | 100 | | |
| | 1.6265 | 18 | $^2G$ | 100 | | |
| | 2.1662 | 6 | $^2P$ | 100 | | |
| | 2.1662 | 22 | $^2H$ | 100 | | |
| | 2.3536 | 10 | $^2_aD$ | $21.8\|^2_aD> + 78.2\|^2_bD>$ | | |
| | 3.7853 | 14 | $^2F$ | 100 | | |
| | 5.9464 | 10 | $^2_bD$ | $21.8\|^2_bD> + 78.2\|^2_aD>$ | | |
| $T_d$ | 0.0000 | 4 | $^4A_2$ | $100\|^4F>$ | $100\ ^4A_2$ | $100\|e^4t_2^3>$ |
| | 0.5399 | 12 | $^4T_2$ | $100\|^4F>$ | $100\ ^4T_2$ | $100\|e^3t_2^4>$ |
| | 0.9369 | 12 | $^4T_1$ | $97.4\|^4F> + 2.6\|^4P>$ | $100\ ^4T_1$ | $65.8\|e^2t_2^5> + 34.2\|e^3t_2^4>$ |
| $D_{2d}$ | 0.0000 | 4 | $^4B_1$ | $100\|^4F>$ | $100\ ^4A_2$ | $100\|e^2b_2^1a_1^2b_1^2>$ |
| | 0.5400 | 4 | $^4B_2$ | $100\|^4F>$ | $100\ ^4T_2$ | $100\|e^2b_2^2a_1^2b_1^1>$ |
| | 0.5664 | 8 | $^4E$ | $99.5\|^4F> + 0.5\|^4P>$ | $97.1\|^4T_2> + 2.9\|^4T_1>$ | $84.6\|e^3b_2^1a_1^1b_1^2> + 14.2\|e^3b_2^1a_1^2b_1^1> + 1.2\|e^3b_2^2a_1^1b_1^1>$ |
| | 0.9400 | 4 | $^4A_2$ | $87.6\|^4F> + 12.4\|^4P>$ | $100\ ^4T_1$ | $53.8\|e^2b_2^2a_1^1b_1^2> + 46.2\|e^4b_2^1a_1^1b_1^1>$ |
| | 0.9859 | 8 | $^4E$ | $99.4\|^4F> + 0.6\|^4P>$ | $97.4\|^4T_1> + 2.6\|^4T_2>$ | $71.7\|e^3b_2^2a_1^1b_1^1> + 27.0\|e^3b_2^1a_1^2b_1^1> + 1.3\|e^3b_2^1a_1^1b_1^2>$ |
| $D_{2d}+\zeta_{3d}$ | 0.0000 | 2 | $\Gamma_6$ | $99.8\|^4F> + 0.1\|^2G>$ | $97.6\|^4A_2> + 2.2\|^4T_2> + 0.2\|^2T_2>$ | $97.6\|e^2b_2^1a_1^2b_1^2> + 1.4\|e^2b_2^2a_1^2b_1^1> + 0.8\|e^3b_2^1a_1^1b_1^2> + 0.2\|e^3b_2^1a_1^2b_1^1>$ |
| | 0.0006 | 2 | $\Gamma_7$ | $99.8\|^4F> + 0.1\|^2G>$ | $97.8\|^4A_2> + 2.0\ \|^4T_2> + 0.2\|^2T_2>$ | $97.8\|e^2b_2^1a_1^2b_1^2> + 1.5\|e^3b_2^1a_1^1b_1^2> + 0.4\|e^3b_2^1a_1^2b_1^1> + 0.2\|e^2b_2^2a_1^2b_1^1>$ |

The detailed wavefunction descriptions of the compound ground state and a few excited states, are presented in Table 2 under different point group symmetries. All calculations were performed based on the ligand field multiplet parameters listed in Table 1. In spherical $SO_3$ symmetry all atomic states are described by pure atomic term symbols, with the exception that the $^2D$ term

symbol occurs twice and each $^2$D state is a linear combination of both. We discriminate the different symbols as $^2_a$D and $^2_b$D. Note that energies of the $^2$P and the $^2$H manifolds are intrinsically degenerate.[46] Applying a tetrahedral ligand field (here 10Dq=-0.54 eV), the $^4$F ground state is split into $^4$A$_2$, $^4$T$_2$ and $^4$T$_1$ states. The first two manifolds are pure in $^4$F character (if 3d spin-orbit coupling is neglected), as they are the only $^4$A$_2$ and $^4$T$_2$ states of the 3d$^7$ manifold. The $^4$T$_1$ state contains ~3% $^4$P character due to the mixing of two $^4$T$_1$ symmetry states. Similarly, in the one-electron orbital descriptions, the $^4$A$_2$ and $^4$T$_2$ states are both pure and with an $e^4t_2^3$ and an $e^3t_2^4$ occupation each, while the $^4$T$_1$ multiplet contains 65.8% $|e^2t_2^5>$ and 34.2% $|e^3t_2^4>$.

Changing the $T_d$ to the $D_{2d}$ symmetry, the $^4$A$_2$ ground state branches into the $^4$B$_1$ state, which retains its pure $^4$F character and a corresponding pure $|e^2b_2^1a_1^2b_1^2>$ one-electron orbital description. The pure $^4$T$_2$ state branches into a pure $^4$B$_2$ state and a $^4$E state, which mixes with another $^4$E state, turning it into a complex mixed orbital description. The main component is the 84.6% $|e^3b_2^1a_1^1b_1^2>$ state that can be understood as all spin-up electrons occupied plus a spin-down electron in the e and b$_1$ orbitals each. The remaining ~15% of this $^4$E state contains other distributions of electrons over the e, b$_2$, a$_1$ and b$_1$ orbitals (cf. Table 2). Furthermore, apart from the main compositions, a 2.9% $|^4T_1>$ cubic symmetry or a 0.5% $|^4P>$ atomic term symbol character is found for this $^4$E state. Switching on the 3d spin-orbit coupling gives rise to assignments in double group notations $\Gamma_6$ and $\Gamma_7$. Most importantly with the inclusion of 3d spin-orbit coupling, the $^4$B$_1$ ground state is not a pure quartet state anymore, but an approximately 0.2% doublet character is mixed. In the orbital composition, effects of 3d spin-orbit coupling are larger which lead around 2% states with different orbital compositions to mix into the ground state. As can be seen in the last column, this 2% states is mainly related to the $^4$T$_2$ excited configuration, which mix via the 3d spin-orbit coupling.

## 3.5. CONCLUSIONS

Cobalt 2p$_{3/2}$ XAS and 2p3d RIXS spectra were acquired for the sample $K_5H[CoW_{12}O_{40}]\cdot xH_2O$. The high energy resolution (~0.09 eV FWHM) Co 2p3d RIXS data of the single Co centered polyoxometalate $K_5H[CoW_{12}O_{40}]\cdot xH_2O$ is reported for the first time, which experimentally revealed the UV/vis unmeasurable low energy dd transition features. The experimental XAS and RIXS spectra were adequately reproduced with ligand field multiplet simulations by considering the temperature dependent occupation of excited states. In fact these data represent the first reported tetrahedral-like $Co^{II}$ soft RIXS data. The ligand field multiplet data simulations also allowed an effective discussion about the potential Co site tetragonal distortion. Parameters accounting for the ligand field on the cobalt ion have strengths of 10Dq = -0.54 eV, Ds = -0.08 eV and Dt = 0.005 eV. An improved experimental resolution is still required though to be conclusive on this topic. The ligand field multiplet RIXS simulation addressed the labeling of a few observed dd features and it

also enabled the comparison with previous dd transition assignments from optical data and DFT calculations. As RIXS clearly demonstrated both optical spin allowed and forbidden transitions, the current dd feature assignments show a higher accuracy. The wavefunction decomposition analyses, using ligand field multiplet projection methods, provided realistic and detailed origins of each dd transition, both from one-electron orbital and term symbol descriptions. In conclusion, the high energy resolution Co 2p3d RIXS spectra and ligand field multiplet simulations offered unprecedented information of the Co electronic structure in $K_5H[CoW_{12}O_{40}]\cdot xH_2O$, suggesting further applications of this technique to explore the potential water oxidation catalytic activity related Co electronic structures in different Co-containing POMs.

## ACKNOWLEDGMENTS

This work was financially supported by the China Scholarship Council and the ERC advanced grant XRAYonACTIVE, number 340279. We thank Wen-Bin Wu, Jun Okamoto and Di-Jing Huang in NSRRC for technical support. We thank Elliot N. Glass and Craig L. Hill in Emory University, USA, for offering the sample. We thank Tanja Cuk for nice discussion. Matti van Schooneveld, Ru-pan Wang and Frank de Groot helped me on data analysis and paper preparation.

## Supporting Information available in Appendix 3

## REFERENCES


(1) Khodakov, A. Y.; Chu, W.; Fongarland, P. *Chem. Rev.* **2007,** *107*, 1692-1744.

(2) Matsumoto, Y.; Murakami, M.; Shono, T.; Hasegawa, T.; Fukumura, T.; Kawasaki, M.; Ahmet, P.; Chikyow, T.; Koshihara, S.; Koinuma, H. *Science* **2001,** *291*, 854-856.

(3) Yin, Q. S.; Tan, J. M.; Besson, C.; Geletii, Y. V.; Musaev, D. G.; Kuznetsov, A. E.; Luo, Z.; Hardcastle, K. I.; Hill, C. L. *Science* **2010,** *328*, 342-345.

(4) Huang, Z. Q.; Luo, Z.; Geletii, Y. V.; Vickers, J. W.; Yin, Q. S.; Wu, D.; Hou, Y.; Ding, Y.; Song, J.; Musaev, D. G.; Hill, C. L.; Lian, T. Q. *J. Am. Chem. Soc.* **2011,** *133*, 2068-2071.

(5) Lv, H. J.; Song, J.; Geletii, Y. V.; Vickers, J. W.; Sumliner, J. M.; Musaev, D. G.; Kogerler, P.; Zhuk, P. F.; Bacsa, J.; Zhu, G. B.; Hill, C. L. *J. Am. Chem. Soc.* **2014,** *136*, 9268-9271.

(6) Lv, H. J.; Geletii, Y. V.; Zhao, C. C.; Vickers, J. W.; Zhu, G. B.; Luo, Z.; Song, J.; Lian, T. Q.; Musaev, D. G.; Hill, C. L. *Chem. Soc. Rev.* **2012,** *41*, 7572-7589.

(7) Nomiya, K.; Miwa, M.; Kobayashi, R.; Aiso, M. *Bull. Chem. Soc. Jpn.* **1981,** *54*, 2983-2987.

(8) Kojima, K.; Matsuda, J. *Bull. Chem. Soc. Jpn.* **1985,** *58*, 821-825.

(9) Glass, E. N.; Fielden, J.; Kaledin, A. L.; Musaev, D. G.; Lian, T. Q.; Hill, C. L. *Chem.-Eur. J.* **2014,** *20*, 4297-4307.

(10) Schiwon, R.; Klingan, K.; Dau, H.; Limberg, C. *Chem. Commun.* **2014,** *50*, 100-102.

(11) Hibberd, A. M.; Doan, H. Q.; Glass, E. N.; de Groot, F. M. F.; Hill, C. L.; Cuk, T. *J. Phys. Chem. C* **2015,** *119*, 4173-4179.

(12) van Schooneveld, M. M.; Gosselink, R. W.; Eggenhuisen, T. M.; Al Samarai, M.; Monney, C.; Zhou, K. J. J.; Schmitt, T.; de Groot, F. M. F. *Angew. Chem.-Int. Edit.* **2013,** *52*, 1170-1174.

(13) de Groot, F. M. F. *Coord. Chem. Rev.* **2005,** *249*, 31-63.

(14) Waegele, M. M.; Doan, H. Q.; Cuk, T. *J. Phys. Chem. C* **2014,** *118*, 3426-3432.

(15) Magnuson, M.; Butorin, S. M.; Guo, J. H.; Nordgren, J. *Phys. Rev. B* **2002,** *65*, 205106.

(16) Maestre, J. M.; Lopez, X.; Bo, C.; Poblet, J. M.; Daul, C. *Inorg. Chem.* **2002,** *41*, 1883-1888.

(17) Glass, E. N.; Fielden, J.; Huang. Z. Q.; Xiang. X.; Musaev, D. G.; Lian, T. Q.; Hill, C. L. *Inorg. Chem.* **2016,** *55*, 4308–4319.

(18) van Schooneveld, M. M.; Kurian, R.; Juhin, A.; Zhou, K. J.; Schlappa, J.; Strocov, V. N.; Schmitt, T.; de Groot, F. M. F. *J. Phys. Chem. C* **2012,** *116*, 15218-15230.

(19) Lai, C. H.; Fung, H. S.; Wu, W. B.; Huang, H. Y.; Fu, H. W.; Lin, S. W.; Huang, S. W.; Chiu, C. C.; Wang, D. J.; Huang, L. J.; Tseng, T. C.; Chung, S. C.; Chen, C. T.; Huang, D. J. *J. Synchrot. Radiat.* **2014,** *21*, 325-332.

(20) Fung, H. S.; Chen, C. T.; Huang, L. J.; Chang, C. H.; Chung, S. C.; Wang, D. J.; Tseng, T. C.; Tsang, K. L. *AIP Conf. Proc*. **2004**, *705*, 655-658.

(21) Ghiringhelli, G.; Brookes, N. B.; Annese, E.; Berger, H.; Dallera, C.; Grioni, M.; Perfetti, L.; Tagliaferri, A.; Braicovich, L. *Phys. Rev. Lett.* **2004,** *92*, 117406.

(22) Kuiper, P.; Guo, J. H.; Sathe, C.; Duda, L. C.; Nordgren, J.; Pothuizen, J. J. M.; de Groot, F. M. F.; Sawatzky, G. A. *Phys. Rev. Lett.* **1998,** *80*, 5204-5207.

(23) Cowan, R. D. *J. Opt. Soc. Am.* **1968,** *58*, 808-818.

(24) Cowan, R. D. *The Theory of Atomic Structure and Spectra*; University of California Press: Berkeley, CA, 1981.

(25) Thole, B. T.; van der Laan, G.; Butler, P. H. *Chem. Phys. Lett.* **1988,** *149*, 295-299.

(26) de Groot, F. M. F.; Kotani, A. *Core Level Spectroscopy of Solids*; CRC Press: Boca Raton, FL, 2008.

(27) Stavitski, E.; de Groot, F. M. F. *Micron* **2010,** *41*, 687-694.

(28) de Groot, F. M. F.; Fuggle, J. C.; Thole, B. T.; Sawatzky, G. A. *Phys. Rev. B* **1990,** *41*, 928-937.

(29) Wasinger, E. C.; de Groot, F. M. F.; Hedman, B.; Hodgson, K. O.; Solomon, E. I. *J. Am. Chem. Soc.* **2003,** *125*, 12894-12906.

(30) Haverkort, M. W.; Sangiovanni, G.; Hansmann, P.; Toschi, A.; Lu, Y.; Macke, S. *Europhys. Lett.* **2014,** *108*, 57004.

(31) Haverkort, M. W.; Zwierzycki, M.; Andersen, O. K. *Phys. Rev. B* **2012,** *85*, 165113.

(32) Hariki, A.; Ichinozuka, Y.; Uozumi. T. *J. Phys. Soc. Jpn.* **2013,** *82*, 043710.

(33) Hariki, A.; Yamanaka, A.; Uozumi. T. *J. Phys. Soc. Jpn.* **2015,** *84*, 073706.

(34) Roemelt, M.; Manganas, D.; DeBeer, S.; Neese, F. *J. Chem. Phys.* **2013,** *138,* 204101-204122.

(35) Manganas, D.; Roemelt, M.; Hävecker, M.; Trunschke, A.; Knop-Gericke, A.; Schlögl, R.; Neese, F. *Phys. Chem. Chem. Phys.* **2013,** *15*, 7260-7276.

(36) Lundberg, M.; Kroll, T.; DeBeer, S.; Bergmann, U.; Wilson, S. A.; Glatzel, P.; Nordlund, D.; Hedman, B.; Hodgson, K. O.; Solomon, E. I. *J. Am. Chem. Soc.* **2013,** *135*, 17121-17134.

(37) Pinjari, R. V.; Delcey, M. G.; Guo, M.Y.; Odelius, M.; Lundberg, M. *J. Chem. Phys.* **2014,** *141*, 124116.

(38) Kramers, H. A.; Heisenberg, W. *Z. Phys.* **1925,** *1*, 681-701.

(39) de Groot, F. M. F. *Phys. Rev. B* **1996,** *53*, 7099-7110.

(40) Casanpastor, N.; Gomezromero, P.; Jameson, G. B.; Baker, L. C. W. *J. Am. Chem. Soc.* **1991,** *113*, 5658-5663.

(41) Cramer, S. P.; de Groot, F. M. F.; Ma, Y.; Chen, C. T.; Sette, F.; Kipke, C. A.; Eichhorn, D. M.; Chan, M. K.; Armstrong, W. H.; Libby, E.; Christou, G.; Brooker, S.; McKee, V.; Mullins, O. C.; Fuggle, J. C. *J. Am. Chem. Soc.* **1991,** *113*, 7937-7940.

(42) Stöhr, J. *NEXAFS Spectroscopy*, 1st ed.; Springer-Verlag: New-York, 1992; Vol 25.

(43) van Schooneveld, M. M.; DeBeer, S. *J. Electron Spectrosc. Relat. Phenom.* **2015,** *198*, 31-56.

(44) Ament, L. J. P.; van Veenendaal, M.; Devereaux, T. P.; Hill, J. P.; van den Brink, J. *Rev. Mod. Phys.* **2011,** *83*, 705-767.

(45) Nataf, L.; Rodriguez, F.; Valiente, R.; Ulanov, V. *J. Lumines.* **2009,** *129*, 1602-1605.

(46) Oliva, J. M. *Phys. Lett. A* **1997,** *234*, 41-44.

(47) Pisarev, R. V.; Kalashnikova, A. M.; Schops, O.; Bezmaternykh, L. N. *Phys. Rev. B* **2011,** *84*, 075106.

(48) Shannon, R. D. *Acta Crystallogr. Sect. A* **1976,** *32*, 751-767.

# Appendix 3

Explanation of the monochromator system at beamline 05A1 at NSRRC.

UV/vis and FT-IR data of $K_5H[CoW_{12}O_{40}]\cdot 12H_2O$.

LFM XAS and RIXS simulation.

Determination of 10Dq and Slater parameters from a combined XAS/RIXS approach.

Boltzmann weighted LFM RIXS cross sections at excitation energies b, c and e.

Determination of $D_{2d}$ distortion parameters from RIXS data.

**Explanation of the monochromator system at beamline 05A1 at NSRRC**

The active-bending grating monochromator (AGM) and the active-bending grating spectrometer (AGS) are kept at the exact mirror condition when the photon energy is changed. Under these conditions the elastic photons with different energies are focused onto the same position on the CCD.

For calibration of the AGM-AGS system in a small energy range, it is possible to change the photon energy by only changing the angle of the AGM without changing the angle of AGS. By changing the angle of AGM only, elastic scattering from different incident energies are focused on different positions of CCD. In our case, first we measured the elastic scattering of 782 eV incident energy, and by changing the AGM, the elastic scattering of 780 eV incident energy was measured on the CCD as a 2 eV energy loss (inelastic scattering) of the 782 eV incident energy. By this method, the two elastic peaks on the detector are separated. The widths (full width at half maximum) of these peaks were fitted to be ~ 5.1 pixels, which corresponds to ~91 meV.

**UV/vis and FT-IR data of $K_5H[CoW_{12}O_{40}]\cdot 12H_2O$**

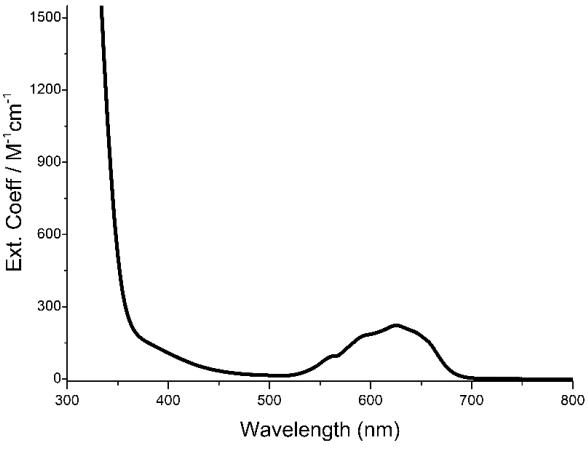


**Figure S1.** UV/vis spectra of $K_5H[CoW_{12}O_{40}]\cdot 12H_2O$.

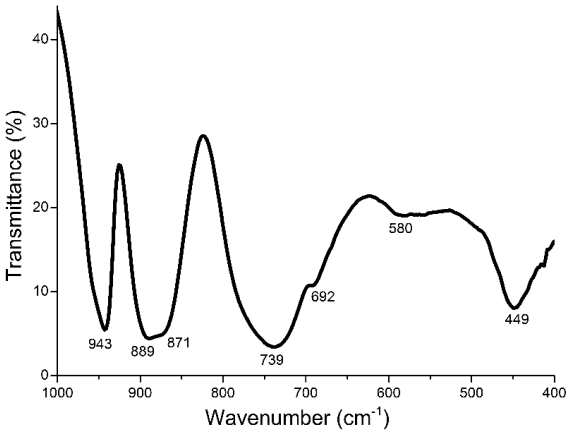


**Figure S2.** FT-IR spectra of $K_5H[CoW_{12}O_{40}]\cdot 12H_2O$.

Spectra in Figures S1 and S2 provide a basic characterization of the compound which can be used as a benchmark in future experiments to ensure the compound identity.

**LFM XAS simulation**

In our simulation, the Co sites were approximated as pure $Co^{II}$ for which the initial state of XAS could be effectively described by a $2p^63d^7$ configuration. All dipole allowed transitions from the initial $2p^63d^7$ configuration to the final/excited state $2p^53d^8$ configuration were considered. The *initial* $3d^7$ state is affected by the 3d spin-orbit coupling ($\zeta_{3d}$), 3d-3d electron interactions ($F_{dd}$) and the ligand field (10Dq, Dt, Ds); while the excited $2p^53d^8$ state is affected furthermore by the 2p spin-orbit coupling ($\zeta_{2p}$) and 2p-3d electron interactions ($F_{pd}$, $G_{pd}$). The superexchange field was neglected as each cobalt ion is isolated within the $W_{12}O_{40}$ cage, which essentially implies the existence of very weak cobalt-cobalt interactions, and tungsten with an empty 5d band shows no magnetic interactions with cobalt. The 3d spin-orbit coupling was included by using the atomic Hartree-Fock value. The simulated discrete transitions were convoluted with a Lorentzian function Γ and a Gaussian function G with empirical values to account for the 2p core hole lifetime broadening (0.4 eV FWHM) and experimental resolution (0.5 eV FWHM), respectively. The

simulation was performed by setting the temperature to 300 K in CTM4XAS interface to account for all states involved (Boltzmann weight).

**LFM RIXS simulation**

The $Co^{II}$ 2p3d inelastic scattering cross section is dominated by resonant scattering via the $2p^53d^8$ intermediate states. This reduces the calculation to transitions of $2p^63d^7$ via $2p^53d^8$ to $2p^63d^8\underline{d}$ final state. The general 2p3d RIXS function $F(\Omega, \omega)$ can be described by the Kramers-Heisenberg formula:[26, 30, 31]

$$F(\Omega,\omega)=\sum_f\left|\sum_i\frac{\langle 3d^{n+1}\underline{d}\,|T_2|\,2p^53d^{n+1}\rangle\langle 2p^53d^{n+1}|T_1|3d^n\rangle}{E_{3d^n}+\Omega-E_{2p^53d^{n+1}}+i\Gamma_{2p^53d^{n+1}}}\right|^2\times\delta\left(E_{3d^n}-E_{3d^{n+1}\underline{d}}+\Omega-\omega\right)$$

where $3d^n$, $2p^53d^{n+1}$ and $3d^{n+1}\underline{d}$ indicate initial, intermediate ($i$) and final ($f$) states, respectively. The $\Omega$ and $\omega$ represent the incoming and outgoing energies. $T_1$ and $T_2$ are dipole transition operators for absorption and emission processes. The $\delta$ term implies the energy conservation for the overall 2p3d RIXS process, which also contains the Lorentzian broadening due to the lifetime of final states. The simulated 2p3d RIXS spectra were broadened by both Lorentzian and Gaussian functions due to the same mechanisms mentioned in the above XAS simulation section. The interference effects were taken into account due to the fact that the energy differences between intermediate states are in the same order of magnitude as their lifetime broadenings ($\Gamma_i$).[31] Boltzmann weighted calculation were performed to simulate the experimental conditions, and contributions of two separate states (ground state and the first excited state) to the simulated RIXS spectra were considered. The 2p3d RIXS spectra were measured with p polarization (linear horizontal polarization) and a 90º horizontal scattering geometry. Since powder samples are oriented randomly, this LH polarization geometry was simulated by using the equal sum of [$\sigma_{in}$ to $\pi_{out}$] and [$\pi_{in}$ to $\sigma_{out}$] polarizations.[36]

**Determination of 10Dq and Slater parameters from a combined XAS/RIXS approach**

The values of the effective ligand field parameters 10Dq in the ground state (GS) and excited state (or intermediate state; IS) used in the XAS/RIXS simulations were obtained from a combined XAS/RIXS simulation as shown in Figure S3. First, the ground state 10Dq value is obtained from RIXS since d-d excitation features in RIXS spectra: i) are sharper than features in $L_3$ edge XAS due to the smaller final state lifetime broadening and higher experimental resolution; ii) can be directly correlated to values of ligand field parameters and the 3d-3d interaction (see in Table 1),

whereas in 2p XAS simulations, the 2p-3d interaction and the 2p spin-orbit coupling also affect the spectral shape. From Figure S3(b) it is clear that the first dd excitations are only well reproduced for an effective 10Dq of -0.55 eV, while -0.50 and -0.60 eV are clearly giving poor matches. Note that the energy positions of these excitations are independent of the values of the Slater-Condon parameters (see Figure S4 and its discussion). Then, using this value initially also in the excited state to reproduce the XAS spectrum, a slight mismatch between experiment and theory is found as shown in Figure S3(a). By reducing the GS 10Dq by 20%, a better spectral match is obtained between experiment and theory w.r.t. the intensity profile of the edge (clear at 779.5 eV). We ascribe the reduction to the 2p core hole causing a localization of the 3d electrons, thereby decreasing the overlap with the oxygen 2p orbitals, implying a decreased crystal field.[41]

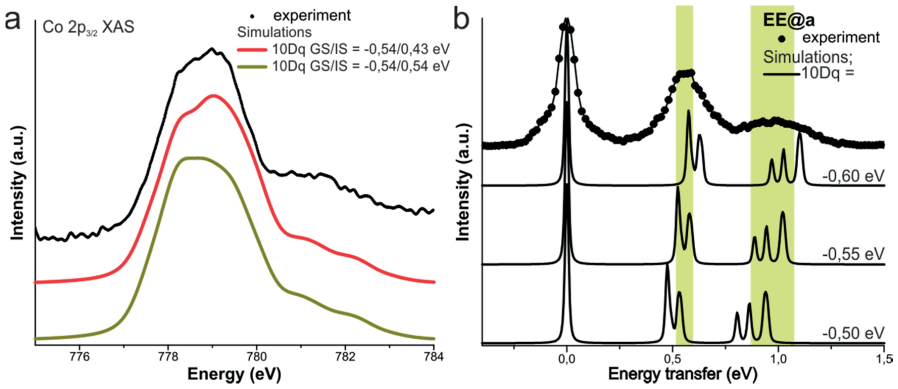


**Figure S3.** (a) Experimental (black dotted line) and simulated Co $2p_{3/2}$ XAS spectra using exactly the LFM parameters reported in Table 1 of the main text (red solid line), or those with only the intermediate state 10Dq value changed to the ground state value (dark yellow solid line). (b) Experimental (black, connected dotted line) and simulated Co 2p3d RIXS spectra using the parameters in Table 1, without a tetragonal distortion (Ds and Dt are 0 eV) and a smaller final state broadening, and varying GS 10Dq to highlight the sensitivity of RIXS to the determination of the effective GS 10Dq.

Above the RIXS data solidly fixed the effective 10Dq value in the GS, and Figure S4 shows they also significantly help to determine the Slater-Condon parameter values. Especially the $F_{dd}$ parameter is dictated by them through the energy positions of the high energetic RIXS transitions. In our calculations the Slater-Condon parameters, including direct Coulomb terms $F_{dd}$, $F_{pd}$ and the exchange term $G_{pd}$, were reduced to 87%, 95%, 95%, respectively, of their atomic multiplet values (set to 80% of the Hartree-Fock calculated values) to correct for omitted charge transfer effects.[13] Figure S4 justifies the choices of these scaling factors. When atomic values are taken (100% values

in the graph) only the peak positions of the first two dd excitations are well reproduced (those are set by 10Dq solely), but higher energy features are not matching the experiment. When the $F_{dd}$ parameter is scaled to 87% of its atomic value, the agreement between the energy positions of the dd features in the experiment and simulation is largely improved. Note that a change of 2% in the $F_{dd}$ scaling already gives a significantly worse spectral agreement between experiment and theory. Furthermore, the reduction of the 3d3d interactions is approximately twice that of the 2p3d interactions as they contain two valence electrons. This results in the $F_{pd}$ and $G_{pd}$ Slater-Condon parameters to be scaled by 95% as used in the XAS simulations. For reasons of clarity only the RIXS spectra at excitation energies a and e are shown in Figure S4, but the revealed trend is observed throughout the whole RIXS plane. Finally, note that the presented RIXS spectra in Figures S3 and S4 reflect calculations at 300 K (as the experiment) and thus appropriate Boltzmann weighted inclusion of excited states was taken into account (see next section and main text).

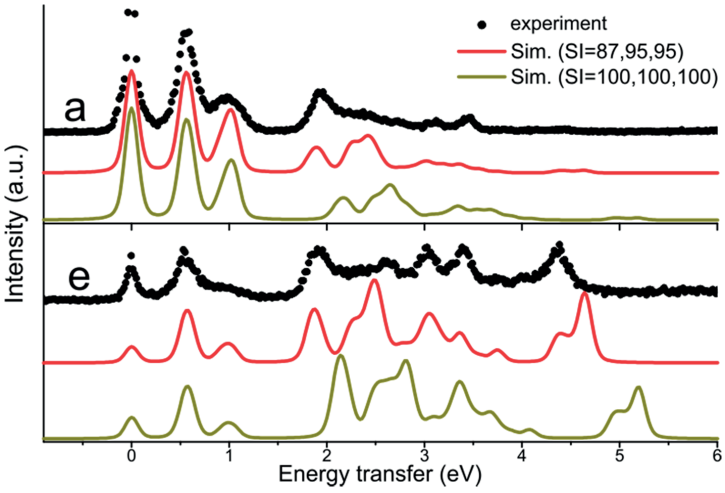


**Figure S4.** Experimental (black dotted line) and simulated (solid lines) Co 2p3d RIXS spectra at excitation energies a (top panel) and e (bottom panel). The red solid lines were performed using the exact LFM parameters given in Table 1 of the main text. The dark yellow solid lines use the same parameters, except that the scaling of the $F_{dd}$, $F_{pd}$ and $G_{pd}$ Slater parameters is now 100% of their atomic values (instead of 87, 95 and 95%, respectively).

Hence, despite the semi-empirical nature of the LFM calculations, the high resolution of the RIXS data, and the combination with the XAS data, allows the accurate (within 5% error) determination of the effective 10Dq and Slater values.

**Boltzmann weighted LFM RIXS cross sections at excitation energies b, c and e**

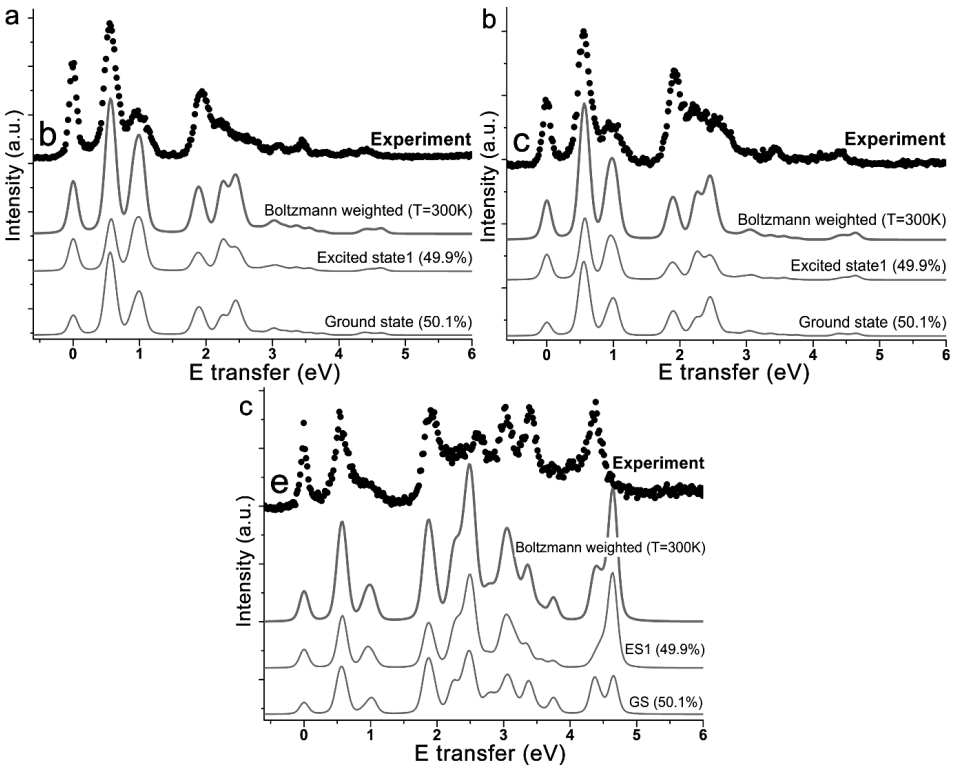


**Figure S5.** Experimental (black dots) and corresponding LFM (grey lines) RIXS spectra at excitation energies b (panel a), c (panel b) and e (panel c), respectively. The theoretical ground and the first excited state RIXS spectrum are shown, together with their Boltzmann weighted sum at 300 K (spectral weights in brackets).

**Determination of $D_{2d}$ distortion parameters from RIXS data**

Table S1 provides the LFM parameters used for the calculations given in Figure 6 of the main text.

**Table S1.** Electronic structure parameter values (in eV) used in LFM simulations of cobalt 2p3d RIXS spectra (Figure 6) in $T_d$ and $D_{2d}$ symmetries.

| | **initial states ($T_d$ /$D_{2d}$)** | **intermediate states ($T_d$ /$D_{2d}$)** | **final states ($T_d$ /$D_{2d}$)** |
|---|---|---|---|
| $F^2_{dd}$ | 8.077 | 8.628 | 8.077 |
| $F^4_{dd}$ | 5.018 | 5.365 | 5.018 |
| $F^2_{pd}$ | | 5.518 | |
| $G^1_{pd}$ | | 4.102 | |
| $G^3_{pd}$ | | 2.333 | |
| $\zeta_{3d}$ | 0.066 | 0.083 | 0.066 |
| $\zeta_{2p}$ | | 9.748 | |
| 10Dq | -0.550 / -0.540 | -0.440 / -0.430 | -0.550 / -0.540 |
| Ds | 0.000 / -0.080 | 0.000 / -0.080 | 0.000 / -0.080 |
| Dt | 0.000 / 0.005 | 0.000 / 0.005 | 0.000 / 0.005 |
| Γ (fwhm) | | 0.400 | 0.010 |
| G (fwhm) | | 0.010 | 0.010 |

The $D_{2d}$ distortion parameters Ds and Dt were obtained from a series of systematic variation tests of Ds and Dt. Figure S6(a) shows one such test series, in which simulated RIXS spectra at excitation energy a were calculated with varying Ds at Dt=0 eV. From this graph it can be seen that applying any positive or negative Ds value increases the broadening of the $^4T_2$ and $^4T_1$ peaks. Values of +/- 0.16 eV are too high in their absolute value as the splitting of the $^4T_2$ (+) or $^4T_1$ (-) peak become too large to match the experiment. Values of +/-0.08 eV show both a slight improvement in the match to the experiment, where the -0.08 eV case better matches higher energy peaks, especially in the 1.5-2.5 eV range. In combination with further tests, an additional Dt distortion of +0.005 eV gives a good match of the simulations to the experiment at excitation energy a, as shown in the solid blue line of Figure S6(b). This graph shows that only +0.005 eV gives a good relative match of the $^4T_2$ to $^4T_1$ intensity ratio at Ds = -0.08 eV and that additionally the energy positions of the peaks matches perfectly the experiment. Figure S6(a) revealed that both positive and negative Ds values, effectively shift down the $^4T_2$ peak in energy from the $T_d$ reference (Ds=0 eV), implying a positive Dt is need in any case to correct for Ds at fixed 10Dq (Figure S6(b) shows that negative Dt lowers transition energies down w.r.t. $T_d$ symmetry). From such approach it will be obvious that,

given the many spectral features observed in 2p3d RIXS it is only a few selected combinations of distortions parameters that could lead to an improvement over all RIXS spectra (at each excitation energy) as is the case for the chosen solution. Despite this careful determination of parameters we do however not claim that this a unique solution. High resolution experiments (20 meV versus 90 meV is possible recently) will enable to further improve on the current view.

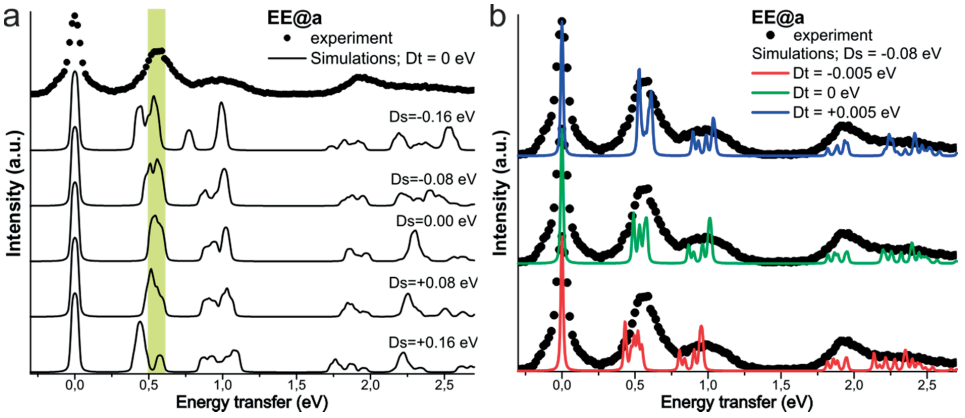


**Figure S6. (a)** Experimental (black dotted line) and simulated Co 2p3d RIXS spectra (black solid lines) at excitation energy a. For calculations, the parameters as given in Table 1 of the main text were used, but with $D_t$ fixed to 0 eV and $D_s$ varying from -0.16 to +0.16 eV in steps of 0.08 eV. (b) The same experimental RIXS spectrum as in (a) compared to calculations at fixed $D_s$ = -0.08 eV and varying $D_t$ value. At $D_t$ +0.005 eV the best match to the experiment was obtained.

Chapter 4

# In-situ 2p3d resonant inelastic X-ray scattering tracking cobalt nanoparticle reduction

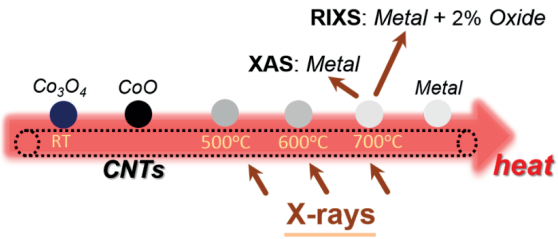


Cobalt oxide nanoparticles supported on carbon nanotubes (CNTs) during the carbon-thermal reduction were studied firstly by cobalt 2p3d resonant inelastic x-ray scattering (RIXS). The in-situ 2p X-ray absorption spectroscopy (XAS) and RIXS measurements were performed at 500°C, 600°C and 700°C, where four consistent excitations energies were used for RIXS acquisitions. After 700°C reduction, XAS spectrum shows pure cobalt metal-like shape, while RIXS clearly reveals the minority cobalt monoxide phase. The holistic fit on both XAS and RIXS data indicated the respective contributions from metal and monoxide. We show that the relative precision to determine the monoxide content changes from ~5% in XAS results to better than 2% in RIXS results, suggesting RIXS a useful tool to track the oxidation state of nanoparticles under in-situ conditions.

## 4.1. INTRODUCTION

In chemical reactions where transition metal nanoparticles play pivotal roles, it is an important goal to track the phase evolution of nanoparticles during activation and usage. In catalysis, for example, tracking chemical phase changes can be essential to unveil deactivation processes of catalysts, while quantifying the active phase can be used to understand catalytic performances.[1] A nuisance of probing minority chemical species is that they are often obscured by signal of majority phases. A minority phase in the sea of major chemical phases can, however, be a key phase, such as the catalytic active phase, that requires the effective detection of it. XAS is an element-specific and spin-selective technique, which is sensitive to the oxidation state and different chemical environments. In-situ XAS further allows the probing of phase information under relevant reaction conditions.[2-4] Due to strong multiplet effects and a small core-hole lifetime broadening,[5] 2p XAS spectra ($L_{2,3}$ edges) of transition metals exhibit rich characteristic features and high chemical sensitivities. Because the XAS edge jump is an atomic property, the XAS intensity scales linearly with the number of atoms, which has made XAS a widely applied technique to discriminate phase heterogeneities and to obtain phase concentrations by fitting procedures.[6-9] But for minority phase detection, a limitation present in 2p XAS is that signals from majority phases overwhelm details of the minority phase.[10] Although fitting procedures were used to determine the minority phase information including concentrations, we note that the overlap of spectroscopic signatures from different phases can lead to multiple interpretations. A minority phase, under such cases, can even be undetected when its signatures are hidden under those from majority phases. In this regard, high energy resolution 2p3d RIXS, which can selectively enhance spectral features from a particular phase of interest, is a complementary spectroscopic tool to 2p XAS. Being a non-linear technique w.r.t. the number of atoms adds to the possible detection of minority phases.

## 4.2. EXPERIMENT

We use $Co_3O_4$ nanoparticles supported on CNTs as model Fischer-Tropsch catalyst precursors, where we study the reduction process of $Co_3O_4$ nanoparticles. We show that 2p3d RIXS can be more useful than 2p XAS in detecting the minority species under in-situ conditions. In an ex-situ study the higher sensitivity of 2p3d RIXS over 2p XAS in detecting minority species was previously demonstrated.[10] Here we add a detailed fitting to a large dataset, acquired in-situ, to previous insights. Fitting results are used to understand the sensitivity of 2p3d RIXS on the minority oxide phase detection. Moreover, the established fitting approach, allows the quantitative description of a mixed phase system with high precision, revealing application potential in the study of active catalysts and other active materials.

The $Co_3O_4$/CNTs catalyst was prepared according to published procedures[11] with a cobalt loading of 8 wt%. The dark field transmission electron microscopy (TEM) of the fresh catalyst (Figure 1A) shows a fairly uniform nanoparticle distribution with the average particle size around 5 nm. Both X-ray powder diffraction (XRD) and cobalt 2p XAS, shown in the Supporting Information, indicate the $Co_3O_4$ phase of cobalt oxide nanoparticles before reduction.

In Fischer-Tropsch synthesis, cobalt metal is reported to be the active phase during hydrogenation of CO.[12-13] Several studies have applied in-situ TEM or XRD to examine the reduction process of carbon supported transition metal nanoparticle catalysts.[14-16] However, TEM has a limitation of probing phase information only to selected nanoparticles; XRD reveals crystalline phases only in non-quantitative ways. On the contratry, X-ray spectroscopies offer bulk phase information of nanoparticles with feasibilities to quantify phase concentrations. Here we compare differences of in-situ 2p XAS and 2p3d RIXS for revealing the relative phase composition of cobalt-based nanoparticles during reduction.

In-situ measurements were performed at BL07LSU[17] in SPring-8. The catalyst was pressed into a thin pellet and loaded on the sample holder, which was then heated in a vacuum chamber attached next to the main chamber for the sample reduction. The temperature on the sample surface was monitored by a well-calibrated pyrometer. After heating in vacuum at 500°C, 600°C and 700°C respectively, the sample was cooled down and transferred into the main chamber for spectra acquisitions. Figure 1B sketches the XAS and RIXS measurements. XAS spectra were collected by the total electron yield (TEY) mode. RIXS spectra were acquired under a 90° scattering angle in the linear horizontal (LH) scattering geometry. Detailed experimental procedures and spectra acquisitions are specified in the Supporting Information.

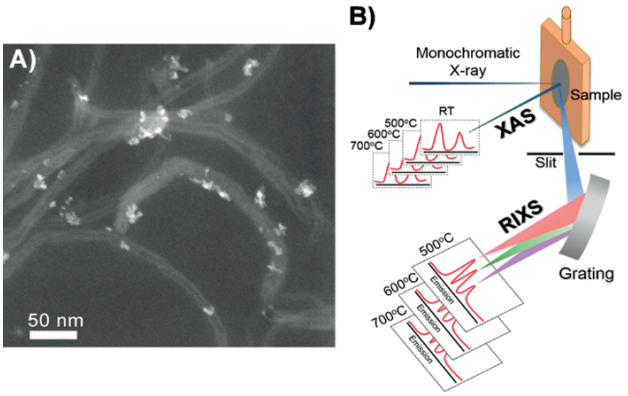


**Figure 1.** (A) Dark field TEM image of the fresh catalyst. (B) Schematic representation of XAS and RIXS measurements.

## 4.3. RESULTS AND DISCUSSION

Temperature-dependent cobalt $2p_{3/2}$ XAS spectra of the catalyst together with literature reference CoO[18] and cobalt metal[19] spectra are shown in Figure 2A. From the analysis, it is clear that CoO and cobalt metal phases co-exist in cobalt nanoparticles after reduction at 500ºC and 600ºC. No sign of the intial $Co_3O_4$ is observed after these treatments. The CoO phase concentration decreased with increasing reduction temperature, as shown by the drop of relative intensities of features at the pre-edge and shoulder. The spectrum acquired after the reduction at 700ºC shows no visible fine structures of CoO, from which it could then be erronously concluded that the fully reduced cobalt nanoparticles are present. Nevertheless, here in-situ 2p3d RIXS was carried out to further examine the phases changes and map its complementariness to 2p XAS. For RIXS, excitations were chosen at energies *a-d* as indicated in Figure 2A.

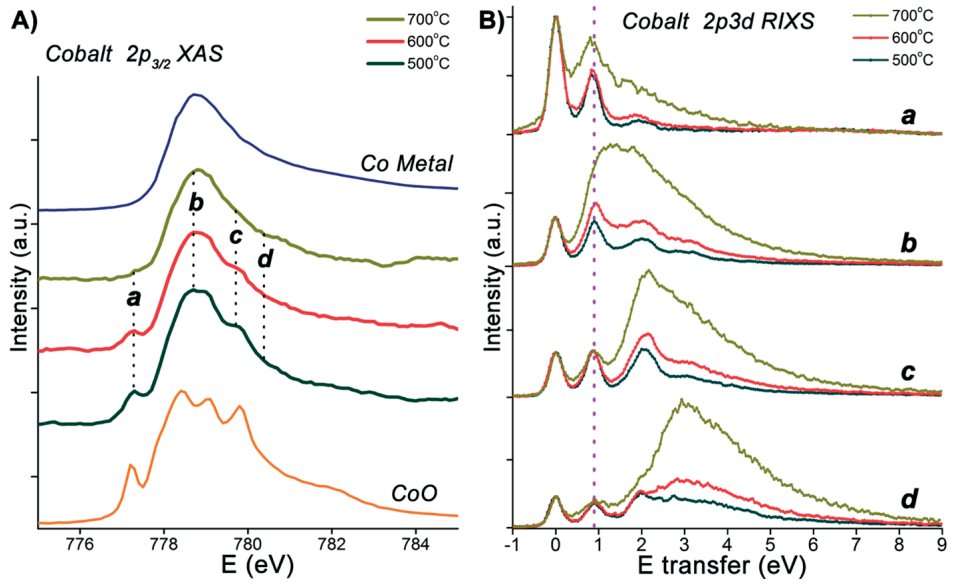


**Figure 2.** Experimental cobalt spectra of the catalyst after vacuum heating at 500ºC (dark green), 600ºC (red) and 700ºC (dark yellow): (A) $2p_{3/2}$ XAS spectra. Four dotted lines indicate excitation energies *a-d* for 2p3d RIXS. (B) 2p3d RIXS spectra. The purple dotted line indicates the d-d excitation from CoO. In (A), the literature reference spectra of Co and CoO[18-19] are plotted for comparison.

2p3d RIXS spectra of metal oxides are composed of the zero energy transfer peak that corresponds to the elastic scattering, and positive energy transfer features corresponding to phonon, magnon, d-

d and charge transfer excitations.[20-21] Phonon and magnon excitations constitute low energy (<0.1 eV) features, while d-d excitations occur at the fixed energy transfer corresponding to energy differences w.r.t the ground state irrespective of incident X-ray energies. The charge transfer excitations in a divalent metal oxide, such as CoO, have little intensity and are often shaded by d-d features unless excitation energies at charge transfer satellites in 2p XAS are chosen.[18, 22] For metals, the 2p3d RIXS measures a fixed X-ray emission by transition from delocalised states to the 2p core hole that has energy transfer from the elastic line linearly dependent on the incident X-ray energies, and is described as fluorescence (FL).[23] Here the 2p3d RIXS signals originated from CoO or cobalt metal are referred to as 'CoO RIXS' and 'Co metal FL' respectively.

Figure 2B shows the corresponding temperature dependent 2p3d RIXS spectra. Datasets from the same excitation energy are normalized to the elastic peak. The increase of the pure metal concentration is most directly observed from spectra acquired at energy *d*, since the metal FL peak around 3 eV separates further from CoO characteristic d-d peaks around 0.9 eV and 2.1 eV.[18, 22] In the current reduction steps, no new phases other than the CoO and cobalt metal, such as cobalt carbides, were found, consistent with previously reported in-situ XRD results.[11, 15] Interestingly, the d-d peak of CoO around 0.9 eV in datasets of 700°C from excitation energies *a*, *c* and *d*, unequivocally indicate the partially reduced nature of cobalt nanoparticles, contrary to the possible conclusion drawn from XAS. We note that the probing depth of TEY XAS at the cobalt $2p_{3/2}$ edge is ~5 nm;[24] while the RIXS can detect photons emitted from several hundreds of nanometers underneath the sample surface.[25] Here, however, the applied heating methods (see the Supporting Information) should induce the homogenous reduction for the whole sample, and the ~5 nm (even smaller after reduction[11]) cobalt nanoparticles are fully probed by both techniques, but with different sensitivities. In 2p XAS, spectral features of the minority CoO phase are shaded by that of the majority metal phase. Whereas in 2p3d RIXS, d-d peaks of the CoO RIXS are dominantly enhanced at the excitation energy ***a*** and separated from the metal FL when excitations move to higher energies, although at the metal resonance (energy ***b***), oxide features are hidden under the metal FL. The selective resonant enhancements in RIXS enable features of the minority CoO phase to be clearly visible.

To obtain phase concentrations and to further explore the sensitivity of 2p3d RIXS for revealing the minority CoO phase, fitting procedures[26-27] (details specified in the Supporting Information) were introduced for both XAS and RIXS spectra. Figure 3 shows the fitted spectra along with the corresponding experimental data, and spectral components used for fitting. Temperature dependent 2p XAS spectra (upper panel) were fitted holistically by using literature CoO[18] and cobalt metal[19] spectra as references. The fitted spectra well matched with the corresponding experimental results. Concentrations of the CoO phase obtained from XAS fitting are listed in Table 1 (second column).

Note that although fitting results indicate the existence of a CoO phase after the reduction at 700ºC, the 4.6% uncertainty with respect to a 5.5% average value implies the inadequacy of 2p XAS alone for revealing precise information of this minority phase. In Figure S3 this is further elaborated upon, by showing a series of cobalt 2p XAS spectra, consisting of small contributions of CoO XAS spectra added to pure Co metal XAS spectra. For CoO contents <10% the obtained high spectral similarities between them explain the large uncertainty in such fitting results.

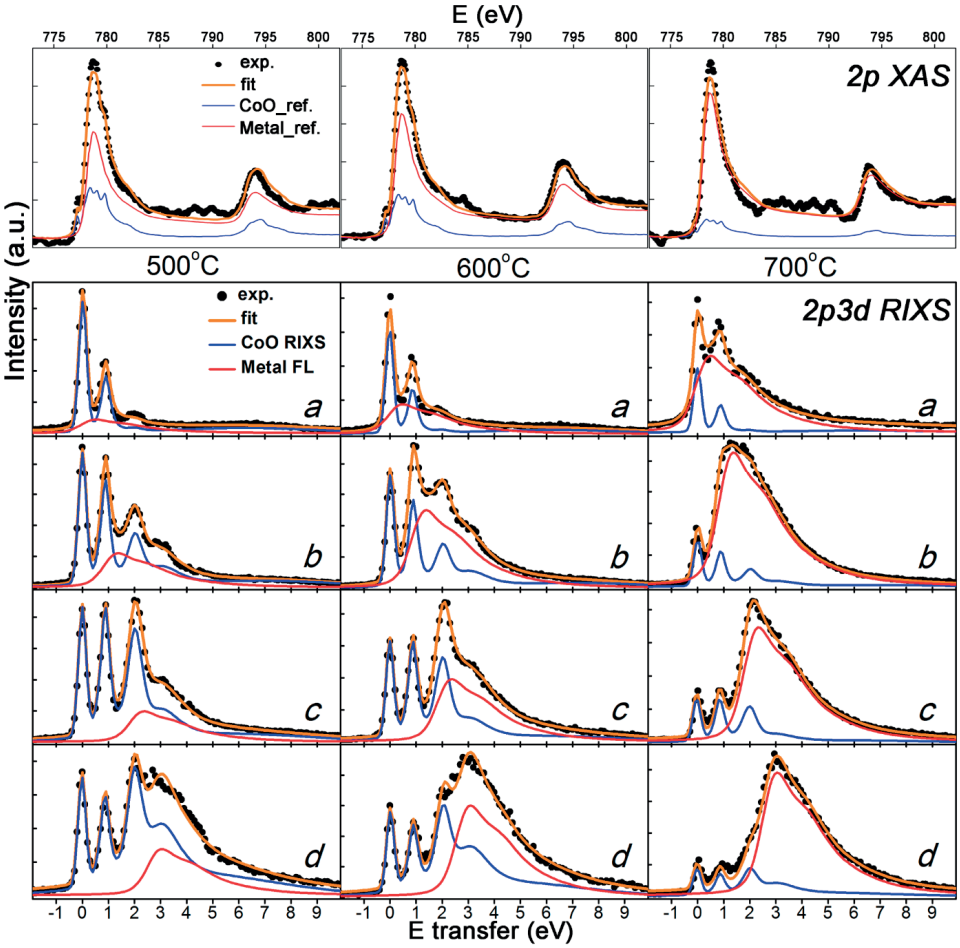


**Figure 3.** Fit (orange line) and experimental (black dot) cobalt 2p XAS (upper panel) and 2p3d RIXS (lower panel) spectra. Datasets of the same temperature are in the same column. CoO (blue line) and cobalt metal (red line) references used for fitting 2p XAS are literature reference spectra.[18-19] In 2p3d RIXS, the CoO RIXS (blue line) and metal FL (red line) contributions are shown.

The twelve 2p3d RIXS spectra, measured at three different temperatures, were also fitted holistically by decomposing them into CoO RIXS and Co metal FL, as shown in the lower panel of Figure 3, where the theoretical bases for the decomposition are stated in the Supporting Information. Here, literature references were not used for fitting since the intensity of RIXS features can be influenced by different sample surface roughness and/or experimental resolutions. Spectra acquired during different experiments should therefore not be directly compared for quantitative purposes. The decomposed CoO RIXS spectra are compared with literature references[18] in Figure S4, and energy differences of the decomposed metal FL peaks are discussed in Figure S5,[28] which essentially confirm the solidity of current decomposition-fitting results. Such RIXS fitting results are quantitatively described in the third column of Table 1 by the CoO spectral weight. The quantification procedure was based on equations (1) and (2) as stated in the Supporting Information, in which the intensity ratios between CoO RIXS and metal FL were corrected by the corresponding X-ray absorption cross section, to account for the photon-in and photon-out process of RIXS. In contrast to XAS, RIXS quantifications contain an extra sensitivity factor related to the difference of the Co/CoO spectral intensity yield as stated by equation (3) in the Supporting Information. This sensitivity factor is given by the relative (integrated) decay strength of CoO RIXS compared with Co metal fluorescence, which determines the capability of 2p3d RIXS for revealing minority CoO phase. Here the sensitivity factor was obtained with the value 5.2 ± 2.8 by correlating XAS and RIXS fitting results of the 500°C and 600°C data.

**Table 1.** 2p XAS and 2p3d RIXS derived percentages of the CoO phase in Co nanoparticles during the three reduction steps.

| Temperature (°C) | CoO concentration (%) from 2p XAS fit | CoO spectral weight (%) from 2p3d RIXS fit | CoO concentration (%) from 2p3d RIXS fit |
|---|---|---|---|
| 500 | 18.4 ± 6.1 | 56.9 ± 2.5 | 20.9 ± 1.7 |
| 600 | 14.2 ± 6.0 | 33.1 ± 1.3 | 9.0 ± 0.5 |
| 700 | 5.5 ± 4.6 | 10.7 ± 0.8 | 2.3 ± 0.2 |

The sensitivity factor implies that the CoO RIXS is ~5 times stronger than the Co metal fluorescence. Note that the lifetime of a state is given by the integrated Auger decay because Auger constitutes more than 99% of the decay. The lifetime broadening of Co metal and CoO are not accurately known. It is often assumed that the lifetime is a property of the core hole, but just as the non-radiative decay is inequivalent also the radiative decay can be inequivalent. The approximate factor of 5 should thus be understood as the ratio between the CoO (RIXS/Auger) ratio and the Co (FL/Auger) ratio. Assuming that the lifetime is the same, the factor of 5 turns into a direct ratio of the CoO RIXS versus Co FL. Note that if the radiative decay is relatively stronger for CoO, the

non-radiative decay should be relatively stronger for Co metal, but now the difference is between 95% and 99% instead of 1% and 5%, so this difference is likely undetectable. A full study of all radiative and non-radiative decay channels for CoO and Co metal would be interesting for a fundamental knowledge of the creation and decay of 2p core holes in oxides, respectively, metals.

The omission of combining the 700ºC data is due to the large uncertainty in the corresponding XAS fitting result that yields statistically meaningless values. This approach holds because here the probed phase information from XAS and RIXS is directly comparable. The lack of adequate temperature dependent datasets for combination renders the result with relatively lower precision. Thus, here the sensitivity factor was approximated to be 5, by which the converted CoO concentrations are shown in the fourth column of Table 1.

## 4.4. CONCLUSION

It is clear that fitting results from 2p3d RIXS spectra are more precise than those from 2p XAS. This is due to the well-resolved characteristic features in RIXS that constrained the solution space in the fitting procedures. Furthermore, the precision of CoO phase concentrations by RIXS fitting procedures is also influenced by the precision of the sensitivity ratio obtained. The obtained value, although approximate in nature, suggests that 2p3d RIXS is feasible to probe the minority CoO phase with higher intrinsic sensitivity in RIXS than the metallic phase. The fact that 2p3d RIXS (1) has varied sensitivities for different phases and (2) can selectively enhance features of a certain phase via tunable excitations on its resonances indeed exhibits its advantage over 2p XAS for studying minority phases. Moreover, TEY 2p XAS is limited by the probing depth and total fluorescence yield 2p XAS may suffer from non-linearly distorted spectral shapes[29] that complicate theoretical interpretations. By comparison, 2p3d RIXS can detect a bulk phase buried under the surface, and high resolution spectral features allow more accurate phase determination from theoretical analyses than 2p XAS.[30] Finally, this is the first approach in which multiple chemical phases in an in-situ 2p3d RIXS experiment are decomposed to contributions from individual phases as to quantify the corresponding concentrations.

## ACKNOWLEDGMENTS

The synchrotron radiation experiments were performed at the HORNET endstation of BL07LSU of SPring-8 with the approval of the Japan Synchrotron Radiation Research Institute

(JASRI) (Proposal No. 2013B7458, 2014A7470, 2014A7468). This work was financially supported by the China Scholarship Council and the ERC advanced grant XRAYonACTIVE, number 340279. We thank Yitao Cui, Jun Miyawaki, Yoshihisa Harada in BL07LSU, SPring-8 for experimental assistances. We thank Mario Ulises Delgado-Jaime for the help on data analysis; Rupan Wang, Matti van Schooneveld and Frank de Groot, for the useful discussions. The sample was offered by Thomas O. Eschemann and Krijn de Jong in Utrecht University.

## Supporting Information available in Appendix 4

## REFERENCES


(1) Hayakawa, H.; Tanaka, H.; Fujimoto, K. *Appl. Catal., A* **2006**, *310*, 24-30.

(2) Li, S. Z.; Meitzner, G. D.; Iglesia, E. *J. Phys. Chem. B* **2001**, *105*, 5743-5750.

(3) Takamatsu, D.; Koyama, Y.; Orikasa, Y.; Mori, S.; Nakatsutsumi, T.; Hirano, T.; Tanida, H.; Arai, H.; Uchimoto, Y.; Ogumi, Z. *Angew. Chem., Int. Ed*. **2012**, *51*, 11597-11601.

(4) Bordiga, S.; Groppo, E.; Agostini, G.; van Bokhoven, J. A.; Lamberti, C. *Chem. Rev.* **2013**, *113*, 1736-1850.

(5) de Groot, F. M. F. *Coord. Chem. Rev.* **2005**, *249*, 31-63.

(6) Tuxen, A.; Carenco, S.; Chintapalli, M.; Chuang, C. H.; Escudero, C.; Pach, E.; Jiang, P.; Borondics, F.; Beberwyck, B.; Alivisatos, A. P.; Thornton, G.; Pong, W. F.; Guo, J. H.; Perez, R.; Besenbacher, F.; Salmeron, M. *J. Am. Chem. Soc.* **2013**, *135*, 2273-2278.

(7) Morales, F.; de Groot, F. M. F.; Glatzel, P.; Kleimenov, E.; Bluhm, H.; Havecker, M.; Knop-Gericke, A.; Weckhuysen, B. M. *J. Phys. Chem. B* **2004**, *108*, 16201-16207.

(8) Ghiasi, M.; Delgado-Jaime, M. U.; Malekzadeh, A.; Wang, R. P.; Miedema, P. S.; Beye, M.; de Groott, F. M. F. *J. Phys. Chem. C* **2016**, *120*, 8167-8174.

(9) Lee, H. J.; Kim, G.; Kim, D. H.; Kang, J. S.; Zhang, C. L.; Cheong, S. W.; Shim, J. H.; Lee, S.; Lee, H.; Kim, J. Y.; Kim, B. H.; Min, B. I. *J. Phys.Condens. Matter* **2008**, *20*, 295203.

(10) van Schooneveld, M. M.; Suljoti, E.; Campos-Cuerva, C.; Gosselink, R. W.; van der Eerden, A. M. J.; Schlappa, J.; Zhou, K. J. J.; Monney, C.; Schmitt, T.; de Groott, F. M. F. *J. Phys. Chem. Lett.* **2013**, *4*, 1161-1166.

(11) Eschemann, T. O.; Lamme, W. S.; Manchester, R. L.; Parmentier, T. E.; Cognigni, A.; Ronning, M.; de Jong, K. P. *J. Catal.* **2015**, *328*, 130-138.

(12) Cats, K. H.; Gonzalez-Jimenez, I. D.; Liu, Y. J.; Nelson, J.; van Campen, D.; Meirer, F.; van der Eerden, A. M. J.; de Groot, F. M. F.; Andrews, J. C.; Weckhuysen, B. M. *Chem. Commun.* **2013**, *49*, 4622-4624.

(13) Tsakoumis, N. E.; Dehghan, R.; Johnsen, R. E.; Voronov, A.; van Beek, W.; Walmsley, J. C.; Borg, O.; Rytter, E.; Chen, D.; Ronning, M.; Holmen, A. *Catal. Today* **2013**, *205*, 86-93.

(14) Chen, W.; Pan, X. L.; Willinger, M. G.; Su, D. S.; Bao, X. H. *J. Am. Chem. Soc.* **2006**, *128*, 3136-3137.

(15) Xiong, H. F.; Moyo, M.; Rayner, M. K.; Jewell, L. L.; Billing, D. G.; Coville, N. J. *ChemCatChem* **2010**, *2*, 514-518.

(16) Xiong, H. F.; Motchelaho, M. A. M.; Moyo, M.; Jewell, L. L.; Coville, N. J. *J. Catal.* **2011**, *278*, 26-40.

(17) Harada, Y.; Kobayashi, M.; Niwa, H.; Senba, Y.; Ohashi, H.; Tokushima, T.; Horikawa, Y.; Shin, S.; Oshima, M. *Rev. Sci. Instrum.* **2012**, *83*, 013116.

(18) van Schooneveld, M. M.; Kurian, R.; Juhin, A.; Zhou, K. J.; Schlappa, J.; Strocov, V. N.; Schmitt, T.; de Groot, F. M. F. *J. Phys. Chem. C* **2012**, *116*, 15218-15230.

(19) Chen, C. T.; Idzerda, Y. U.; Lin, H. J.; Smith, N. V.; Meigs, G.; Chaban, E.; Ho, G. H.; Pellegrin, E.; Sette, F. *Phys. Rev. Lett.* **1995**, *75*, 152-155.

(20) Kotani, A.; Shin, S. *Rev. Mod. Phys.* **2001**, *73*, 203-246.

(21) Ament, L. J. P.; van Veenendaal, M.; Devereaux, T. P.; Hill, J. P.; van den Brink, J. *Rev. Mod. Phys.* **2011**, *83*, 705-767.

(22) Magnuson, M.; Butorin, S. M.; Guo, J. H.; Nordgren, J. *Phys. Rev. B* **2002**, *65*, 205106.

(23) van Schooneveld, M. M.; Juhin, A.; Campos-Cuerva, C.; Schmitt, T.; de Groot, F. M. F. *J. Phys. Chem. C* **2013**, *117*, 14398-14407.

(24) Seah, M. P.; Dench, W. A. *Surf. Interface Anal.* **1979**, *1*, 2-11.

(25) Henke, B. L.; Gullikson, E. M.; Davis, J. C. *At. Data Nucl. Data Tables* **1993**, *54*, 181-342.

(26) Delgado-Jaime, M. U.; Kennepohl, P. *J. Synchrot. Radiat.* **2010**, *17*, 119-128.

(27) Delgado-Jaime, M. U.; Mewis, C. P.; Kennepohl, P. *J. Synchrot. Radiat.* **2010**, *17*, 132-137.

(28) de Groot, F. M. F.; Pizzini, S.; Fontaine, A.; Hamalainen, K.; Kao, C. C.; Hastings, J. B. *Phys. Rev. B* **1995**, *51*, 1045-1052.

(29) van Schooneveld, M. M.; Gosselink, R. W.; Eggenhuisen, T. M.; Al Samarai, M.; Monney, C.; Zhou, K. J. J.; Schmitt, T.; de Groot, F. M. F. *Angew. Chem., Int. Ed*. **2013**, *52*, 1170-1174.

(30) de Groot, F. M. F.; Arrio, M. A.; Sainctavit, P.; Cartier, C.; Chen, C. T. *Solid State Commun.* **1994**, *92*, 991-995.

# Appendix 4

## Contents

Synthesis of the CNTs supported Co FT catalyst.

XRD of the fresh $Co_3O_4$/CNTs catalyst.

In-situ 2pXAS & 2p3d RIXS measurements.

In-situ Co 2p XAS of Co3O4/CNTs catalyst during reduction steps.

Co 2p XAS of CoO and Co metal mixture with <10% CoO phase concentration.

The holistic fit of 2p XAS.

The holistic decomposition-fit of 2p3d RIXS.

Combination of 2p XAS and 2p3d RIXS fitted results.

Comparison of decompose-fitted CoO RIXS with literature reference CoO RIXS.

Decompose-fitted Co metal fluorescence four excitation energies.

**Synthesis of the CNTs supported Co FT catalyst**

The catalyst was prepared according to published procedures.[11] Commercially purchased multiwalled carbon nanotubes (CNTs, Baytubes C 150 HP, Bayer Materials Science) without further processing were used as support material. The untreated CNTs were dried in vacuum and then loaded by incipient wetness impregnation by using a 1.5M cobalt nitrate hexahydrate ($Co(NO)_3 \cdot 6H_2O$, p.a., Acros) in ethanol (Interchema, >99%). The obtained materials were dried in a static oven at 333K in air for 10 hours. The materials were then calcined in a reactor at 250°C for 4 hours under a flow of nitrogen gas to decompose the cobalt precursor. The metal loading was calculated assuming the Co to be fully oxidized into the form of $Co_3O_4$, and it was calculated from the mass of solution added during the impregnation of the catalyst.

**XRD of the fresh $Co_3O_4$/CNTs catalyst**

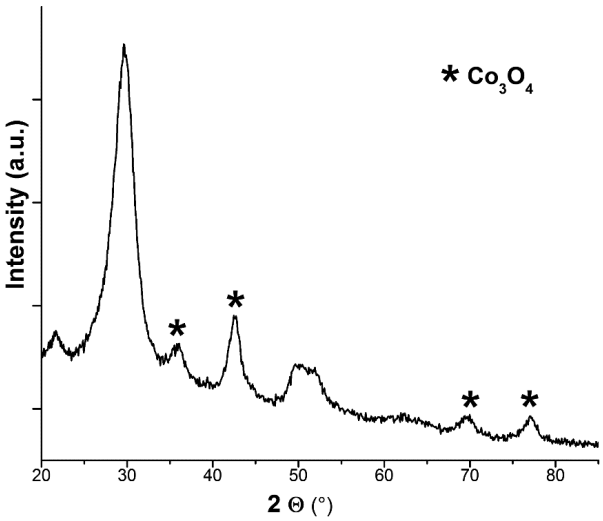


**Figure S1.** X-ray Diffraction of the fresh catalyst

The XRD data were collected by using a Bruker D2 Phaser with a Co K α (λ=1.789 Å) source. The diffraction peaks around 30° and 50° originate from the graphitic CNTs.

**In-situ 2pXAS & 2p3d RIXS measurements**

*In-situ reduction in synchrotron:* the vacuum reduction of the catalyst were performed at the beamline 07LSU, in SPring-8 synchrotron, Japan. The granule-shape catalysts were grinded into powder and pressed into a round pellet with 1 mm thickness and 7 mm diameter. The pellet was held by an oxygen free copper sample holder and fixed by a cap on top of it. A round hole with 2 mm diameter in the middle of the cap allows the X-ray shinning on the sample. The sample holder was transferred from the load lock chamber into the so-called preparation chamber which is connected next to the main chamber. The pressure inside the preparation chamber before and after heating the sample was pumped down to ~$2x10^{-8}$ mbar. The vacuum reduction was performed in the preparation chamber by electron bombardment using a filament. The heating was performed from the rear side of the sample holder, which transferred the heat to the whole sample pellet in order to achieve the homogenous sample heating. The temperature on the sample surface was measured by a pyrometer that was calibrated by using the thermocouple in the lab prior to the synchrotron in-situ experiment. During the vacuum heating, 500°C, 600°C and 700°C on the sample surface was reached and kept for 1 hour respectively. After each heating, the sample was cooled down naturally in the preparation chamber and then transferred into the main chamber for both 2p XAS and 2p3d RIXS measurements. The pressure inside the main chamber was pumped to be ~$2x10^{-8}$ mbar.

*2p XAS & 2p3d RIXS data acquisition:* the temperature dependent Co 2p XAS were acquired by the total electron yield (TEY) mode by measuring the drain current of the sample. The temperature dependent spectra including the fresh sample spectrum acquired at room temperature (RT) before the vacuum heating are shown in Figure S2. Each spectrum was sampled with 10 points $eV^{-1}$. The energy of the spectra were calibrated by comparing with the reference spectra of CoO single crystal sample and compared with the literature CoO XAS spectra.[18] The RIXS data were collected by the high energy resolution spectrometer at BL07LSU.[17] The scattering angle between the incoming and outgoing light vectors was kept to be 90°. The linear horizontal (LH) polarized incident beam with the 45° incident angle to the sample surface was used for both XAS and RIXS data recordings. The RIXS spectrometer as optimized by measuring the elastic scattering peaks at 780 eV. The elastic peaks were fitted with Gaussian functions and the emission energy was calibrated by the peak position of the elastic scatterings at 770 and 780 eV. The RIXS energy resolution of the elastic peak at 780 eV was calibrated to be 235 meV. The presented RIXS spectra in Figure 1 was summed by 2-4 separated measured RIXS spectra (60 minutes each). The four excitation energies shown as a-d in Figure 2c are 777.3 eV, 778.7 eV, 779.7eV and 780.4eV.

**In-situ Co 2p XAS of $Co_3O_4$/CNTs catalyst during reduction steps**

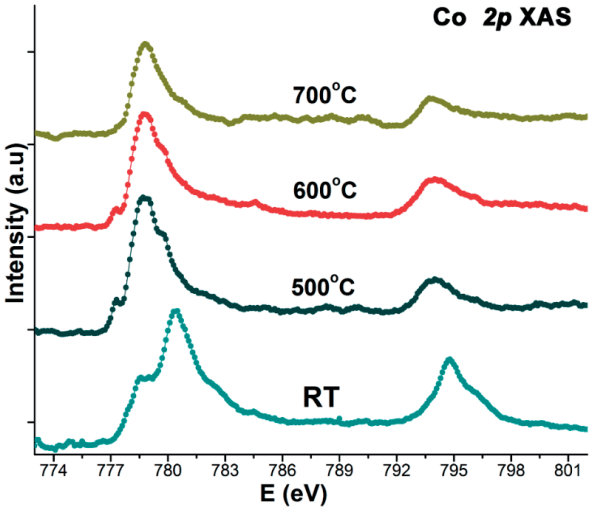


**Figure S2.** Temperature dependent Co 2p XAS (TEY) at room temperature (RT), 500ºC, 600ºC, and 700ºC.

**Co 2p XAS of CoO and Co metal mixture with <10% CoO phase concentration**

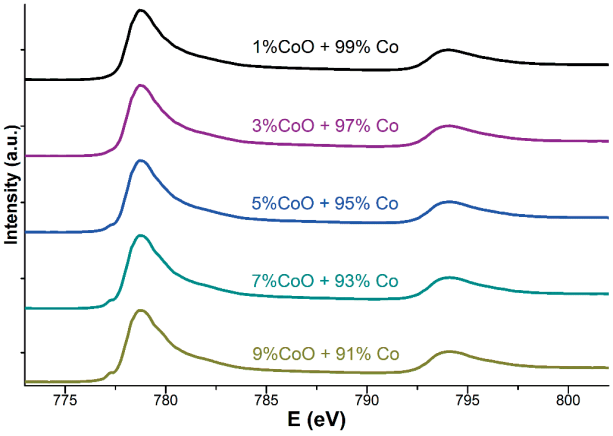


**Figure S3**. Simulated cobalt 2p XAS spectra with varied CoO to cobalt metal spectral weight ratio as shown in each spectra. Literature CoO and Co metal spectra are used as references.

**The holistic fit of 2p XAS**

The principle of the holistic fit was described in the literature.[26] Here the 2p XAS at the 500ºC, 600ºC and 700ºC were fitted simultaneously with the CoO and Co metal 2p XAS obtained from literatures as stated in the main manuscript. In the fit model, a background function[27] was included to fit both the raw experimental spectra and the two literature reference spectra. This background function is an ensemble of piecewise manner polynomial functions, and which was used to fit quasilinear regions in 2p XAS spectra. The reference spectra after background subtraction were normalized to the intensity of post-$L_2$ edge (~803 eV) as presented in Figure 2b and 2c. For the two reference spectra used (between 773 and 803 eV), the $L_{2,3}$ continuum edge jumps with the 2:1 ratio were included for the Co metal reference spectrum (see the literature reference[19] in the manuscript); while only the $L_3$ continuum edge jump was set for CoO reference spectrum. Here, the different edge jumps were set due to the difference of electron localization in oxides and in metal. Note that in the fits, edge jump positions were allowed to float, and which were also linked with the above mentioned background functions. The scaling factors and the energy shifts between the reference spectra and experimental data were also set in the fit model, which together with other parameters were fitted simultaneously. The model was fitted by using the BlueprintXAS[26] to produce multiple fits, and a total of 24 good fits were obtained and analyzed. From the fits, scaling factors with uncertainties were used as the quantification results and presented in Table 1.

**The holistic decomposition-fit of 2p3d RIXS**

The twelve 2p3d RIXS datasets were fitted by using a separate model without including reference spectra. The twelve datasets were merged into one dataset that allows the decomposition and fits to be performed holistically. Here, each experimental Co 2p3d RIXS spectra was composed of 'artificial' CoO RIXS and Co FL. All individual peaks that used to comprise the CoO RIXS and Co FL are the pseudo-Voigt peaks.

For the CoO RIXS, it is composed of an elastic peak, d-d peaks and a separate peak that simulates the charge-transfer (CT) effects. The relative energy position of d-d peaks were set to be constant in all the datasets, while energy positions of the CT peak were only fixed for datasets acquired at the same excitation energy. Similarly, all the elastic and d-d peaks were forced to have the same shape (the Lorentzian : Gaussian ratio and the broadening of full width at half maximum), while CT peak is only set to be with the same shape for datasets belonging to the same excitation energy, and which was allowed to float in the model. Furthermore, the relative intensities of all CoO RIXS features were kept constant for datasets collected at the same excitation energies, but this varies for datasets belonging to different excitation energies. The decompose-fitted CoO RIXS was compared

with the literature[18] reference CoO (obtained with different energy resolutions), as shown in Figure S4. Apart from the excitation energy *a*, other excitation energies chosen in these two work were not consistent, hence we could only compare RIXS slices obtained by close excitation energies, as noted in the figure legends. The RIXS slices were normalized to the first d-d peak, since the elastic peak intensity for data from different measurements is not directly comparable. The comparison of spectra at excitation energy *d* is not shown in Figure S4, since no reference spectra acquired at close excitation energies is available.

For the Co FL, in this model, it was assumed to be with the same shape in all twelve datasets. Because in fluorescence the excitation is decoupled from the decay, the metal FL can be considered as the convolution of XAS with the x-ray emission spectra above the edge. When the excitation energy is chosen above the edge the XAS spectral shape is constant (or slowly varying in intensity) implying that the Co FL is also constant in shape. At the absorption edge the shape of the XAS spectrum slightly modifies the Co FL, where a peak maximum makes the shape sharper and a valley makes the shape slightly broader [see literature reference,[28] cf figure 1]. The fixed shape FL envelope as a whole consists of three peaks, whose relative energy positions, intensity ratios and shapes are set to be constant. The energy shifts between FL envelopes, belonging to datasets acquired at excitation energies b-d, were set to the corresponding shifts of excitations. However, for the FL envelope that acquired at the excitation energy a, its energy position was allowed to float since the fixed emission breaks down for this excitation energy. (Here, we need to better interpret our assumption). The decompose-fitted Co FL was shown in Figure S5. Decompose-fitted results showed that the energy difference between the FL maxima from datasets acquired at excitation energies a and b was around 0.8 eV. Whereas the difference between excitation energies a and b is 1.4 eV. The discrepancy is due to that the X-ray Raman was measured when choosing the excitation energy a; while at excitation energies b-d, the 2p3d RIXS of Co metal were pure FL with fixed emission energies.

Initially, the total CoO RIXS intensity (integrated area) was parameterized as a function of the total Co FL intensity, shown as the equation (1):

$$r_{ij} = \frac{I_{FL,ij}}{I_{RIXS,ij}} \tag{1}$$

where the parameter $r_{ij}$ is dependent of the temperature *i* and the excitation energy *j*.

Since RIXS is a 'photon-in photon-out' technique, the $r_{ij}$ was firstly normalized by the absorption cross section ratio of CoO ($\sigma_{CoO,j}$) to Co metal ($\sigma_{Co,j}$), as shown in the equation (2). Here, this ratio was obtained from the normalized reference spectra shown in Figure 2(A). The new parameter $R_i$

in this model is only dependent of temperature and which directly implies the ratio of spectra contribution by Co metal to CoO.

$$R_i = \frac{I_{FL,ij}}{I_{RIXS,ij}} \times \frac{\sigma_{CoO,j}}{\sigma_{Co,j}} \quad (2)$$

Similar to the XAS fit, all parameters set in this decomposition-fit model were fitted simultaneously by the BlueprintXAS. A total of 39 good fits were obtained and analyzed. The results of are chosen to shown as the CoO contribution in Table 1 in the main manuscript.

**Combination of 2p XAS and 2p3d RIXS fitted results**

In principle, RIXS is a more bulk sensitive technique than the TEY XAS since the attenuation depth of photon is much larger than electrons. Considering the 5 nm (even smaller after the reduction[11]) Co nanoparticles in the current studied materials, the TEY XAS is almost equivalent to the RIXS with respect to the detection depth. On the other hand, the XAS fitted results directly represent the percentage of the CoO and Co metal in the Co nanoparticles; whereas the RIXS fitted results only represent the spectra intensity contribution from the either phase. To directly compare the XAS and RIXS fitted results, an extra factor that represent the signal yields ratio of CoO and Co metal phase for the respective RIXS and FL is further needed. With this factor, percentages of the CoO phase can be extracted from the RIXS fitted results, as shown in equation (3). The signal yield is an intrinsic property of materials and this ratio is therefore a constant (*C*) between Co and CoO. In equation (3), the *C* represents the ratio of Co FL to CoO RIXS yield by the same unit of respective phases. Here, the constant *C* in equation (3) is the sensitivity factor discussed in the main manuscript.

$$CoO\% = \frac{1}{R_i * C + 1} * 100 \quad (3)$$

In current work, we compared the 2p XAS and 2p3d RIXS fitted results at 500ºC and 600ºC. In total, the 24*39 combinations at each temperature were used. We ignored the 2p XAS fitted results of 700ºC, because the large uncertainty rendered a larger uncertainty without statistical meanings.

**Comparison of decompose-fitted CoO RIXS with literature reference CoO RIXS**

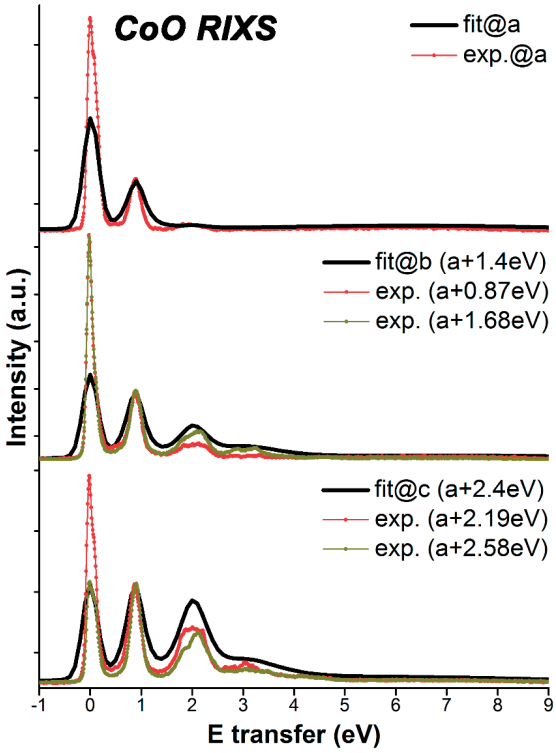


**Figure S4.** Decompose-fitted CoO RIXS and literature reference[18] CoO RIXS: (Top) Both spectra acquired at the excitation energy a. (Middle) Decompose-fitted spectra acquired with the excitation energy b, which is 1.4 eV higher than the excitation energy a; literature reference spectra acquired with excitation energies that are respectively 0.87 eV and 1.68 eV higher than the excitation energy a. (Bottom) Decompose-fitted spectra acquired with the excitation energy c, which is 2.4 eV higher than the excitation energy a; literature reference spectra acquired with excitation energies that are respectively 2.19 eV and 2.58 eV higher than the excitation energy a.

**Decompose-fitted Co metal fluorescence four excitation energies**

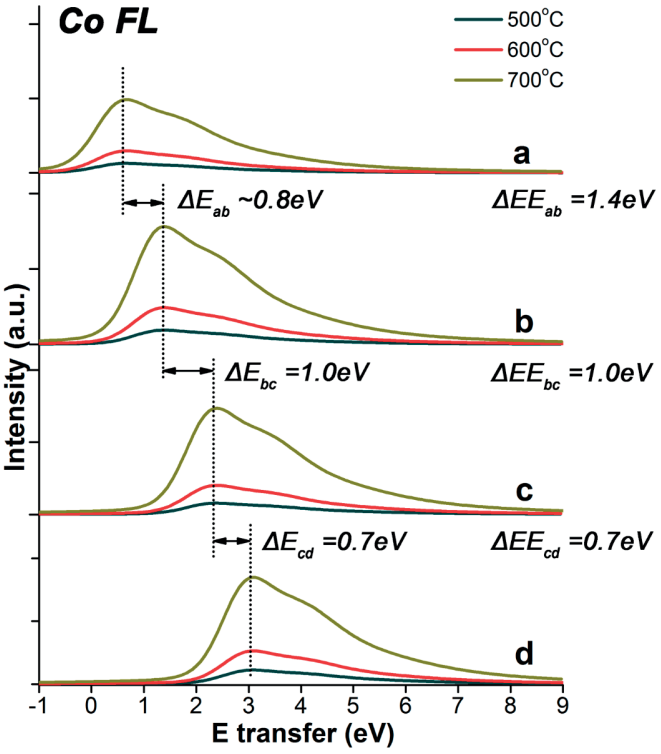


**Figure S5**. The decompose-fitted Co metal fluorescence from datasets acquired at excitation energies a-d, of 500ºC (dark green), 600ºC (red) and 700ºC (dark yellow). The delta E represents the energy difference between the fluorescence maxima. The delta EE is the difference of excitation energies.

Chapter 5

# The difference between electron yield and fluorescence yield X-ray magnetic circular dichroism derived sum rule values

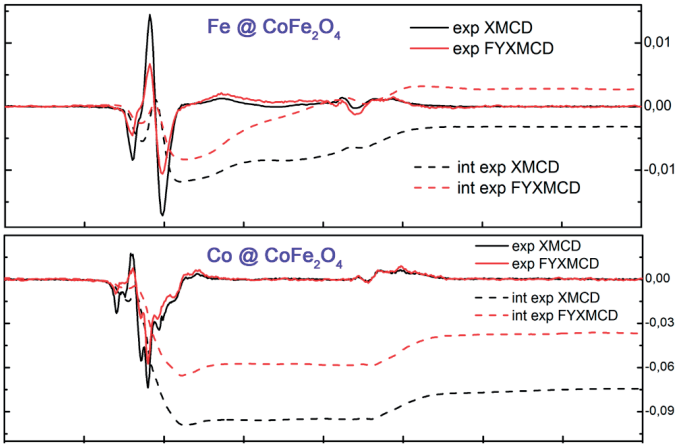


The quantitative analysis of 3d transition metal $L_{2,3}$ edge X-ray magnetic circular dichroism (XMCD) spectra and the related sum rules are compared for measurements with electron yield and fluorescence yield detection. Multiplet simulations on the $Mn^{2+}$, $Fe^{2+}$, $Co^{2+}$ and $Ni^{2+}$ ions show that the fluorescence yield detected sum rule derived expectation values of $L_z$ and $S_z$ show noticeable deviations and detection angle dependence. We show that small deviations of the polarization dependent fluorescent decay values lead to significant deviations in the $L_z$ and $S_z$ sum rule values. Fe and Co experimental XMCD spectra of a supported 10 nm $CoFe_2O_4$ thin film are measured simultaneously by both electron and fluorescence yield. The deviations shown in the experimental data are well explained by the simulations and are shown to mainly depend on the polarization dependent total decay. We conclude that fluorescence yield detected X-ray magnetic circular dichroism is unsuitable for quantitative analysis of the $L_z$ and $S_z$ sum rule values.

## 5.1. INTRODUCTION

XMCD is an experimental tool that probes the difference between X-ray absorption spectra (XAS) obtained by using left- and right-circularly polarized X-rays. By combining abilities of the X-ray spectroscopy with the magnetometry, XMCD offers the advantage of element specificity to study electronic and magnetic structures of magnetic materials or the magnetic components in a complex with magnetic heterogeneities.[1-3] For example, Funk *et al.*[2] applied XMCD to investigate the paramagnetic Ni center in the active site of acetyl-CoA decarboxylase/synthase complex. The optical sum rules[4-6] state that integrals of the XMCD spectrum can be related to ground state expectation values of the spin ($S_z$) and the orbital ($L_z$) angular momentum. This makes XMCD more efficacious as a quantitative analysis tool to study magnetic properties. For 3d transition metals, the XMCD at their $L_{2,3}$ edges is significantly stronger than at their K edges. However, $L_{2,3}$ edges of transition metals lie in the soft X-ray range, in which transmission measurements of absorption spectra are difficult due to the short X-ray penetration length of ~20 nm at the L edge maximum.[6-7] In most experiments, transition metal L edge XAS are obtained by yield methods that measure the flux of secondary emission after the absorption process. Both EY and FY detection modes are used. In the EY detection, one either measures the electron yield with channeltron multiplier or the drain current of the sample. In the FY detection, the fluorescence detector collects emitted photons. Due to the short electron escaping depth,[8-9] EY detection is surface sensitive and it can be affected by the applied magnetic field. FY measurements have no magnetic field problems, which probe bulk properties and as such can detect the XMCD of buried layers and interfaces. FY detection is susceptible to saturation or self-absorption effects[10-11] in samples that are not dilute, because the X-ray penetration and detection depths are equivalent. Saturation effects are small if the sample is optically thin, say below ~20 nm. In addition, FY-XAS (referred to as FYXAS in the following text) is intrinsically distorted, or in other words the FY intensity is not proportional to the absorption coefficient due to the energy-dependent variation in the integrated X-ray emission intensities.[12-13] Deviations of the FYXAS shapes due to the intrinsic variations of fluorescence decay strengths has been demonstrated by Kurian *et al.*[14]

Although the identification of FYXAS to EY-XAS (referred to as XAS in the following text) had been disapproved, it is not obvious whether the intrinsic variations of fluorescence decay have large effects on the sum-rule-derived $L_z$ and $S_z$ expectation values. The theoretical analysis by van Veenendaal *et al.*[15] suggested that when the total fluorescence decay is not strongly polarization dependent, only small deviations exist in the $L_z$ and $S_z$ values obtained by FY detection, implying that the sum rules hold for $L_{2,3}$ edges of 3d transition metals and $M_{4,5}$ edges of light rare earths ($n<7$). Nevertheless, arguments were also raised concerning the angular dependence of the sum rule results.[16] In the current work, we revisit this issue from both the theoretical and experimental

side. Theoretically, multiplet approaches were used to investigate the spectral difference between EY- and FY-XMCD (referred to as XMCD and FYXMCD in the following text). The respective sum-rule-derived $L_z$ and $S_z$ values obtained under different detection directions were compared. The simulations were focused on the magnetically most studied 3d transition metal elements Mn, Fe, Co and Ni. Experimentally, Fe and Co XMCD spectra of the $CoFe_2O_4$ thin film were obtained by using both EY and FY methods. Sum rules were applied on the spectra of both elements to examine the expectation values obtained by both yield methods.

## 5.2. THEORY AND EXPERIMENT

### 5.2.1. Multiplet simulations

The simulations were performed with the ligand field multiplet approach by using the Cowan-Butler-Thole's multiplet code that was further modified and developed by Thole *et al.*[17-19] In order to simplify the model and to focus on the essence of the deviations of FY in $L_{2,3}$ XAS and XMCD, charge transfer effects have been neglected. Note that charge transfer effects are more prominent in highly covalent complexes where electrons are delocalized. In divalent transition metal oxides where electrons are more localized, charge transfer effects are expected to be minor. In the ionic limit the initial state configuration can be described by a $2p^63d^n$ configuration.

In the 2p XAS simulation, all dipole allowed transitions from the initial configuration $2p^63d^n$ to the final state $2p^53d^{n+1}$ configuration were considered. In the simulations on $Mn^{2+}$, $Fe^{2+}$, $Co^{2+}$ and $Ni^{2+}$ ions, atomic values of the Slater integrals (80% of Hartree-Fock calculated values) and spin-orbit couplings ($L{\cdot}S_p$ and $L{\cdot}S_d$) were used. Calculations of all four elements were performed under the octahedral ($O_h$) symmetry, using a cubic ligand field splitting (10Dq) of 1.0 eV and a super-exchange field (M) of 10 meV. Selection rules are imposed on the transitions to obtain the XMCD spectra where both the incident X-ray direction and the magnetization are assumed to be along the z-axis. The XMCD spectrum is defined as the absorption of left circularly polarized (positive helicity, $\mu_{+1}$) X-rays minus the absorption of right circularly polarized (negative helicity, $\mu_{-1}$) X-rays. Note that the definition of left and right X-ray components is inverted in part of the literature leading to an inverted XMCD spectrum.

Since the 2p3d X-ray emission channel dominates the radiative decay, the FY can be effectively described by the energy integrated 2p3d resonant inelastic X-ray scattering (RIXS) process. The fluorescence relaxation is the inverted process of absorption, in which dipole transitions from excited/intermediate states with the $2p^53d^{n+1}$ configuration to final states with the $2p^63d^n$ configuration happen. FY simulations in the current work are based on following rules that are based on a combination of observations and calculations:

(I). Auger decay is dominant and it sets the lifetime of XAS final states.
(II). The lifetime of Auger decay is constant for core-core-core channels. It varies in channels where valence states are involved, but this variation can be neglected.[12]

(III). The 2p3d FY decay is the dominant radiative channel, where we note that the 2p3s and 2p4s decay channels have typically relative strengths of 10% to 20%. Being core-core decay channels, the 2p3s and 2p4s RIXS decay do not show any energy dependence.

(IV). The FY XAS and XMCD spectra will be calculated from the integral over the complete 2p3d decay channel.

(V). The 2p3d FY decay is strongly energy dependent.

(VI). The 2p3d FY decay is strongly detection angle dependent.

The 2p3d inelastic X-ray scattering process can be described by the Kramers-Heisenberg formula[20-21] and the scattering cross section is the function of in-coming ($\Omega$) and out-going ($\omega$) X-ray energies given as:

$$F(\Omega,\omega) = \sum_f \left| \sum_n \frac{\langle f|T_2|i\rangle\langle i|T_1|g\rangle}{E_g+\Omega-E_i+\mathrm{i}\frac{\Gamma}{2}} \right|^2 \times \delta(E_g+\Omega-E_f-\omega) \quad (1)$$

where the *g*, *i* and *f* represents initial state, intermediate state and final state respectively. $T_1$ and $T_2$ are the dipole operators of absorption and emission. $\Gamma$ indicates the intermediate states lifetime. Interference effects are included in the FY calculation with $\Gamma$ set to 0.4 eV (full width at half maxima, fwhm). The 2p3d RIXS simulations were performed under $C_4$ symmetry that yield 9 combinations of left, right and z-polarized incoming and out-going X-rays. FYXMCD spectra were obtained by considering the different emission directions as:[22]

$$I_q^{normal} = I_{q0} + \frac{1}{2}(I_{q1} + I_{q-1}) \quad (2)$$

$$I_q^{iso} = I_{q0} + I_{q1} + I_{q-1} \quad (3)$$

The normal geometry here implies the fluorescence detector is at 90 degree (normal scattering geometry) with respect to the magnetic axis; while the isotropic detection is considered as it is used in literatures.[15-16] The isotropic signal is obtained from the fluorescence signal detection integrated over all angles or if the detector is at the 'magic angle' with respect to the magnetic axis. The calculated transitions were convoluted with Lorentzian and Gaussian functions to account for the lifetime and experimental resolution respectively. Note that because the FY signal is integrated over final states, the final state lifetime and experimental resolution will not affect the FY spectra.

### 5.2.2. Procedure to obtain the sum-rule-derived values

The sum rules apply to the transition between two well defined shells and here for 3d transition metals $L_{2,3}$ edges, the transition is between 2p level and 3d level. The integrated 2p3d X-ray absorption spectrum over the whole $L_{2,3}$ edge is proportional to the number of empty 3d holes ($\langle n_h \rangle$). The absorption coefficient (μ) includes the individual left ($\mu_{+1}$), right ($\mu_{-1}$) and z ($\mu_0$) polarized components as: $\int\mu = \int(\mu_{+1}+\mu_{-1}+\mu_0)$. In order to allow direct comparison to the experimental data, in this work the z polarized component is assumed to be one half the addition of other two components as: $\int\mu = \frac{3}{2}\int(\mu_{+1}+\mu_{-1})$. With these assumptions, the orbital momentum sum rule is defined as:

$$\langle L_z \rangle = \frac{4}{3}\langle n_h \rangle \frac{\int_{L_3+L_2}(\mu_{+1}-\mu_{-1})}{\int \mu} \tag{4}$$

For the spin momentum sum rule, it describes the effective spin momentum that is $\langle SE_z \rangle = \langle S_z \rangle + 7/2\langle T_z \rangle$. In this work, the spin-quadrupole coupling $\langle T_z \rangle$ is assumed to be zero. So $\langle S_z \rangle$ equals to the effective spin moment $\langle SE_z \rangle$ that was discussed in the reference.[23] Hence, the spin momentum sum rule is given as:

$$\langle S_z \rangle = \langle n_h \rangle \frac{\int_{L_3}(\mu_{+1}-\mu_{-1}) - 2\int_{L_2}(\mu_{+1}-\mu_{-1})}{\int \mu} \tag{5}$$

For the application of the spin sum rule, the core hole spin-orbit coupling must be much larger than the 2p3d multiplet effects, yielding well separated $L_3$ and $L_2$ edges. Although the $L_3$ and $L_2$ edges of 3d transition metals appear separated in shape, they are strongly mixed in character due to the large 2p3d multiplet effects.[23] The division energy of the $L_3$ and $L_2$ edges was chosen to be consistent in both XMCD and FYXMCD spectra that ensures the effective comparison of $\langle S_z \rangle$ values from the two yield methods.

### 5.2.3. Sample preparation

The sample used was a 10 nm (011)-oriented $CoFe_2O_4$ thin film supported the $[Pb(Mg_{1/3}Nb_{2/3})O_3]_{0.68}$-$[PbTiO_3]_{0.32}$ substrate. The film was synthesized via pulsed laser deposition at a substrate temperature of 590°C in an oxygen ambient of $1x10^{-4}$ Torr using a KrF excimer laser fluence of 1.3 J/cm$^2$. The sample was cooled to room temperature in an atmosphere of 1 Torr of oxygen after deposition. SQUID magnetization measurements show that the Curie temperature is above 600K.

### 5.2.4. X-ray absorption experiments

The sample was measured at the X-Treme beamline at the Swiss Light Source.[24] The measurements were carried out with a 30 degree grazing incident X-ray beam along the substrate (100) direction. A 2T magnetic field was applied along the incident beam direction. The FY detector was set at 90 degree to the incident beam. The EY and FY XAS spectra with left or right circularly polarized incident X-rays were acquired simultaneously. The experimental XAS spectra only include the left and right components. The measurements were performed at room temperature.

## 5.3. RESULTS AND DISCUSSION

### 5.3.1. Calculated XAS, FYXAS, XMCD and FYXMCD spectra of $Mn^{2+}$, $Fe^{2+}$, $Co^{2+}$, $Ni^{2+}$

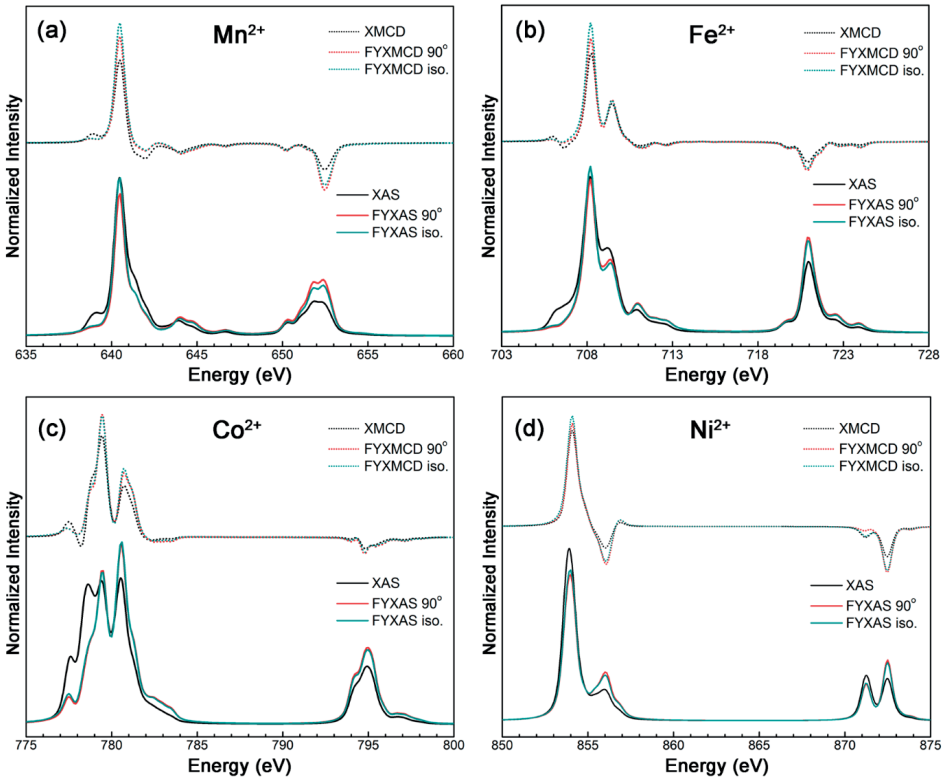


**FIG.1.** The calculated $L_{2,3}$ XMCD and FYXMCD (dotted lines), XAS and FYXAS (solid lines) spectra of (a) $Mn^{2+}$, (b) $Fe^{2+}$, (c) $Co^{2+}$ and (d) $Ni^{2+}$ ions. EY spectra are with the black color; FY spectra of 90° and isotropic detection geometries are with red and green colors respectively. XMCD and FYXMCD spectra are all inverted for plotting.

Figure 1 shows the calculated XAS and XMCD spectra together with the FY counterparts under both 90° and isotropic scattering geometry of $Mn^{2+}$ ($3d^5$), $Fe^{2+}$ ($3d^6$), $Co^{2+}$ ($3d^7$) and $Ni^{2+}$ ($3d^8$) ions. The calculated XAS only include the left and right polarized absorption components. For FY spectra, left and right components were calculated based on the descriptions of equation (2) and (3). Both XAS and XMCD spectra are normalized to the corresponding XAS integral and FY spectra are normalized to the respective FYXAS integral. Note that XMCD and FYXMCD spectra in this figure are inverted on purpose just to save the plotting space. Comparing the XAS with FYXAS of both scattering geometries, a general trend is observed with the FYXAS giving increased intensity at the higher energy side of the $L_3$ edge and an increased intensity of the $L_2$ edge. In particular, the $L_3/L_2$ intensity ratio of $Mn^{2+}$ ($3d^5$) ion is decreased in FYXAS spectra with the 90° scattering geometry. The observed distortion in FYXAS shape had been explained by the state dependent fluorescence decay ratio,[12, 14] where the fluorescent decay matrix element was shown to be proportional to the exchange integral $G^1_{pd}$.[15] The differences between FYXAS spectra under the two geometries are less obvious, especially for $Co^{2+}$ and $Ni^{2+}$ ions, in which spectral differences are almost invisible. For the $Mn^{2+}$ ion, a higher $L_3$ edge and a lower $L_2$ edge are shown in the isotropic FYXAS spectra comparing to its 90° scattering FY counterpart.

It can be seen from upper panels of Figure 1 (a) - (d) that the spectral shape difference between the XMCD and FYXMCD (both geometries) spectra is smaller than that in absorption spectra. Differences between the FYXMCD spectra under two geometries are similar to those shown in the corresponding FYXAS spectra. A more prominent difference is observed in FY spectra of the $Mn^{2+}$ ion, while more similar FYXMCD spectra under different geometries are found in both $Co^{2+}$ and $Ni^{2+}$ ions. The sum-rule-derived $L_z$ and $S_z$ values from the calculated XMCD and FYXMCD spectra under both scattering geometries are listed in Table 1. Deviations shown represent sum-rule-derived $L_z$ and $S_z$ values from FYXMCD with respect to the corresponding value from XMCD. Note that the positive or negative $L_z$ and $S_z$ values obtained are related to the definition of left and right polarized X-rays. The values shown in Table 1 are based on the spectra plotted in Figure 1.

The $Mn^{2+}$ ($3d^5$) ion in the current calculation is in the high spin ground state $^6A_1$ symmetry, in which the electron occupation can be approximated as $t_{2g}^3 e_g^2$. The orbital momentum is, in first approximation, zero with no effective influence of the valence spin orbit coupling. The sum-rule-derived $L_z$ value from current XMCD calculation is approximately -0.001, i.e. not exactly zero due to minor mixing of excited quartet multiplet states. The sum-rule-derived $L_z$ values from FYXMCD spectra with 90° and isotropic scattering geometries are -0.077 and 0.317 respectively, which strongly deviates from the XMCD result. For the $Fe^{2+}$ ($3d^6$) ion, sum-rule-derived $L_z$ values from FYXMCD under two detection geometries deviate ~±20% from the expectation value obtained from XMCD. The large difference between $L_z$ values obtained by the two fluorescence scattering

geometries also indicates that sum rule results are dependent on fluorescence detection direction. This is understandable since in some cases the fluorescent emission can be strongly angular dependent due to the departure from spherical symmetry in the intermediate state. [16] Similar deviations between XMCD and FYXMCD, and the detection geometry dependent FY results are also found for both $Co^{2+}$ ($3d^7$) and $Ni^{2+}$ ($3d^8$) ions in the case of sum-rule-derived $L_z$ values. In particular, the calculated $Ni^{2+}$ $L_z$ value under 90° fluorescence scattering geometry deviates ~-32% from the calculated value from XMCD.

**TABLE 1.** Sum-rule-derived $L_z$ and $S_z$ values obtained from calculated XMCD and FYXMCD (90° and isotropic detections) spectra (Figure.1) of $Mn^{2+}$, $Fe^{2+}$, $Co^{2+}$ and $Ni^{2+}$ ions. Deviations of $L_z$ and $S_z$ values obtained from FY spectra with respect to the that from EY spectra are calculated based on $\frac{\text{FYXMCD} - \text{XMCD}}{\text{XMCD}}$ %.

| | XMCD | FYXMCD (90° detection) | *Deviation** | FYXMCD (iso. detection) | *Deviation** |
|---|---|---|---|---|---|
| **$\langle L_z \rangle$** | | | | | |
| $Mn^{2+}$ | -0.001 | -0.077 | -- | 0.317 | -- |
| $Fe^{2+}$ | 0.756 | 0.621 | *-18%* | 0.902 | *19%* |
| $Co^{2+}$ | 0.909 | 0.986 | *9%* | 1.045 | *15%* |
| $Ni^{2+}$ | 0.320 | 0.219 | *-32%* | 0.293 | *-8%* |
| **$\langle S_z \rangle$** | | | | | |
| $Mn^{2+}$ | 1.664 | 2.572 | *55%* | 2.636 | *58%* |
| $Fe^{2+}$ | 1.423 | 1.719 | *21%* | 1.814 | *27%* |
| $Co^{2+}$ | 0.929 | 1.119 | *20%* | 1.114 | *20%* |
| $Ni^{2+}$ | 0.920 | 0.954 | *4%* | 1.061 | *15%* |

* Deviations of $L_z$ values from $Mn^{2+}$ ions are not present in such way due to mathematically meaningless

The sum-rule-derived $S_z$ values from XMCD and FYXMCD listed in Table 1 were calculated by using divisions of the $L_3$ and the $L_2$ edges at respectively 649 eV, 717 eV, 790 eV and 862 eV for $Mn^{2+}$, $Fe^{2+}$, $Co^{2+}$ and $Ni^{2+}$ ions. These energies are based on the energy scale shown in Figure 1. Note that divisions of the two edges chosen can slightly influence the $S_z$ values, but the consistency in XMCD and FYXMCD allows the direct comparison between sum-rule-derived $S_z$ values from them. The $S_z$ values obtained from FY spectra show relatively less detection geometry dependence compared to the $L_z$ values, though for $Ni^{2+}$ the difference between $S_z$ values from the two fluorescence detection geometries is still significant. The difference between $S_z$ values obtained by FY and by EY detections are demonstrated by the deviations calculated in Table 1. The deviations for $Mn^{2+}$ are found to be more than 50% for both fluorescence detection geometries. For $Fe^{2+}$ and

$Co^{2+}$ ions, deviations are between 20% and 30%; while deviations are found to be relatively small for the $Ni^{2+}$ ion, especially for fluorescence under 90° detection geometry. A general trend visible in Table 1 is that deviations of $S_z$ values decrease with the increase of 3d electron occupation for these four ions chosen here. A similar trend can be seen for the case of $L_z$ values except for $Ni^{2+}$ ion under 90° fluorescence detection geometry.

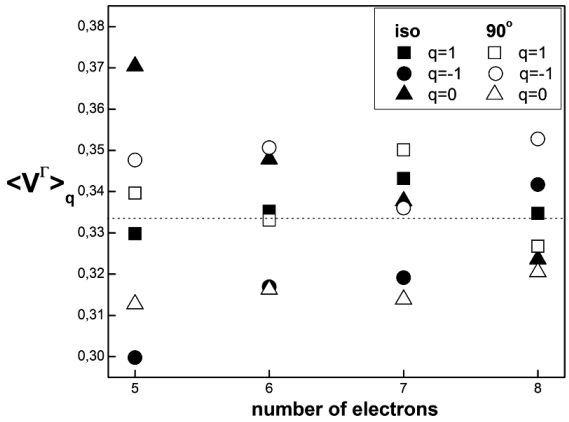


**FIG.2.** The calculated total decay $<V^{\Gamma}>_q$ for $Mn^{2+}$, $Fe^{2+}$, $Co^{2+}$ and $Ni^{2+}$ ions with the 3d electron occupation from 5 to 8. Solid and hollow symbols correspond to the FY detection geometry of isotropic and 90° respectively. Components of different polarizations are represented by square (q=1), circle (q=-1) and triangle (q=0). The dotted straight line represents the value of 1/3.

In the reference,[15] van Veenendaal *et al*. showed that $I_q^{fluor}=I_q^{XAS}<V^{\Gamma}>_q$, where the $I_q^{fluor}$ and $I_q^{XAS}$ are respectively the integrated intensity of fluorescence and XAS with the polarization of q (0 and ±1), and $<V^{\Gamma}>_q$ is defined as the *total* decay. Based on this equation, the requirement for using FYXMCD as a quantitative tool is that the $<V^{\Gamma}>_q$ has no strong polarization dependence. The $<V^{\Gamma}>_q$ values of $Mn^{2+}$, $Fe^{2+}$, $Co^{2+}$ and $Ni^{2+}$ ions under two detection geometries were calculated to correlate with deviations of the sum-rule-derived values from fluorescence detections. The $<V^{\Gamma}>_q$ values shown in Figure 2 are after the normalization of $\Sigma_q<V^{\Gamma}>_q=1$. When all the three $<V^{\Gamma}>_q$ equal 1/3 (the value shown as the dotted line in Figure 2), the fluorescence decay is polarization independent. It is seen from Figure 2 that deviations of total decay values from 1/3 are relatively small, similar to the results shown in the reference.[15] A relatively large deviation of the total decay happens for the $Mn^{2+}$ ion under isotropic detection geometry. This may partly explain the large deviations found in its $L_z$ and $S_z$ values as shown in Table 1. One qualitative relationship between the total decay and the deviation of $L_z$ values found is when $<V^{\Gamma}>_1$ (square signs in Figure 2) is larger than $<V^{\Gamma}>_{-1}$ (circle signs in Figure 2), the $L_z$ value obtained by FY detection is larger than

that by EY detection and *vice versa*. Furthermore, although not linearly, the larger difference between $<V^{\Gamma}>_1$ and $<V^{\Gamma}>_{-1}$, the larger deviation of FY $L_z$ values are shown. However, the full quantitative relationship between the differences of total decay values (q=1 or q=-1) and the deviation of $L_z$ and $S_z$ values obtained by FY is more complex. For example, under the isotropic detection, the deviation for the $L_z$ value of $Fe^{2+}$ ion is larger than that of $Co^{2+}$ ion but the deviation for the total decay value of $Fe^{2+}$ ion is smaller. In the case of $S_z$ values, the calculated deviations are even more difficult to be correlated with that for total decay values. Nevertheless, the comparison of two deviations indicates that even for fluorescence with small deviated total decay values from 1/3, or equivalently, with weak polarization dependent total decay $<V^{\Gamma}>_q$, may still lead to the large error in the sum-rule-derived $L_z$ or $S_z$ values.

### 5.3.2. Experimental results on $CoFe_2O_4$ thin film

Experimentally, the Fe and the Co $L_{2,3}$ edge XMCD and FYXMCD spectra from the $CoFe_2O_4$ thin film were carried out to investigate the quantitative results obtained by the two detection methods. $CoFe_2O_4$ is supposed to be an inverse spinel, in which $Co^{2+}$ occupies the $O_h$ sites and $Fe^{3+}$ is split between the $O_h$ and the tetrahedral ($T_d$) sites. Previous studies [25] showed, however, that Fe in the $CoFe_2O_4$ contains the $Fe^{2+}$ $O_h$, $Fe^{3+}$ $O_h$ and $Fe^{3+}$ $T_d$ components and consequently Co may also contain the $Co^{3+}$ $T_d$ component to balance the charge. The distribution of Co components is often correlated with the sample preparation conditions including sample forming temperatures and fast cooling rates, etc. [26] In $CoFe_2O_4$, magnetic properties of Fe components are the same as those in $Fe_3O_4$, where the $Fe^{2+}$ and $Fe^{3+}$ ions at $O_h$ sites are ferromagnetic and the $Fe^{3+}$ ions at $T_d$ sites are antiferromagnetic. The weight of each Fe component may vary from sample to sample due to the deviation of site occupancies. For the thin film measured in the current work, the weights of Fe components were obtained with a fitting procedure. The upper panel of Figure 3 shows the experimental Fe $L_{2,3}$ XMCD spectrum together with the calculated result. In this figure, both XMCD spectra were normalized to the corresponding XAS integral and the obtained calculated spectrum was further scaled to the intensity of the experimental XMCD spectrum at 709.1 eV. This normalization procedure allows a more direct comparison between calculated and experimental spectra. It is noted that the calculated spectrum slightly disagrees with the experimental data around 712-713 eV. This can be caused by the omission of charge transfer effects in current calculations. The $Fe^{3+}$ system is more covalent than the $Fe^{2+}$ ion and it may require the inclusion of more configurations to better simulate the experimental data. In the lower panel of Figure 3, separate XMCD spectra of $Fe^{2+}$ $O_h$, $Fe^{3+}$ $O_h$ and $Fe^{3+}$ $T_d$ components are presented with their corresponding weights of 12.32%, 54.94% and 32.74%.

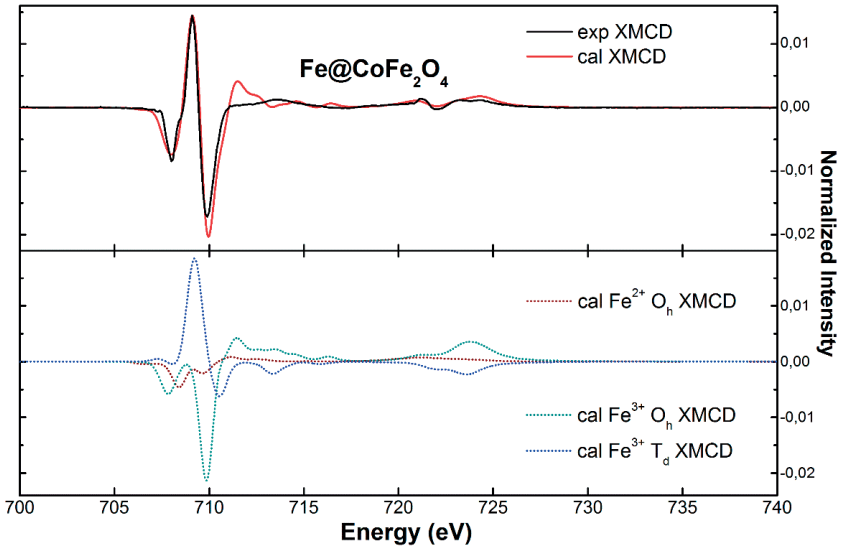


**FIG. 3.** Upper panel: Experimental (black line) and calculated (red line) Fe $L_{2,3}$ XMCD spectra of the $CoFe_2O_4$ thin film. Lower panel: the calculated XMCD spectra of $Fe^{2+}$ $O_h$ (wine red dots), $Fe^{3+}$ $O_h$ (green dots) and $Fe^{3+}$ $T_d$ (blue dots) components. The calculated spectra include contributions of the ground state and all Boltzmann distributed excited states at 300K.

An important parameter in the fitting of the combined spectral shape is the relative shifts of the three components. In case of isolated (or binary) $Fe^{2+}$ and $Fe^{3+}$ oxides, the shift between $Fe^{2+}$ and $Fe^{3+}$ is approximately 1.5 eV. [27] In $CoFe_2O_4$ the octahedral iron sites are coupled by hopping, implying that the shift is reduced. The fitting procedure finds that the shift is reduced to 0.7 eV, with $Fe^{2+}$ $O_h$ at 711.3 eV and $Fe^{3+}$ $O_h$ at 712.0 eV, and with the $Fe^{3+}$ $T_d$ position at 711.8 eV. The ground state of $Fe^{2+}$ $O_h$, $Fe^{3+}$ $O_h$ and $Fe^{3+}$ $T_d$ ions are respectively the $^5T_2$, $^6A_1$ and $^6A_1$ symmetries. The spin-orbit coupling and exchange field together yield a number of low-lying states for the $^5T_2$ symmetry. The exchange field alone also yields several low-lying states for the $^6A_1$ symmetry. In the calculation, Boltzmann weighted states were included for all three Fe components to account for the temperature dependent states occupation. For the XMCD calculation, all Boltzmann weighted symmetry states were considered.

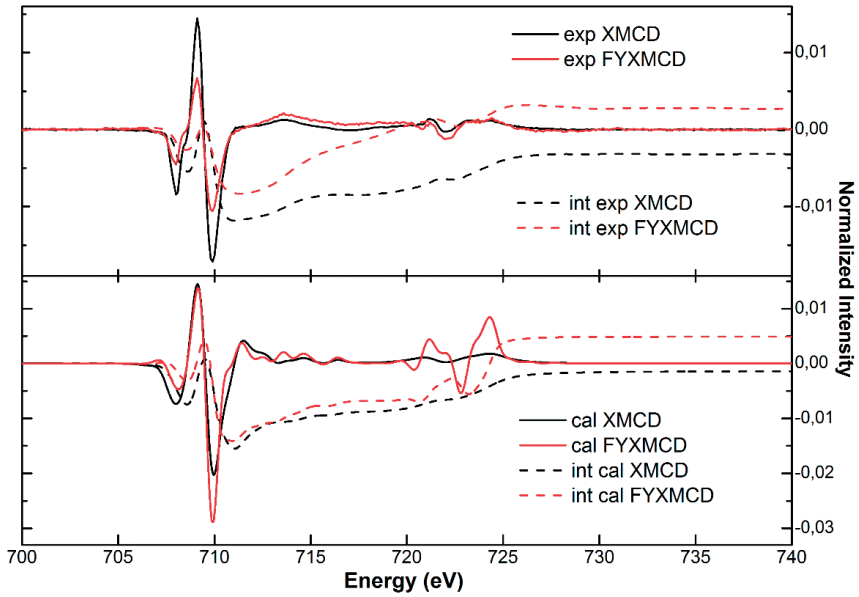


**FIG. 4**. Fe $L_{2,3}$ XMCD (black line), (FY)XMCD (red line) spectra and the corresponding integrals (int, dashed lines). Upper panel: experimental results from the $CoFe_2O_4$ thin film. Lower panel: calculation results.

The upper panel of Figure 4 shows the Fe $L_{2,3}$ edge experimental XMCD and FYXMCD spectra from the $CoFe_2O_4$ thin film, together with their respective integrals. Both spectra present are normalized to their respective XAS integral. The spectral shape of Fe FYXAS suggests that no (see Figure S2 in Appendix) saturation or self-absorption effects exist, and we neglect them in the current discussion. This is justified by the 10 nm thickness of the $CoFe_2O_4$ thin film sample measured in this work. Since XMCD and FYXMCD spectra are already normalized to respective XAS and FYXAS integrals, integrals shown in this figure are proportional to the $L_z$ values of all temperature populated states included. The fact that the integral of FYXMCD spectrum has an opposite sign of the XMCD spectrum integral directly indicates the non-negligible deviation of sum-rule-derived $L_z$ values by FY detection. The sum-rule-derived $S_z$ values from the experimental XMCD and FYXMCD are respectively -0.093 and -0.044, which were calculated by separating the $L_3$ and $L_2$ edges at 718 eV and considering the number of holes of average three Fe components as 4.88. Both deviations in the $L_z$ and $S_z$ values clearly indicate that FY is unsuitable for quantitative XMCD analysis.

**TABLE 2.** Ligand field multiplet parameters used for simulating Fe spectra of the $CoFe_2O_4$ thin film. All values are given in eV. The bottom panel of the table gives the reduction of the Slater integrals ($F^2_{dd}$, $F^4_{dd}$, $F^2_{pd}$, $G^1_{pd}$ and $G^3_{pd}$) with respect to their atomic values, as derived from the fitting procedure. The exchange field value used in all calculations is 41 meV.

| Parameter (eV) | $F^2_{dd}$ | $F^4_{dd}$ | $F^2_{pd}$ | $G^1_{pd}$ | $G^3_{pd}$ | $\mathbf{L}\cdot\mathbf{S}_p$ | $\mathbf{L}\cdot\mathbf{S}_d$ | 10Dq |
|---|---|---|---|---|---|---|---|---|
| **$Fe^{2+}$ $O_h$** | | | | | | | | |
| initial state (EY&FY) /final state (FY) | 8.097 | 5.032 | | | | | 0.025 | 1.240 |
| intermediate state (FY) /final state (EY) | 8.697 | 5.410 | 4.942 | 3.643 | 2.070 | 8.200 | 0.033 | 1.240 |
| **$Fe^{3+}$ $O_h$** | | | | | | | | |
| initial state (EY&FY) /final state (FY) | 8.843 | 5.533 | | | | | 0.029 | 1.780 |
| intermediate state (FY) /final state (EY) | 9.413 | 5.891 | 5.461 | 4.081 | 2.322 | 8.199 | 0.036 | 1.780 |
| **$Fe^{3+}$ $T_d$** | | | | | | | | |
| initial state (EY&FY) /final state (FY) | 8.926 | 5.585 | | | | | 0.029 | -0.650 |
| intermediate state (FY) /final state (EY) | 9.501 | 5.946 | 5.501 | 4.145 | 2.358 | 8.199 | 0.036 | -0.650 |
| Parameter (atomic value %) | $F^2_{dd}$ | $F^4_{dd}$ | $F^2_{pd}$ | $G^1_{pd}$ | $G^3_{pd}$ | $\mathbf{L}\cdot\mathbf{S}_p$ | $\mathbf{L}\cdot\mathbf{S}_d$ | |
| **$Fe^{2+}$ $O_h$** | 92.3 | 92.3 | 90.9 | 91.0 | 91.0 | 100 | 49.0 | |
| **$Fe^{3+}$ $O_h$** | 91.8 | 91.8 | 91.7 | 91.7 | 91.7 | 100 | 49.0 | |
| **$Fe^{3+}$ $T_d$** | 92.7 | 92.7 | 92.4 | 93.1 | 93.1 | 100 | 49.0 | |

The question can be raised whether the deviation found in this case is only related to the experimentally different probing depth of EY and FY detections, or it also results from the intrinsic energy dependent fluorescence decay. To determine this, the simulated Fe spectra were compared with experimental results. The lower panel of Figure 4 shows the corresponding simulation results, in which spectra were plotted after the same normalization procedure as used in Figure 3 and a same scaling factor was used for both spectra. The calculation parameters are present in Table 2. In FY calculations, for the $Fe^{2+}$ Oh component, the lowest lying ground state with the first five excite states that together account for ~96.2% of the total room temperature populated states were included; while for both $Fe^{3+}$ components, the ground state and the first two excited states that account for ~99.1% of all populated states were considered. Integrals of the calculated XMCD and FYXMCD spectra are with opposite signs and both are in correspondence with their experimental counterparts. Note that sharper $L_2$ edge features shown in the FYXMCD spectrum are due to the smaller lifetime broadening value of the $L_2$ edge used than that used in the XMCD spectrum calculation, and which do not influence the integral values. The small differences between integral

values of the calculated and corresponding experimental spectra may result from spectral mismatches, such as the fine structures around 711-712 eV. But it can also relate to experimental effects of different probing depths of the two detections that are not included in calculations. Nevertheless, sum-rule-derived $L_z$ values obtained from calculation results show the same trend of deviations as demonstrated by the experimental data, which proves the effects of intrinsic fluorescence decay variations on deviations of ground state expectation values obtained by the FY detection. The $S_z$ values extracted from calculation results are respectively the -0.115 (EY) and -0.148 (FY). It is clear that these values differ from those obtained by experiments. Apart from the spectral mismatches as mentioned in above text, the valid applications of spin sum rule are needed for the determination of more accurate $S_z$ values from calculation results. [23] More details on this issue will be given in the discussion below.

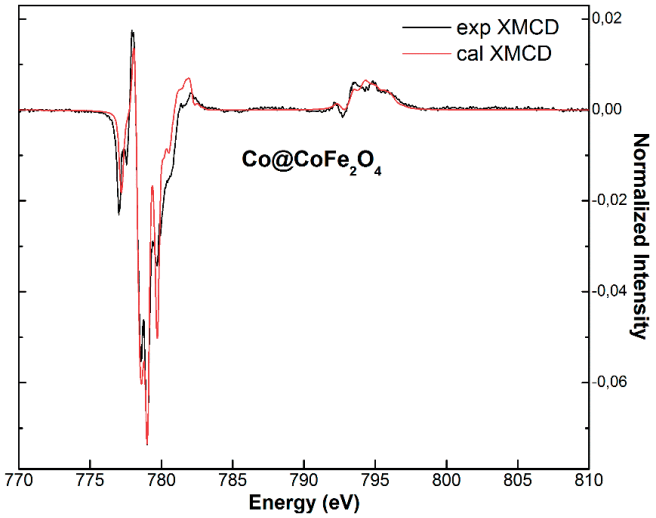


**FIG. 5.** Experimental (black line) Co $L_{2,3}$ XMCD spectrum of the $CoFe_2O_4$ thin film and the corresponding calculation result (red line).

The Co experimental data from the $CoFe_2O_4$ thin film were also analyzed. The evidence of $Fe^{2+}$ $O_h$ component suggests that ~12% $Co^{3+}$ ions could be present in $T_d$ sites to balance the charge and the site occupancy. Fine structures in the experimental Co XAS spectrum (see Figure S4 in Appendix) however, indicate that the Co ion present should consist of minor or no $Co^{3+}$ ion since its corresponding fine structures and intensities are almost invisible. In current analyses, we assume the Co component to be only the $Co^{2+}$ ion with $O_h$ symmetry. The charge and site occupancy imbalance may due to the imperfect occupancy of oxygen sites that yields the sample as $CoFe_2O_4$.

x. For simplicity, here we keep to name the thin film sample as $CoFe_2O_4$. Figure 6 shows the comparison of experimental and calculated Co $L_{2,3}$ XMCD spectra. Both spectra present are normalized to their corresponding XAS integrals and the calculated result was further scaled to the intensity of experimental data at 779 eV. The calculation parameters are listed in Table 3. The lowest lying ground state of the $Co^{2+}$ ($d^7$) ion is with the $^4T_1$ symmetry. In the Co XMCD calculation, all temperature populated states based on the Boltzmann distribution were included. Most of the fine structures shown in the experimental spectrum are well reproduced by the calculated spectrum, which should largely support the assumption of $Co^{2+}$ $O_h$ ion present alone in the measured $CoFe_2O_4$ thin film.

**TABLE 3.** Ligand field multiplet parameters used for simulating Co spectra of the $CoFe_2O_4$ thin film. All values are given in eV. The bottom panel of the table gives the reduction of Slater integrals with respect to their atomic values. The exchange field in both simulations are 41 meV.

| Parameter (eV) | $F^2_{dd}$ | $F^4_{dd}$ | $F^2_{pd}$ | $G^1_{pd}$ | $G^3_{pd}$ | $\mathbf{L}\cdot\mathbf{S}_p$ | $\mathbf{L}\cdot\mathbf{S}_d$ | 10Dq |
|---|---|---|---|---|---|---|---|---|
| initial state (EY&FY) /final state (FY) | 9.052 | 6.416 | | | | | 0.041 | 1.070 |
| intermediate state (FY) /final state (EY) | 9.669 | 7.708 | 6.244 | 4.911 | 3.069 | 9.748 | 0.051 | 1.070 |
| Parameter (atomic value %) | $F^2_{dd}$ | $F^4_{dd}$ | $F^2_{pd}$ | $G^1_{pd}$ | $G^3_{pd}$ | $\mathbf{L}\cdot\mathbf{S}_p$ | $\mathbf{L}\cdot\mathbf{S}_d$ | |
| | 78 | 89 | 86 | 91 | 100 | 100 | 62 | |

Figure 6 shows the experimental (upper panel) and corresponding calculated (lower panel) Co XMCD and FYXMCD spectra together with the integrals. Spectra were normalized by the same methods as used in Figure 5. In the FY calculation, the lowest ground state and the first five excited states that together account for ~97.6% of all temperature populated states were included. Similar to Fe, the deviation of sum-rule-derived Co $L_z$ values from experimental data is obviously reflected by the difference of integral values. The integral difference is less prominent in the calculation results, but which shows the same trend as that shown in the experimental spectra. Sum-rule-derived $L_z$ values from the calculated XMCD and FYXMCD spectra are respectively -0.25 and -0.21, giving a ~-18% deviation for the value from FY. For the $S_z$, sum-rule-derived values from experimental data are -0.148 (EY) and -0.106 (FY), in which the deviation is clearly seen. The $S_z$ values obtained from the calculated spectra are with a ~14% deviation. We note that $S_z$ values from current calculation results are not directly comparable to that obtained from experiments by using the spin sum rule.[23] In this case, deviations shown in both $L_z$ and $S_z$ values from calculated results suggest that the intrinsic problem of FY still influence the quantitative analysis results.

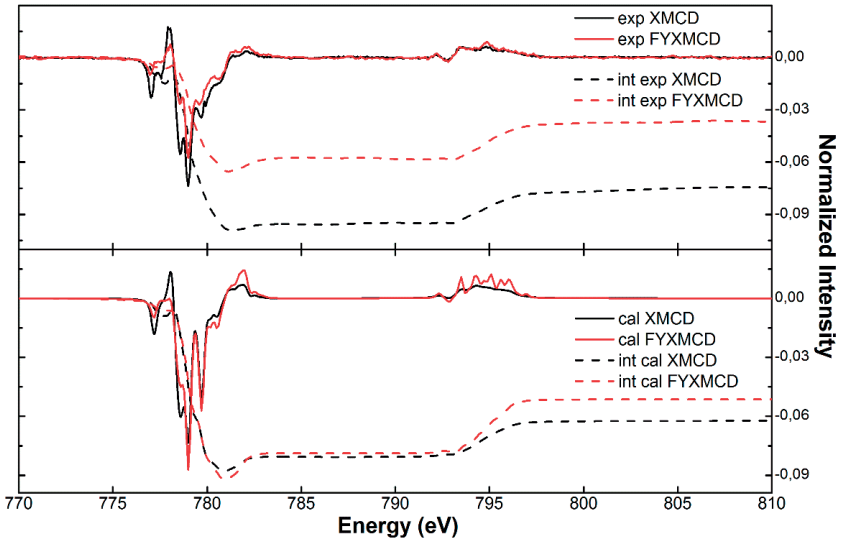


FIG. 6. Co $L_{2,3}$ XMCD (black line), (FY)XMCD (red line) spectra and the corresponding integrals (int, dashed lines). Upper panel: experimental results from the $CoFe_2O_4$ thin film. Lower panel: calculation results.

### 5.3.3. Deviations between the sum-rule derived Sz value and Sz

As discussed above we have added another factor that causes deviations between the sum-rule derived $S_z$ value and the actual value. Previous studies have indicated that two important factors are (1) the value of $T_z$ and (2) the multiplet-induced mixing of the $L_3$ and $L_2$ edges.[23] These two factors play a role independent of the detection method. In this paper we added a third intrinsic factor in the form of the difference in the energy-dependent FY decay for left and right polarized x-rays. As shown above this effect can be significant and it adds to the two other effects discussed above. It only applies to FY detected spectra of the $L_{2,3}$ edges of 3d transition metal systems.

## 5.4. CONCLUSION

We have analyzed the difference of sum-rule-derived ground state expectation values given by EY and FY. For the investigated $Mn^{2+}$, $Fe^{2+}$, $Co^{2+}$ and $Ni^{2+}$ ions, their respective EY- and FY-XMCD spectra differ from each other. FYXMCD spectra also show the detection angle dependent shapes. Differences shown in the spectral shape strongly correlate to intrinsic variations of intermediate states fluorescence lifetimes. This variation of fluorescence lifetimes lead to the deviated sum-rule-derived $L_z$ and $S_z$ values obtained by FY, which are also angular dependent. For the studied four

ions, the $Mn^{2+}$ ion shows the largest deviation in both $L_z$ and $S_z$ values. A general trend of deviations revealed is that they decrease with the increase of 3d electron occupation, except for the $L_z$ value of $Ni^{2+}$ ion under the 90° fluorescence detection geometry. The total decay $<V^{\Gamma}>_q$ of each ion are also calculated. Differences between $<V^{\Gamma}>_1$ and $<V^{\Gamma}>_{-1}$ values can be qualitatively correlated with deviations shown in the $L_z$ value, but we did not find a simple quantitative relationship. The small deviations of $<V^{\Gamma}>_q$ values from 1/3 indicate that the weak polarization dependent total decay does not necessarily imply reliable quantitative XMCD analysis by FY.

The Fe and Co $L_{2,3}$ edge XMCD spectra of the $CoFe_2O_4$ thin film measured by both EY and FY are studied. The experimental differences of the EY- and FY-XMCD spectral shapes are reproduced by multiplet calculations, including the resulting difference in the $L_z$ and $S_z$ values. It turns out that more than experimental factors, intrinsic factors are added to the complication of FYXMCD applications on the quantitative analysis. Therefore, although the FY detection shows several advantages over the EY detections, care should be taken on the quantitative information obtained by FY as intrinsic deviations are difficult to be ruled out.

## ACKNOWLEDGMENTS

This work was financially supported by the China Scholarship Council and the ERC advanced grant XRAYonACTIVE, number 340279. We thank Cinthia Piamonteze, Jakoba Heidler, Jan Dreiser, Rajesh Chopdekar and Frithjof Nolting for their experimental support. We also thank Mario Ulises Delgado-Jaime for the data analysis help. We also thank Ru-pan Wang and Frank M.F.de Groot for the helpful discussions on the theory parts.

## Supporting Information available in Appendix 5

## REFERENCES


(1) Funk, T.; Kennepohl, P.; Di Bilio, A. J.; Wehbi, W. A.; Young, A. T.; Friedrich, S.; Arenholz, E.; Gray, H. B.; Cramer, S. P. *J. Am. Chem. Soc.* **2004**, *126*, 5859-5866.

(2) Funk, T.; Gu, W. W.; Friedrich, S.; Wang, H. X.; Gencic, S.; Grahame, D. A.; Cramer, S. P. *J. Am. Chem. Soc.* **2004**, *126*, 88-95.

(3) Mizumaki, M.; Yano, K.; Umehara, I.; Ishikawa, F.; Sato, K.; Koizumi, A.; Sakai, N.; Muro, T. *Phys. Rev. B* **2003**, 132404.

(4) Thole, B. T.; Carra, P.; Sette, F.; van der Laan, G. *Phys. Rev. Lett.* **1992**, *68*, 1943-1946.

(5) Carra, P.; Thole, B. T.; Altarelli, M.; Wang, X. D. *Phys. Rev. Lett.* **1993**, *70*, 694-697.

(6) Chen, C. T.; Idzerda, Y. U.; Lin, H. J.; Smith, N. V.; Meigs, G.; Chaban, E.; Ho, G. H.; Pellegrin, E.; Sette, F. *Phys. Rev. Lett.* **1995**, *75*, 152-155.

(7) Thole, B. T.; van der Laan, G.; Fuggle, J. C.; Sawatzky, G. A.; Karnatak, R. C.; Esteva, J. M. *Phys. Rev. B* **1985**, *32*, 5107-5118.

(8) Vogel, J.; Sacchi, M. *J. Electron Spectrosc. Relat. Phenom.* **1994**, *67*, 181-188.

(9) Nakajima, R.; Stohr, J.; Idzerda, Y. U. *Phys. Rev. B* **1999**, *59*, 6421-6429.

(10) Eisebitt, S.; Boske, T.; Rubensson, J. E.; Eberhardt, W. *Phys. Rev. B* **1993**, *47*, 14103-14109.

(11) de Groot, F. M. F. *Nat. Chem.* **2012**, *4*, 766-767.

(12) de Groot, F. M. F.; Arrio, M. A.; Sainctavit, P.; Cartier, C.; Chen, C. T. *Solid State Commun.* **1994**, *92*, 991-995.

(13) Pompa, M.; Flank, A. M.; Lagarde, P.; Rife, J.; Stekhin, I.; Nakazawa, M.; Ogasawara, H.; Kotani, A. *J. Phys. IV (France)* **1997**, *7*, 159-160.

(14) Kurian, R.; Kunnus, K.; Wernet, P.; Butorin, S. M.; Glatzel, P.; de Groot, F. M. F. *J. Phys. Condens. Matter* **2012**, *24*, 452201.

(15) van Veenendaal, M.; Goedkoop, J. B.; Thole, B. T. *Phys. Rev. Lett.* **1996**, *77*, 1508-1511.

(16) Goedkoop, J. B.; Brookes, N. B.; van Veenendaal, M.; Thole, B. T. *J. Electron Spectrosc. Relat. Phenom.* **1997**, *86*, 143-150.

(17) Cowan, R. D. *J. Opt. Soc. Am.* **1968**, *58*, 808-818.

(18) Cowan, R. D. *The Theory of Atomic Structure and Spectra*; University of California Press: Berkeley, CA, 1981.

(19) Thole, B. T.; van der Laan, G.; Butler, P. H. *Chem. Phys. Lett.* **1988**, *149*, 295-299.

(20) Kramers, H. A.; Heisenberg, W. *Z. Phys.* **1925**, *1*, 681-701.

(21) Kotani, A.; Shin, S. *Rev. Mod. Phys.* **2001**, *73*, 203-246.

(22) Thole, B. T.; Vanderlaan, G.; Fabrizio, M. *Phys. Rev. B* **1994**, *50*, 11466-11473.

(23) Piamonteze, C.; Miedema, P.; de Groot, F. M. F. *Phys. Rev. B* **2009**, *80*, 184410.

(24) Piamonteze, C.; Flechsig, U.; Rusponi, S.; Dreiser, J.; Heidler, J.; Schmidt, M.; Wetter, R.; Calvi, M.; Schmidt, T.; Pruchova, H.; Krempasky, J.; Quitmann, C.; Brune, H.; Nolting, F. *J. Synchrot. Radiat.* **2012**, *19*, 661-674.

(25) Pattrick, R. A. D.; Van der Laan, G.; Henderson, C. M. B.; Kuiper, P.; Dudzik, E.; Vaughan, D. J. *Eur. J. Mineral.* **2002**, *14*, 1095-1102.

(26) Waseda, Y.; Shinoda, K.; Sugiyama, K. *Z. Naturforsch., A: J. Phys. Sci.* **1995**, *50*, 1199-1204.

(27) de Groot, F. M. F.; Glatzel, P.; Bergmann, U.; van Aken, P. A.; Barrea, R. A.; Klemme, S.; Havecker, M.; Knop-Gericke, A.; Heijboer, W. M.; Weckhuysen, B. M. *J. Phys. Chem. B* **2005**, *109*, 20751-20762.

# Appendix 5

## Contents

The raw experimental Fe L edge XAS and FYXAS of the $CoFe_2O_4$ thin film. Spectra measured with left and right polarized X-rays are shown separately.

The raw experimental Fe L edge XAS and FYXAS of the $CoFe_2O_4$ thin film. Spectra shown are summed with left and right polarized components.

The raw experimental Co L edge XAS and FYXAS of the $CoFe_2O_4$ thin film. Spectra measured with left and right polarized X-rays separately.

The raw experimental Co L edge XAS and FYXAS of the $CoFe_2O_4$ thin film. Spectra measured with left and right polarized X-rays are shown separately.

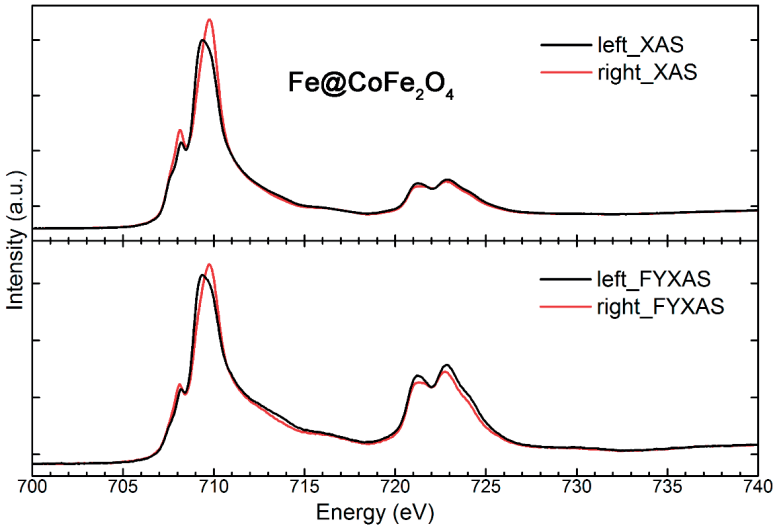


**Fig S1**. Experimental raw Fe L edge XAS (upper panel) and FYXAS (lower panel) of the $CoFe_2O_4$ thin film. Spectra measured with left (black line) and right (red line) polarized X-rays respectively.

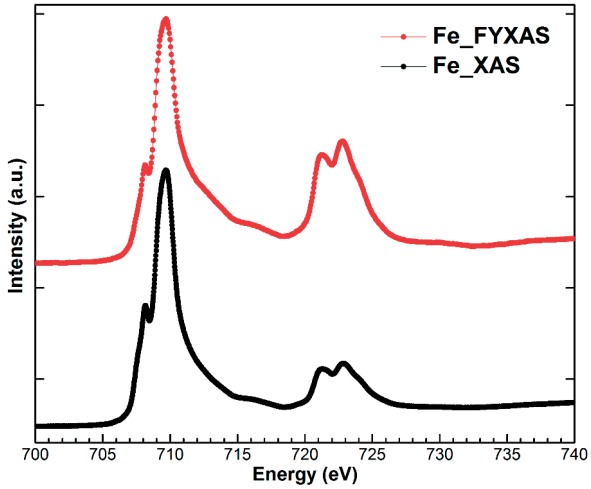


**Fig S2**. Experimental raw Fe L edge XAS (red dotted-line) and FYXAS (black dotted-line) of the $CoFe_2O_4$ thin film. Each spectrum is summed by the components measured by left and right polarized X-rays as shown in Figure S1.

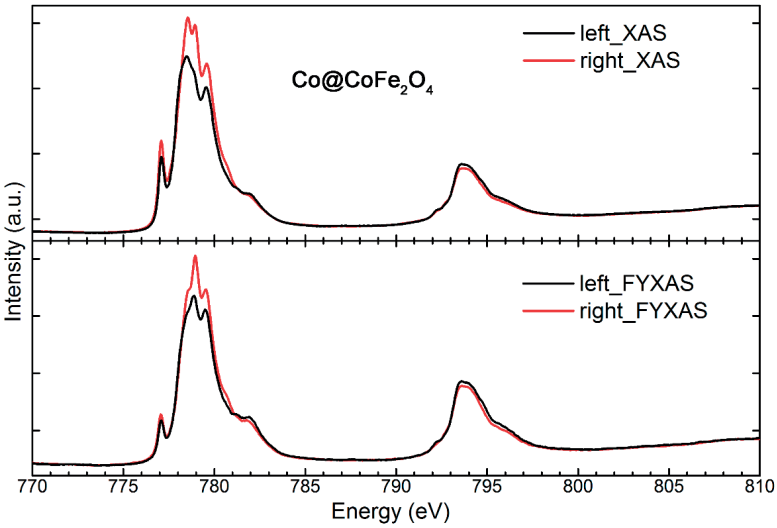


**Fig S3**. Experimental raw Co L edge XAS (upper panel) and FYXAS (lower panel) of the $CoFe_2O_4$ thin film. Spectra measured with left (black line) and right (red line) polarized X-rays respectively.

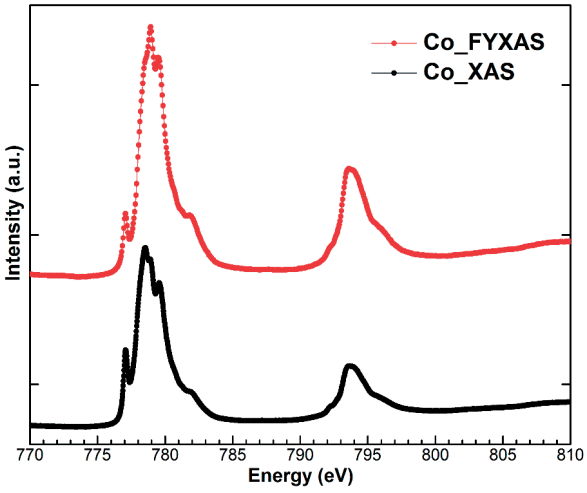


**Fig S4**. Experimental raw Co L edge XAS (red dotted-line) and FYXAS (black dotted-line) of the $CoFe_2O_4$ thin film. Each spectrum is summed by the components measured by left and right polarized X-rays as shown in Figure S3.

# Summary

Throughout my PhD work, I have focused on synchrotron-based 2p X-ray absorption spectroscopy (XAS) and 2p3d resonant inelastic X-ray scattering (RIXS) to study several cobalt containing materials. 2p3d RIXS that shows high sensitivity to the partially filled 3d orbitals of transition metal ions within different types of materials, which yields unique chemical information. The ligand field multiplet (LFM) approach is used for the theoretical interpretation of the experimental spectra.

In **Chapter 1**, X-ray spectroscopies, especially the 2p XAS (including X-ray magnetic circular dichroism, XMCD) and 2p3d RIXS are introduced with a few fundamental aspects from both experimental and theoretical sides. The experimental issues, such as saturation or self-absorption effects in 2p XAS spectra, which are important for understanding the measured results are emphasized. The principle of the RIXS experimental instruments that are used in the work in Chapter 2 and 3 are also illustrated.

The high energy resolution 2p XAS and 2p3d RIXS spectra are used to investigate the ground state electronic structure of transition metal sites in two polyoxometalate (POM) water oxidation catalysts in **Chapter 2**. The $[Co_4(H_2O)_2(\alpha\text{-}PW_9O_{34})_2]^{10-}$ ($Co_4P_2$) and $[Co_4(H_2O)_2(\alpha\text{-}VW_9O_{34})_2]^{10-}$ ($Co_4V_2$) catalysts are iso-structural but they show large different catalytic properties. The examination of each tetra-cobalt core in both catalysts and vanadium centers in $Co_4V_2$ serves to understand differences of the electronic structures in these two POM catalysts. The cobalt 2p3d RIXS spectra demonstrated a smaller ligand field strength of the tetra-cobalt core in $Co_4V_2$ than that in $Co_4P_2$. The vanadium 2p3d RIXS spectra of $Co_4V_2$ indicate, apart from the ligand oxygen to vanadium metal ion charge transfer, also the charge transfer between cobalt and vanadium centers. This offers the experimental proof on the previous theoretically predicted hybridization of cobalt and vanadium 3d orbitals. The smaller ligand field strength shown by cobalt RIXS and the cobalt vanadium charge transfer shown in vanadium RIXS complementarily suggest a larger electron delocalization from cobalt centers in the ground state of $Co_4V_2$. The non-activated electronic structure information, although not the final determining factor, brings insights to the potential electron transfer routes that may influence the catalytic properties of the $Co_4V_2$ catalyst.

In **Chapter 3**, the cobalt 2p3d RIXS with experimental resolution ~90 meV full width at half maximum is exploited to probe the single cobalt centered POM $K_5H[CoW_{12}O_{40}]\cdot xH_2O$. The low energy d-d excitation feature ~0.55 eV corresponding to the $^4T_2$ manifold under tetrahedral symmetry is unmeasurable with ultraviolet-visible (UV/vis) spectroscopy, and here it is firstly revealed. The high energy resolution RIXS spectra are simulated via the LFM approach, by which

the tetragonal ($D_{2d}$) distortion on cobalt sites is discussed. This distortion is effectively inaccessible by diffraction techniques. However, RIXS spectra with greater energy resolution than current one could offer the possibility to examine more accurate the local symmetry environment of transition metal ions. In 2p3d RIXS spectra, both optical allowed and forbidden transitions are revealed, which allows the assignment of d-d excitation features with higher accuracy than from previous optical data. Based on the LFM simulation results, we also use the wave-function decomposition method to analyze the more realistic and detailed origins of a few lowest d-d excitations, in both one-electron-orbital and term symbol descriptions. The simulated 2p3d RIXS results based on the experimental data offers a full picture of the ground state electronic structure of the cobalt ions in this POM.

A combined in-situ 2p XAS and 2p3d RIXS study on the carbon-thermal reduction of cobalt Fischer-Tropsch catalyst is present in **Chapter 4**. Both XAS and RIXS spectra are acquired at three different temperatures. For the RIXS acquisition, four excitation energies are consistently applied at each temperature that yields twelve spectra. The XAS spectrum acquired after 700ºC reduction shows a pure cobalt metal like spectral shape while the RIXS results clearly reveal the characteristic d-d excitation feature of cobalt monoxide, indicating the different sensitivity of these two technique to the minority oxide phase in this case. The holistic fit are performed on both XAS and RIXS results. In the RIXS spectra, a first approached decomposition-fit model is used that allows the separation of multiple spectral components in the RIXS spectra. From the fit results, the relative precision to determine the cobalt monoxide content changes from ~5% in 2p XAS to better than 2% in 2p3d RIXS, suggesting 2p3d RIXS as a useful tool to track the oxidation state of nanoparticles under in-situ conditions. In analyses of RIXS quantification results, an extra sensitivity factor is explored by combining the XAS and RIXS fit results. This sensitivity factor determines the capability of 2p3d RIXS for revealing minority CoO phase, however, which is not obtained with the high accuracy in current work. This calls further exploration on it, which will add interesting fundamental knowledge of the creation and decay of 2p core holes in oxides, respectively, metals.

In **Chapter 5**, we investigate the differences between electron and fluorescence yield XMCD derived sum-rule values. We revisit this issue by using both model LFM simulations on 3d transition metal ions $Mn^{2+}$ ($3d^5$), $Fe^{2+}$ ($3d^6$), $Co^{2+}$ ($3d^7$) and $Ni^{2+}$ ($3d^8$) and the experimental cobalt, iron data from 10 nm $CoFe_2O_4$ thin film sample. The model simulation results indicate that fluorescence yield detected sum rule derived expectation values of $L_z$ and $S_z$ show noticeable deviations and the detection angle dependence. Also, a small deviation of the polarization dependent fluorescent decay values from 1/3 can lead to large deviation to significant deviations in the $L_z$ and $S_z$ sum rule values. The experimental data from 10 nm thin film are free of saturation

effects and are suitable to explore the fluorescence yield deviations from state-dependent decay ratios. The deviations between electron and fluorescence yield XMCD spectra, in both iron and cobalt cases, are explained by the simulation results, suggesting that fluorescence yield XMCD result is unsuitable for quantitative analysis of the $L_z$ and $S_z$ sum rule values.

# Samenvatting

Tijdens mijn promotieonderzoek heb ik me beziggehouden met synchrotrongebaseerde 2p Röntgen absorptie spectroscopie (XAS) en 2p3d *resonante inelastische Röntgen verstrooiing* (RIXS) om daarmee kobalt-bevattende materialen te bestuderen. 2p3d RIXS heeft een grote gevoeligheid voor de gedeeltelijk gevulde 3d orbitalen van overgangsmetaalionen in verschillende materialen, wat unieke chemische informatie oplevert. De ligandveld multiplet theorie (LFM) is gebruikt voor de theoretische interpretatie van de experimentele spectra.

In **hoofdstuk 1** wordt Röntgenspectroscopie geïntroduceerd met de beschrijving van een aantal experimentele en theoretische aspecten, met name de 2p XAS (met inbegrip van X-ray magnetisch circulair dichroïsme, XMCD) en 2p3d RIXS. De experimentele vraagstukken die van belang zijn voor het begrijpen van de gemeten resultaten worden benadrukt, waaronder verzadiging- en zelfabsorptie-effecten in 2p XAS spectra,. Het principe van RIXS experimenten die worden gebruikt in het proefschrift wordt uitgelegd.

In **hoofdstuk 2** worden hoge energie-resolutie 2p XAS en 2p3d RIXS spectra gebruikt om de elektronische structuur van overgangsmetaal-locaties te onderzoeken in twee polyoxometalaatcomplexen (POM) water oxidatie katalysatoren. De $[CO_4(H_2O)_2(\alpha\text{-}PW_9O_{34})_2]^{10-}$ ($Co_4P_2$) en $[CO_4(H_2O)_2(\alpha\text{-}VW_9O_{34})_2]^{10-}$ ($Co_4V_2$) katalysatoren zijn iso-structureel, maar ze vertonen grote verschillen in hun katalytische eigenschappen. Het onderzoek van de tetra-kobalt kern in beide katalysatoren en van de vanadium centra in $Co_4V_2$ heeft als doel de verschillen in de elektronische structuur van deze twee katalysatoren te begrijpen. De kobalt 2p3d RIXS spectra tonen een kleiner ligandveld in de tetra-kobalt kern $Co_4V_2$ dan in $Co_4P_2$. Vanadium 2p3d RIXS spectra van $Co_4V_2$ laten zien dat er naast de zuurstof vanadium ladingsoverdracht ook ladingsoverdracht is tussen kobalt en vanadium centra. Dit geeft het experimentele bewijs van de theoretisch voorspelde hybridisatie van de kobalt en vanadium 3d orbitalen. Het kleinere ligandveld uit de kobalt RIXS samen met de kobalt vanadium ladingsoverdracht uit de vanadium RIXS suggereren samen een grotere elektrondelocalisatie van de kobalt centra in $Co_4V_2$. Dit brengt inzichten om de potentiële elektronenoverdracht routes te bepalen die de katalytische eigenschappen van de katalysator beïnvloeden in $Co_4V_2$.

In **hoofdstuk 3** wordt cobalt 2p3d RIXS met experimentele resolutie ~90 meV benut om het kobalt ion gecentreerd in de POM $K_5H[CoW_{12}O_{40}]\cdot xH_2O$ te karakteriseren. De lage energie d-d excitatie van ~0.55 eV komt overeen met de $^4T_2$ toestand in de tetraëdrische symmetrie, welke niet zichtbaar is met ultraviolet-zichtbare (UV/vis) spectroscopie. De hoge energie-resolutie RIXS spectra worden gesimuleerd via de LFM aanpak, waarbij de tetragonale ($D_{2d}$) verstoring op de kobalt-sites wordt meegenomen. Deze vervorming is niet meetbaar met diffractie technieken. Echter, RIXS

spectra met een grotere resolutie energie dan de huidige zou de mogelijkheid hebben om nauwkeuriger de lokale symmetrie van overgangsmetaal-ionen te onderzoeken. In 2p3d RIXS spectra zijn zowel optische toegestane als verboden overgangen zichtbaar, wat de toewijzing van d-d excitaties toelaat met hogere nauwkeurigheid dan eerdere optische data. Op basis van de LFM simulatie resultaten en de golffunctie decompositie methode is het mogelijk de gedetailleerde oorsprong van de d-d excitaties te analyseren, zowel in één-electron-orbitalen als in de veeldeeltjes term symbool beschrijving. De gesimuleerde 2p3d RIXS resultaten op basis van de experimentele data geeft een goed beeld van de elektronische structuur van de kobalt ionen in deze POM.

Een gecombineerde in situ 2p XAS en 2p3d RIXS studie over de koolstof-thermische reductie van een kobalt Fischer-Tropsch katalysator is beschreven in **hoofdstuk 4**. Zowel de XAS en RIXS spectra zijn verkregen op drie verschillende temperaturen. Voor de RIXS spectra worden vier excitatie energieën consistent toegepast bij elke temperatuur wat in totaal twaalf spectra oplevert. Het XAS spectrum verkregen na reductie bij 700 $^{o}$C toont een zuiver kobaltmetaal terwijl de RIXS resultaten duidelijk de karakteristieke d-d excitatie van kobaltmonoxide onthullen. De holistische fit wordt uitgevoerd op zowel de XAS en de RIXS resultaten. Uit de resultaten blijkt dat de relatieve nauwkeurigheid van de hoeveelheid kobaltmonoxide verbetert van ~5% in 2p XAS tot beter dan 2% in 2p3d RIXS waaaruit geconcludeerd wordt dat 2p3d RIXS een nuttige methode is om de oxidatietoestand van nanodeeltjes te volgen onder in-situ-omstandigheden.

In **hoofdstuk 5** onderzoeken we de verschillen tussen electron-detectie en fluorescentie-detectie in XMCD metingen en de daaruit afgeleide waardes van de somregels. We bekijken dit theoretisch door het gebruik van zowel LFM simulaties op de 3d metaalionen $Mn^{2+}$ ($3d^5$), $Fe^{2+}$ ($3d^6$), $Co^{2+}$ ($3d^7$) en $Ni^{2+}$ ($3d^8$) alsmede kobalt en ijzer experimenten aan $CoFe_2O_4$ dunne films. De simulatieresultaten geven aan dat de op fluorescentie gebaseerde somregel $L_z$ en $S_z$ verwachtingswaarden geven die grote, hoekafhankelijke, afwijkingen hebben. Het blijkt dat een kleine afwijking van de polarisatie-afhankelijke fluorescentie leidt tot significante afwijkingen in de $L_z$ en $S_z$ somregel waarden. De experimentele gegevens van de 10 nm dunne $CoFe_2O_4$ film zijn vrij van verzadigingseffecten en geschikt om de fluorescentie-detectie afwijkingen experimenteel te onderzoeken. De afwijkingen tussen de elektronen- en fluorescentie-detectie ijzer en kobalt XMCD spectra kunnen worden verklaard door de simulatieresultaten, wat suggereert dat fluorescentie-detectie XMCD resultaten niet geschikt zijn voor een kwantitatieve analyse van de $L_z$ en $S_z$ somregel waarden.

# Acknowledgements

During my four and a half years stay in Netherlands, there are so many persons to whom I really want to express my deep gratitude. Here, I would like to give my appreciation for people who helped me in studies or researches and for friends I met in Netherlands during the past years using English; in the end, I will use my native language to express my gratitude to my family members.

First of all, I wish to give my deepest gratefulness to my supervisor Prof. Dr. Frank de Groot. I still remember that before I came to Utrecht, a Chinese senior Ph.D. student who worked in the group of Professor Bert Weckhuysen told me that you are the most modest and the nicest professor in this large group. After I spent my four and a half years' Ph.D. study with you, I told many of my friends that you are the nicest person I have ever met until now. Sometimes I even joked with them saying that if everybody behaves like you, the world would become a kind of Utopia. No quarrels and battels happen. I still remember that the scholarship I brought by myself was only half of the normal Ph.D.'s salary, and living with this scholarship in Utrecht was really hard. I indeed had the idea to quit and to find other positions, since I had got several other positions with normal Ph.D. funding instead of the Chinese Scholarship Council (CSC) funding that I applied to cover my 4 years Ph.D. study with you. At beginning, you tried to support me financially, but it was not allowed by the university. Comparing with the 'half salary', your kindness and the willingness to offer me enough chances to learn and perform more work made me continued. Luckily, I finished my doctoral thesis and also learned a lot from those academic events that you offered me chances to join: 15 times beamtime, and a few times international conferences in different countries. Among them, 4 times in SLS (Switzerland), 3 times in BESSY II (Germany), 4 times in NSRRC (Taiwan), 2 times in SPring-8 (Japan) and 1 time in SSRL (USA), 1 time in Soleil (France) and 1 time in ESRF (France). Also, the SILS summer school in Grado (Italy), 2013; the IWP/RIXS conferences in Erice (Sicily, Italy), 2014; the XAFS 16 in Karlsruhe (Germany) 2015; and the VUVX 2016 in Zürich (Switzerland). Especially in Karlsruhe, I started to think about my next stop after attending the talk given by a professor, and with whom I will continue my research in the next two years.

Besides, I also wish to say thanks to the group members who work with Frank. For us, we need to perform experiments in synchrotrons and the group working is extremely important. During my beamtimes mentioned above, there are several group members joined and helped me. Firstly, Mr. Iron-Man: Ru-pan Wang. Rupan knows quite a lot about the experimental skills of soft X-ray RIXS and also the theory. With his help, I improved much faster than before for the experiments. We had many nice discussions and collaborations, which can be clearly seen from his involvement in my works. Mr. Red beard: Ties Haarman. Ties is my best Dutch friend, we spent several nice beam trips and conferences together. In Karlsruhe and in Zürich, he cooked many nice dinners for us,

and in NSRRC we had a nice RIXS beamtime together with his help on quick data analysis. He always bring me my favorite gums from Germany. More importantly, nearly every time when I made problems that requires Dutch speaking via telephone, I always goes to him and he is always willing to spend time to help. Mr. Super Mario: Mario U Delgado-Jaime, another super friendly guy in this group. Without your help on the data analysis, I could not easily finish two of my work as shown in the current thesis. Dr. Delgado, you can me became friends when we were in SPring-8 during my first RIXS beamtime there. Later I visited you when you were still living in Düsseldorf. You surprised me by serving me some delicious 'Chinese' food. From that time, I started to realize that you are not only an excellent scientist but also a good chef. It is really happy to know that recently you became a researcher at University of Guadalajara, in your beautiful hometown. I wish that you will have bright future and happy life with your family there. The next Dutch speaking friend, who were also bothered by me many times for Dutch speaking issues via telephone, is Mr. Samurai: Dr. Mustafa Al Samarai. I joined most of your beamtimes during your Ph.D. study in Frank's group. We had unhappy and happy memories for the experiments. But the beam trip to Stanford was the nicest memory. You achieved a real in-situ measurement, and probably later the JACS paper, and I also tried my best to help. You led me to experience some nice Iranian and Morocco food during our beamtime, and I named you the 'new half' in Japan. You followed Dr. Delgado and Dr. van Schooneveld to work as a postdoc in the group of Professor Serena de Beer, I really wish you could achieve nice in-situ work there. The next Dutch speaking friend, the mum of 'new half', is Mrs. Marte Curie: Marte van der Linden. As my wife said you are more beautiful than most real Dutch girl, you already became popular for Chinese when we were together in Versailles during our beamtime in Soleil. A group of Chinese visitors took pictures with you, the blond beauty as they told me. You are the most sophisticated Ph.D. in current group, and I wish that you would finish your work in time and live happily with Mr. Landman. Miss Hebatalla Elnaggar, you are the cleverest girl as I know and you also work very hard. The never ending issue of magnetite is waiting for you to end by photon-in and photon-out X-ray techniques, go! Don't forget to visit me in Chengdu, I will lead you to take pictures with Panda there. Mr. Zimmermann, the one who has and will never go to U.S., as you told me. We know each other firstly in Grado, and it was a big surprise you joined Frank's group later. In my opinion, it is really a pity if you can't become a teacher. You are really good at teaching others, explicitly and clearly. But I know that you want a yacht, hopefully you can save enough money as soon as possible, and to travel without the connection to rest of the world. Finally, I wish to thank toughest, but most excellent guy in Frank's group, Dr. van Schooneveld. Your work inspired me a lot since I started, and fortunately you came back to work for around a year, and I published the first work with your help. I wish you a bright future in your new job, and probably come back to academia in the future. Other group members, Dr. Myrtille Hunault, Dr. Mahnaz Ghiasi and Mr. Ahmed Ismail, I also wish you

guys have happy life in Netherlands. Another good friend in the large group is Mr. Ad van der Eerden. You taught me a lot during those beamtime we went together, and you helped me during my beamtime in SLS and NSRRC. I wish you enjoy your work in the group and your happy life with your family in Utrecht.

During my Ph.D. study in Utrecht University, I lived in Utrecht for the first year, after that I moved to Leiden, and stayed in this quiet and beautiful small town for almost another four years until now. In Leiden, I met a lot of friends here. Most of them were/are the Ph.D. candidates in Leiden University. Here, I give my gratitude and best wishes to these friends. They are: Dr. Jing Shen (沈静) and her husband Liang Zhou (周亮), Dejian Kong (孔德建) and his wife Zhenjie Li (李振杰), Lalin Kovudhikulrungsri, Zhan Xiong (熊瞻) and his wife Junling He (何俊伶), Dr. Song Wu (吴松), Yanming Guo (郭延明) and his wife Dr. Jinxian Wang (汪进贤), Feng Zhang (张峰), etc.

在这过去的四年半博士生涯里，我离开家乡，除了三次短时间回家，大多数时间没能和亲人生活在一起。幸运的是我的妻子为了和我在一起，辞掉了在国内很好的工作，来荷兰莱顿大学攻读博士，陪在了我身边。我们在荷兰结婚，幸福地在一起学习生活，也在欧洲旅游。更幸运的是，我们的儿子两年后在荷兰出生了。他的到来给我们寂寞的博士生涯带来了极大的快乐，也让我们这两个初为父母的年轻人有了许多改变。父母和岳父母从精神和经济上给了我们最大的帮助。我们的宝宝出生后，两位妈妈轮流来荷兰照顾他，也照顾我们，让我们有更多的精力去完成学业。我感谢父母，他们在我遇到任何困难的时候，都给予我他们所能提供的所有帮助，您们让我有信心去面对一切困难，也让我知道作为家长应该怎么样去爱自己的孩子；我感谢我的妻子，你在我脆弱的时候陪我在一起，给我无尽的安慰，鼓励和支持，让我坚强向前，你是我面对未来的强大动力；我也感谢我的岳父母，您们对我视如己出，尽力照顾我们这两个大孩子还有那一个小孩子。我们的儿子现在幸福地和姥姥姥爷生活在一起，没有姥姥姥爷的帮忙照顾，我和妻子的博士学业一定没法如现在一样完成。

在离开家到荷兰求学的时间里，最大的不幸，也是我一生永远无法弥补的痛，就是我最最亲爱的奶奶在我博士学业的第四年里，突然而永远地离开了我们。奶奶，您没来得及等到您的孙儿带着博士学位回来看您。您也没能见到您朝思暮想的重孙，我一定会带着他去您的墓前，告诉他，最爱你的祖祖知道你来看她了。奶奶，我知道，您一定在天堂正幸福地看着我们，看着我们如您所愿幸福地生活着。奶奶永活我心中！

# List of Publications and Presentations

## This thesis is based on following publications:

*Chapter 2:*

**Boyang Liu**, Elliot N. Glass, Ru-pan Wang, Yoshihisa Harada, Stefan Schuppler, Di-jing Huang, Craig L. Hill and Frank M. F. de Groot, *Vanadium-cobalt charge transfer in polyoxometalate water oxidation catalysts revealed by 2p3d resonant inelastic x-ray scattering*, submitted to Inorg. Chem.

*Chapter 3:*

**Boyang Liu**, Ru-pan Wang, Elliot N. Glass, Craig L. Hill, Tanja Cuk, Jun Okamoto, Di-jing Huang, Matti M. van Schooneveld and Frank M. F. de Groot, *Distorted tetrahedral $Co^{II}$ in $K_5H[CoW_{12}O_{40}]\cdot xH_2O$ probed by 2p3d resonant inelastic X-ray scattering*, Inorg. Chem. *55*, **2016**, 10152.

*Chapter 4:*

**Boyang Liu**, Matti M. van Schooneveld, Yi-tao Cui, Jun Miyawaki, Yoshihisa Harada, Thomas O. Eschemann, Krijn P. de Jong, Mario U. Delgado-Jaime and F. M. F. de Groot, *In-situ 2p3d resonant inelastic X-ray scattering tracking cobalt nanoparticle reduction*, submitted to J. Phys. Chem. C.

*Chapter 5:*

**Boyang Liu**, Cinthia Piamonteze, Mario U. Delgado-Jaime, Ru-pan Wang, Jakoba Heidler, Jan Dreiser, Rajesh Chopdekar, Frithjof Nolting and F. M. F. de Groot, *The difference between electron yield and fluorescence yield X-ray magnetic circular dichroism derived sum rule values*, submitted to Phys. Rev. B

## Other publications by the author:

Ru-pan Wang, **Boyang Liu**, Robert Green, Mario U. Delgado-Jaime, Thorsten Schmitt, Matti M. van Schooneveld and Frank M. F. de Groot, *Accurate charge transfer parameters of cobalt halides and sulfide derived from 2p3d RIXS*, submitted to J. Phys. Chem. C.

Mustafa Al Samarai, Christina H. M. van Oversteeg, Mario U. Delgado-Jaime, Tsu-Chien Weng, Dimosthenis Sokares, **Boyang Liu**, Marte van der Linden, Ad van der Eerden, Eelco Vogt, Bert Weckhuysen and Frank M. F. de Groot, *Nature of cobalt species studied during the in-situ sulfurization of CoMo/$Al_2O_3$ and CoNiMo/$Al_2O_3$ hydrodesulfurization catalysts*, submitted to J. Am. Chem. Soc.

**Boyang Liu**, Wang Zhang, Di Zhang, Haoming Lv and Xiaolu Gong, *Novel Ag decorated biomorphic SnO2 inspired by natural 3D nanostructures as SERS substrates*, Mater. Lett. *27*, **2012**, 11742.

## Oral presentations:

**Boyang Liu**, Mario U. Delgado-Jaime, Hisao Kiuchi, Hideharu Niwa, Jun Miyawaki, Yoshihisa Harada, Frank M. F. de Groot, "*In-situ 2p3d resonant X-ray emission spectroscopy of Co/CNT Fischer-Tropsch catalysts*", XAFS16, 23-28 Aug. 2015, Karlsruhe, Germany.

**Boyang Liu**, Tanja Cuk, Di-jing Huang, Frank M. F. de Groot, "*2p3d RIXS probe of $Co^{II}$ polyoxometalates ground state electronic structure*", EWinS 2016, 1-22 Feb. 2016, Ajdovščina, Slovenia.

**Boyang Liu**, Mario U. Delgado-Jaime, Jun Miyawaki, Yoshihisa Harada, Frank M. F. de Groot, "*Quantification of Co@CNT by in-situ 2p3d RIXS*", NCCCXVII, 7-9 Mar. 2016, Noordwijkerhout, the Netherlands.

**Boyang Liu**, Mario U. Delgado-Jaime, Yi-tao Cui, Yoshihisa Harada, Matti M. van Schooneveld, Frank M. F. de Groot, "*Quantification of 'Invisible' CoO by in-situ 2p3d Resonant Inelastic X-ray Scattering*", VUVX 2016, 3-8 Jul. 2016, Zürich, Switzerland.

## Poster presentations:

**Boyang Liu**, Frank M. F. de Groot, "*Resonant Inelastic X-ray Scattering study of carbon supported cobalt catalyst for Fischer Tropsch synthesis*", NCCCXV, 10-12 Mar. 2014, Noordwijkerhout, the Netherlands.

# CURRICULUM VITAE

Boyang Liu was born on November 22nd, 1985 in the city of Ya-an, Sichuan province, People's Republic of China. After finished his high school study in No. 7 high school Chengdu, he then started the bachelor study in the Institute of Materials Science and Engineering, Sichuan University in September 2004. In June 2008, he obtained the Bachelor of Science degree in Materials Physics. His graduate thesis research was performed in the group of Professor Shifu Zhu in Sichuan University. From Mach of 2009, he started to work as a research assistant (internship) in the group of Professor Di Zhang, in State Key Laboratory of Metal Matrix Composites, Shanghai Jiaotong University. From September 2009, he became a Master student in the same group and started to work on the fabrications of nanocomposites by using butterfly wing scales. After two and a half years study, he obtained the Master of Engineering degree in March 2012 with the thesis "Fabrication of SERS Nanocomposite Substrates from Butterfly Wing Scales". After that, he visited several groups in Japan and China, and finally decided to work with Professor Frank M. F. de Groot as a Ph.D. student in the Inorganic Chemistry and Catalysis group from Utrecht University, in the Netherlands. His Ph.D. study started at October 2012, from then he focused on using synchrotron based X-ray spectroscopy techniques to explore the electronic structures of various cobalt containing materials. During his Ph.D. study, he supervised one master student. Currently, he is working temporarily as a Postdoc in the same group to finish some work which are not included in the current thesis. From October 2017, the author will join the XsoLaS group as a post-doctor researcher to work with Prof. Anders Nilsson, in Stockholm University, Stockholm, Sweden.